High-Order Robotic Joint Sensing with Multiple Accelerometer and Gyroscope Systems

Laurence McLean

School of Mechanical Engineering
The University of Adelaide
South Australia 5005
Australia

A thesis submitted in fulfillment of the requirements for the degree of M. Phil. in Engineering on December 11, 2018.

M. Phil. Thesis

December 11, 2018

School of Mechanical Engineering
The University of Adelaide
South Australia 5005
Australia

Typeset by the author using LaTeX.
Printed in Australia.

Abstract

In recent years work into larger humanoid robotic systems and other highly dynamic legged robots has driven a need to increase control system performance and parameter estimation capability. This in turn has seen an increase in the use of higher order joint space derivative terms such as acceleration and jerk being introduced into the control systems and estimators. Although it is evident that the inclusion of these terms can increase the performance of the estimators and control systems, there is a distinct lack of high quality sensors or systems capable of providing this information. Instead it is apparent that those researchers aiming to employ the acceleration and jerk terms are having to resort to other poor quality methods of acquiring the information, which in turn limits the capability of the systems. The works examined suggest that in particular, access to higher quality sources of joint space acceleration measurement or estimation can lead to increases in the performance of control systems and estimators employing these terms. The aim of this work is to investigate the feasibility and capability of a new joint space sensor based on positional encoders and MEMs accelerometers that can estimate angular joint position, velocity and acceleration.

The system proposed employs the accelerometer only IMU (AO-IMU) concept to estimate link angular acceleration and velocity in an inertial frame. This concept is then extended to obtain these angular components relative to the previous link. Sensor fusion techniques are then tasked with estimating the velocity states of the AO-IMU and ensuring consistency across the relative states. Two calibration schemes are proposed and demonstrated to correct for the bias, gain and cross axis effects present in the inertial sensors and to correct for the non-ideal placement of the sensors on the body frame. The performance of the system is compared to three online methods common in the literature with significant increases in performance being shown across all states, particularly in the acceleration and velocity states.

The base sensor system is then augmented to explore alternate inertial sensor arrangements and structures. In this the effects of adding MEMs gyroscopes to the sensor system are studied and shown to have a small positive effect on the relative velocity state. The addition of multiple relative accelerometers are then studied to examine whether the initial system design choices could be improved upon, with this study showing greater increases in the relative acceleration and velocity states performance. Taking inspiration from the positive results of the multiple relative accelerometer study, an alternate sensor system structure is proposed whereby the robot is instrumented with AO-IMUs and the relative accelerometers omitted. This augmented structure may prove more useful in larger robotic systems. This study initially showed poor results with the low angular velocities experienced by the upper link AO-IMU introducing bias errors. This was corrected for by the inclusion of gyroscopes with the resulting system exhibiting good performance.

The findings within this work show that with some modification, the AO-IMU is capable of directly measuring the relative angular acceleration and velocity of a robotic link. When combined with positional sensors this system can be extended to obtain high quality measurements of a joint's angular position, velocity and acceleration.

Declaration

I certify that this work contains no material which has been accepted for the award of any other degree or diploma in my name, in any university or other tertiary institution and, to the best of my knowledge and belief, contains no material previously published or written by another person, except where due reference has been made in the text. In addition, I certify that no part of this work will, in the future, be used in a submission in my name, for any other degree or diploma in any university or other tertiary institution without the prior approval of the University of Adelaide and where applicable, any partner institution responsible for the joint-award of this degree.

I give consent to this copy of my thesis when deposited in the University Library, being made available for loan and photocopying, subject to the provisions of the Copyright Act 1968. I acknowledge that copyright of published works contained within this thesis resides with the copyright holder(s) of those works.

I also give permission for the digital version of my thesis to be made available on the web, via the University's digital research repository, the Library Search and also through web search engines, unless permission has been granted by the University to restrict access for a period of time.

	11/12/2018
SIGNED	DATED

Contents

List of Figures

List of Tables

Chapter 1

Introduction

1.1 Why a Rotary Joint Sensor

Modern robotic control systems typically rely on rotational position and velocity feedback to close a control loop around a joint of interest. With new work into humanoid and larger highly dynamic robotic systems becoming more prevalent, researchers have begun employing additional joint feedback data such as acceleration and jerk into control systems in order to increase machine performance.

1.1.1 Joint Sensing for Control System Performance

Possibly the primary argument for incorporating rotary joint acceleration or jerk measurements is that of general control system performance. In an effort to improve joint torque control Dallali et al. (2015) developed a feedback compensator that required estimates of joint velocity, acceleration and jerk. Radulescu et al. (2012) employed joint acceleration feedback in their optimal controller formulation, and in their work on humanoid robots Rotella et al. (2016) demonstrated that they are able to drive up stiffness and damping gains for feedback controllers when incorporating velocity and acceleration terms.

In all these works the acceleration or jerk terms were not available as measured quantities and in each case alternate means of obtaining the information were sought. Dallali et al. resorted to using differentiation of an encoder to obtain their estimates, while Radulescu et al. relied on an acceleration estimate obtained from their system model. Rotella et al. simply used the commanded acceleration as a substitute for the estimate into their control system.

Higher order derivatives of joint position and velocity also appear in work on highly dynamic legged robots. These machines, typically operating in some unstructured environment, will experience unexpected contacts with the environment and must be capable of compensating for these disturbances in real time. One such robot is the StarlETH quadruped robot (Hutter 2013). In this work joint acceleration was incorporated into a disturbance compensation task as part of their Hybrid Operational Space Control methodology. Hutter states that in their hardware set up acceleration was not available and laments the use of double differentiation in obtaining the data, due to the inherent noise issues. Instead an assumption was made that there would be no acceleration for slow manoeuvres and the term was set to zero. No mention of any performance cost due to this assumption was provided.

Joint acceleration data also finds their way into estimating other online quantities that then go on to find use in larger control systems. Humanoid robots rely on quantities such as the Centre of Mass (CoM) (Xinjilefu 2015) and Centre of Pressure (CoP) (Baelemans

2013) to estimate the machine's body state, which is in turn incorporated into the control of the robot. In these cases the acceleration terms are fused with other quantities such as information from kinematics. In the works by Xinjilefu (2015) and Baelemans (2013) once again the employed acceleration terms are not obtained via direct measurement. In these cases commanded accelerations and differentiated position and velocity terms are substituted for the measurements respectively.

1.1.2 Joint Sensing for Parameter Estimation

Parameter estimation in robotic systems revolves around finding estimates, ideally online, of unknown quantities such as link length, inertia, joint friction etc. If not estimated by some means, these parameters are typically taken from CAD models or measured in some way. Acquiring this information requires time and accuracy on the researcher's behalf and the quantities found during offline procedures may vary during the operation of the machine due to environmental factors.

In the limbed robotic systems of interest within this work, the majority of the parameter estimation efforts revolve around estimating the inertial components of the joint space dynamic model, typically of the form:

$$\boldsymbol{B}(\boldsymbol{q})\ddot{\boldsymbol{q}} + \boldsymbol{C}(\boldsymbol{q}, \dot{\boldsymbol{q}})\dot{\boldsymbol{q}} + \boldsymbol{F}_v\dot{\boldsymbol{q}} + \boldsymbol{F}_s\boldsymbol{sgn}(\dot{\boldsymbol{q}}) + \boldsymbol{g}(\boldsymbol{q}) = \boldsymbol{\tau}. \tag{1.1}$$

The parameters of interest within this model are the components of the inertia or mass matrix $\boldsymbol{B}$, the components of $\boldsymbol{C}$ which is a matrix representing the Coriolis and centripetal components, and the static and viscous friction components $\boldsymbol{F}_v$ and $\boldsymbol{F}_s$. The model may be extended or truncated depending on the requirements. Estimation of the parameters of this model appear in a number of different works. In an early work Khosla (1987) attempts to recover these components and explicitly relies on joint acceleration. Within this they employ an online least squares fit of five data points to obtain the acceleration term, noting that both the delay and noise exhibited by the process lead to bias in the estimates and lowered estimation performance.

Baelemans (2013) incorporated joint velocity and acceleration terms into a parameter estimation system for a humanoid robot. In this work they strictly rely on differentiation to obtain the acceleration terms. They go on to discuss issues encountered in estimating the robot inertia matrix terms, claiming the motions employed in the estimation tasks were not significant enough to resolve these terms. Aside from increasing the motion velocity and acceleration magnitudes they offer no solution to this issue, however noting that they employed noisy differentiation it may be possible that increasing the noise performance of the joint acceleration estimate may improve their results.

Joint acceleration appears in other parameter estimation works where the acceleration term is employed in the estimation process, but obtained via some online state estimator such as Unscented Kalman Filters (UKF) (Naerum et al. 2009; Van Der Merwe, Wan, Julier, et al. 2004), observers and adaptive controllers (Arteaga 2003) and Gaussian partially observable Markov decision process (POMDP) based systems (Webb et al. 2014).

In each of these systems the acceleration terms are sourced from internal estimates of the online estimator, rather than via measurement or differentiation. However such systems are not without issue. For example, in the case of the UKF the acceleration term is typically driven by a white noise process with no associated measurement and as may such lag the measured states.[1]

[1] This is demonstrated in this work in Section 5.3.2.1.

1.1.3 Motivation

It is evident that higher order terms such as joint acceleration and jerk can play a role in increasing robotic control system performance and enabling the successful estimation of parameters. However, it is apparent that researchers are using differentiation to estimate accelerations, 'good enough' assumptions to set accelerations to some known value, relying on models to obtain accelerations, or using commanded acceleration as the measurement into the control system. Those researchers relying on differentiation to obtain velocity and acceleration note the noise and phase delay issues that present from the differentiation of already noisy signals, and those employing models as a means of extracting acceleration find that they must first obtain accurate model parameters. However, these parameters may vary during the operation of the machine and may be time consuming, costly or otherwise difficult to obtain accurately. Rotella et al. noted in their work when employing commanded accelerations that measured accelerations should yield better results, however this remained untested.

The lack of use of estimates from sensors that directly measure joint acceleration within these works suggests that the available devices or techniques are not sufficient in some manner, and due to the benefits of incorporating these higher order terms into control system performance and parameter estimation methods, further investigation into finding a solution is warranted.

1.2 Thesis Structure

This work is presented in three major components. A review of the literature is first presented. This is then followed by the development testing of the sensor system, which is in turn followed by work on extending the sensor system.

Chapter 2 presents background information into the current state of joint space sensing, primarily pertaining to limbed robotic systems. Within this, classic methods of obtaining joint position and velocity are examined. Works regarding mechanical means of measuring acceleration and their issues are then considered. Following this the literature surrounding the recent works into incorporating MEMs sensors is discussed. From here we find that the use of MEMs devices shows promising results regarding estimating the higher order joint states, however the current means in which they are employed is perhaps not ideal. This then leads on to a discussion on the accelerometer only IMU (AO-IMU) and how this concept may be more suited for use in estimating joint states than the previous MEMs based techniques.

Chapters 3, 4 and 5 detail the development of the joint sensor system. The sensor system kinematics and theoretical basis are first developed in Chapter 3. Within this the issues regarding the individual inertial sensors are first outlined. The AO-IMU kinematics are then described and the issues regarding this formulation are first discussed. The relative kinematics are then derived.

Chapter 4 develops the estimators that are employed to mitigate the AO-IMU issues and fuse the states into usable information. The estimator for the AO-IMU is first presented, followed by a discussion on the development of the relative UKF. The development of the process noise matrices is then discussed.

Chapter 5 then presents the test rig hardware and the systems employed as baselines and online comparisons. Following this, two methods of calibrating the sensor system are then detailed. This chapter then details and discusses the results of testing the system on two motion profiles. The issues regarding calibration and misalignment are then investigated.

The final chapter, Chapter 6, departs from the base sensor presented in the previous three chapters and examines the system when augmented with alternate inertial sensor combinations and under alternate structures. The system is first augmented with gyroscopes to examine their effects on the performance. The relative accelerometer is then replaced with a redundant set of accelerometers and the systems performance examined. An alternate sensor structure is then proposed and examined, which is finally followed by a brief exploration of the use of redundant gyroscopes.

A final conclusion then discusses the findings of the work.

Chapter 2

Literature Review

2.1 Existing Joint Sensing Methods

Many approaches to obtaining rotary position and velocity information are available, with the majority of these methods relying on rotary encoders to obtain an estimate of the joint's rotational position. Classic methods rely on differentiation of the joint position to obtain velocity, with some extending to robust differentiators and other numerical approaches. The drawbacks of systems based on differentiation have prompted researchers to investigate other means of obtaining velocity and acceleration estimates. Methods incorporating observers or Kalman filters have shown improved results, however many of these do not typically extend beyond obtaining joint position and velocity. Alternative approaches exploiting the glut of low cost MEMs inertial sensors have also enjoyed recent research. Typical applications of these systems tend toward replacing positional encoders with MEMs devices. Further works have gone on to augment positional encoders with the MEMs sensors in order to improve position and velocity estimates, with some works extending to estimate joint acceleration.

This chapter reviews a number of common methods employed in obtaining joint state information. What is found within this review is that many of the existing methods aim toward improving estimates of joint position and velocity, with only a very small number working to estimate joint acceleration. The systems that do estimate joint acceleration tend to rely heavily on full machine dynamics and kinematics models.

2.2 Classical Methods, Observers and Estimators

Classical velocity estimation methods typically rely on the differentiation of positional encoder data and can be divided into three methods (Petrella et al. 2007); frequency measurement, in which encoder pulses are counted in a fixed time step; period measurement, where the time between encoder pulses is measured, and a mix of the two. All three methods exhibit performance issues primarily based on quantisation noise and a loss of accuracy at low speeds. Low pass filtering can be adopted to reduce the steady state and quantisation errors, however these methods introduce a large phase lag (Zhu and Lamarche 2007) which limits the performance of the control loop. Low speed accuracy can be improved by combining period and frequency measurement but microprocessor timer limitations and quantisation noise still hinder performance. Due to these limitations differentiation methods are generally limited to measuring velocity and not extended into measuring acceleration.

Closed loop observer approaches have also been applied in the estimation of robotic joint states. These systems are beneficial in that the periodic computational requirements

are low and the observer accuracy is limited by the numerical precision of the computer (Baran et al. 2012). An encoder is typically used to obtain position and velocity estimates, however depending on the observer model employed acceleration estimates may also be obtained, although in this case extra information may be required. For example the system analysed by Baran et al. (2012) was able to estimate the velocity and acceleration of an electric motor, but relied on reference current information along with rotor positional information. Observer based systems rely on accurate models of the plant under consideration and these parameters that describe the plant must be accurately obtained and may also vary during the operation of the machine (Petrella et al. 2007). Inaccurate or varying parameters may lead to reduced observer performance and incorrect state estimates.

An alternative approach to observers is the application of Kalman filters (Shaowei and Shanming 2012). These estimators appear in both their linear forms where a measurement is taken directly from an encoder and the state is propagated via simple Euler integration (Bellini et al. 2003; Shaowei and Shanming 2012) or as non-linear estimators, where the $sin - cos$ components of the encoder position are estimated (Petrella et al. 2007). Both of these formulations result in some estimate of the angular velocity, with the system depicted in Bellini et al. (2003) extending to obtain some estimate of angular acceleration. Kalman filter based systems are useful in state estimation as they are tolerant of system model and measurement errors (Petrella et al. 2007). The output accuracy of the estimator is also independent of the sensor resolution and an estimate of the states can be made available during short periods when no sensor measurement is available. This allows the estimators to operate and provide output at a higher rate than the measuring sensor is capable of delivering. Despite these benefits Kalman filter based systems are subject to high computational cost that scales with the number of states being estimated or measured. The accuracy and convergence times of the filters are also affected by parameter choices (Petrella et al. 2007).

Numerical methods have also been applied successfully to encoder based position data in order to obtain estimates of velocity. Methods including robust differentiation or integration (Su et al. 2005) and curve fitting (Chen et al. 2012) have shown promising results, however these methods all appear to be directed at finding velocity estimates and are still highly dependent on encoder resolution and sampling rate.

2.3 Mechanical Sensors

A small number of mechanical devices dedicated to measuring angular acceleration are detailed in the literature. In early works Godler et al. (1995) details the development of a rotary angular acceleration sensor. The device discussed in this work relies on a pair of discs, one being a fixed reference and the other attached to the rotating shaft via flexures, that deviate slightly when exposed to accelerations. The discs are fabricated with slit patterns that when rotated coaxially and relative to one another produce a moire effect that transforms the slight relative rotational displacement of the discs to a more pronounced vertical displacement that is then measured via optical sensors. While successful operation of the device is demonstrated its reliance on the flexure discs renders the sensor an inherently inertial device and as such is subject to influence from external accelerations. Without a means of estimating the angular acceleration of the reference body, this device may only be suitable for measuring the angular acceleration of stationary installations.

The device developed in Kuzma and Kalas (2001) too relies on the motion of discs moving relative to one another. In this system the angular acceleration is related to the torsional torque between two sets of discs with opposing magnets. The device is configured

such that any angular acceleration applied results in a torsional torque between the two magnet discs, with the angular displacement as a result of the torque being measured to estimate the angular acceleration. Like the system in Godler et al. this device is too subject to the influence of external acceleration and requires some reference body.

The sensors described in Zhao and Feng (2015) and Restivo et al. (2012) are true relative angular acceleration sensors. Simply put, the devices are both based on moving a disc or a cup through a magnetic field generated by permanent magnets and the successful operation of both devices is demonstrated in the papers.

While these sensors have all been shown to operate successfully they exhibit a number of drawbacks that may render them undesirable for robotics applications. When compared to a robotic joint, all the sensors are potentially physically large. Three of the sensors make use of permanent magnets which adds mass and all four sensors require some form of housing and must be mounted coaxially. The coaxial mounting of the permanent magnet based devices moves away from the general trend in robotics of mounting devices of significant mass toward the base and away from the moving links. All the devices require bearings and as Kuzma and Kalas notes, the friction from the bearings introduces dead zones into the sensor operation. Some of the devices exhibited non-linearity issues across their measurement range, and finally when viewed in a robotics context the devices that do not measure true relative acceleration will require some means of estimating the previous link acceleration.

2.4 MEMs Sensors

In recent times abundant access to low cost MEMs inertial sensors have enabled obtaining some estimate of velocity or acceleration directly from a sensor, rather than via numerical differentiation. These devices are physically small and light weight, reasonably low in electrical power requirements and are low in cost and highly available due to their wide spread adoption in modern mobile devices. Due to this, these sensors are an attractive means of obtaining inertial information and as such are actively being researched in a robotics context.

The approaches to employing MEMs inertial sensors within robotics control and estimation systems are varied. In their survey Cheng and Oelmann (2010) discuss four methods in which joint positional information may be extracted from combinations of MEMs gyroscopes and accelerometers. Similarly, Quigley et al. (2010) demonstrates that users may trade off measurement precision with the low cost of inertial sensors, depending on the intended machine task. Both of these works demonstrate that depending on the precision and accuracy required, the positional encoders typically found in robotic joint systems may be completely replaced with accelerometer and gyroscope based position estimation systems. Although capable of estimating positional information these methods that rely solely on gyroscopes and accelerometers are subject to some drawbacks. In obtaining positional estimates the previous mentioned works rely on integration or differentiation of the gyroscopes output and on the accelerometers ability to measure acceleration due to gravity under reasonably static conditions. The outputs of the gyroscope integration or differentiation and the accelerometer output are then combined in some manner, typically a complementary filter (Colton 2007) to obtain the positional estimate. Cheng and Oelmann (2010) discussed issues in the integration or differentiation processes when applied to the gyroscope output. The result of this was introduction of unbounded noise in the case of the integration process and bounded noise when differentiating, with both resulting in decreased system performance when estimating the position during dynamic movements. Finally, Cheng and Oelmann remarked that when deploying accelerometers for position estimation it is not possible to

resolve any rotation that is normal to the gravity vector, with extra sensors being required to estimate these quantities. Unfortunately this situation arises frequently in fixed base robotic systems.

These systems described primarily presented a low cost alternative to replacing positional encoders and while this is useful, these methods do not address the need for estimating the higher order terms.

Alternative system configurations have been proposed whereby the MEMs sensors are combined in some manner with the positional encoder. Kubus et al. (2012) aimed to improve joint angle and angular rate estimates by reducing quantisation noise through the fusing of encoder signals and MEMS gyroscopes via a complementary filter. This work, along with the previously mentioned work by Cheng and Oelmann (2010) discussed the requirement for gyroscopes to be placed on each link, with the difference between them resulting in the particular joint's angular velocity. Kubus et al. (2012) demonstrates improved results over that of a differentiated encoder in a closed loop robot control experiment, however the work also notes there are some tweaking factors involved that are dependent on the placement of the gyroscopes on the robot links. Zhu and Lamarche (2007) also worked toward improving angular velocity estimates by incorporating a single three axis accelerometer into the tool tip of a single link robot. Within this they were able to improve the joint space velocity estimation by tasking the accelerometer with estimating the high frequency velocity components and the position encoder with the low frequency components. Axelsson et al. (2012) went on to incorporate a linear acceleration measurement from an accelerometer into a particle filter system in order to better the estimate of the tool tip position. Both of these works move away from using the accelerometer to solely measure acceleration due to gravity and push further toward incorporating the measurements into the actual dynamics of the robotic system. Unfortunately, the works do not extend beyond obtaining or improving position or velocity estimates.

Following on from single devices placed at tool tips, work into effectively 'lacing' all the links or joints of a robotic system with inertial sensors is under way. These systems typically employ whole Inertial Measurement Units (IMUs), comprised of single three axis gyroscopes, accelerometers and magnetometers placed on each link of the robot and are generally networked in some manner to allow sampling from all devices during a time interval. It is primarily within these systems that we see extension into estimating higher order states.

In their work on large hydraulic back hoe style machines Honkakorpi (2014) worked to replace expensive encoders with inertial sensors placed on each link of the machine. In a similar manner to the previous gravity based methods, this work too relied on complementary filtering of gyroscope data and measurements of acceleration due to gravity to estimate joint positions. However, this work was also extended to extract both angular velocity and acceleration from the inertial sensors[1]. The angular acceleration data was then successfully used in a control loop, which was constructed primarily to increase the system damping in order to reduce the oscillations present in the long links.

Systems employing IMUs on all links also appear in research into humanoid robotics. Rotella et al. (2016) placed single IMUs on each link of their humanoid robot and fused the gyroscope and accelerometer data from the IMUs with measurements obtained from encoders in an effort to estimate rotary joint position, velocity and acceleration. In a similar manner to Honkakorpi, this work relied on a kinematic model of the whole robot to extract the angular velocity and acceleration components from the distributed gyroscopes

[1]The details of this are covered in Section 2.5.

and accelerometers. Rotella et al. demonstrated that the system would increase control system performance, however rather than relying on the measured angular acceleration they resorted to using the commanded acceleration, noting performance would have been better had they used the measured acceleration.

This choice of employing commanded acceleration over that of the measured acceleration came about due to their use of a single accelerometer per link. Rotella et al. showed that at least two accelerometers (in their case IMUs) would be required *per link* in order to estimate the angular acceleration, however they did not test the performance of their system in this configuration. Honkakorpi had accounted for this in their work and employed two IMUs per link to estimate the angular acceleration, demonstrating positive results. Although, this work was based on a planar system and they noted that a third accelerometer per link would be required to extend into three dimensions.

2.5 Accelerometer Only IMU

It is the idea that an IMU employing only a single accelerometer is not capable of producing an angular acceleration estimate that leads to the Accelerometer Only IMU (AO-IMU).

Whereas the previous work discussed (Honkakorpi 2014; Rotella et al. 2016; Xinjilefu 2015) employed multiple IMUs and full robot kinematic and dynamic models to obtain their angular acceleration estimate, the AO-IMU can be thought of as a single IMU that is capable of producing both angular acceleration and velocity estimates without the need for a whole robot model. It is this capability that makes these devices attractive when considering the estimation of higher order rotational joint states.

The AO-IMU concept is based around fixing arrays of accelerometers at known positions and orientations to a single rigid body. Then from the relationship for acceleration of a point on a rigid body the linear acceleration and angular acceleration and velocity components can be extracted.

The use of linear accelerometers to measure rotational acceleration and velocity has been the subject of research since the 1960*s*. In early works arrays of six and nine accelerometers were employed to estimate the acceleration and velocity components of rigid bodies (Grammatikos 1965; Padgaonkar et al. 1975). Those methods incorporating six accelerometer measurements employed integration to estimate angular velocity (Padgaonkar et al. 1975). The estimated angular velocity was then relied upon to obtain the new angular acceleration estimate for the next time step and as such the use of integration led to poor performance in the devices. These devices were subsequently augmented to employ nine accelerometers (Padgaonkar et al. 1975) and in these configurations the angular acceleration could be derived directly from the measurements at each time step however, integration was still required to estimate the angular velocity.

Subsequent works have gone on to demonstrate that by incorporating a minimum of 12 acceleration measurements it was possible to directly measure both the angular acceleration and components of the angular velocity (Zappa et al. 2001). These devices serve as the basis for the modern AO-IMU as it stands today.

Modern accelerometers are widely available in packages whereby three mutually orthogonal axes are present on the same device. Further AO-IMU works have gone on to exploit these packages. In these works Lin and Ho (2009), Schopp et al. (2010), and Madgwick et al. (2013) demonstrated that unlike the schemes presented in Padgaonkar et al., systems employing the triple axis devices do not need specific geometric configurations, only that the placement and orientation are known. Although these particular array configurations

present great flexibility in their geometric configuration, there are some considerations that must be addressed.

The general formulation of the modern AO-IMU relies the kinematic equation for acceleration of a rigid body

$$\boldsymbol{a}_m = \boldsymbol{a}_o + \dot{\boldsymbol{\omega}} \times \boldsymbol{r} + \boldsymbol{\omega} \times (\boldsymbol{\omega} \times \boldsymbol{r}), \tag{2.1}$$

where $\boldsymbol{a}_o$ is the body's linear acceleration, $\dot{\boldsymbol{\omega}}$ and $\boldsymbol{\omega}$ are the angular acceleration and velocity and $\boldsymbol{r}$ are the known accelerometer positions. The vector $\boldsymbol{a}_m$ represents one triple axis accelerometer measurement. An equation for each three axis accelerometer is then stacked into a vector and the subsequent system is reformulated into a matrix equation of the form

$$\boldsymbol{a} = \boldsymbol{B}\boldsymbol{x}, \tag{2.2}$$

where $\boldsymbol{a}$ is the vector of stacked acceleration measurements, $\boldsymbol{x}$ are the unknown and time varying linear acceleration and angular acceleration and velocity components and the matrix $\boldsymbol{B}$ is made up of the known accelerometer positions. The unknown values $\boldsymbol{x}$ may then be found as a solution to this equation.

The quality of the output of the AO-IMU then becomes dependent on the condition of the matrix $\boldsymbol{B}$ and its suitability for inversion. A number of works have investigated these properties and as such guidelines for the optimal placement of the accelerometers are available. Lu and Lin (2011) showed that while it is not strictly necessary for successful operation, a cube structure centred about the origin o with the accelerometers being placed at the cube's opposing corners offers the best performance. Madgwick et al. (2013) went on to demonstrate that the performance of the AO-IMU becomes dependent on the volume the cube occupies. Within this it was shown that the error of the kinematic states $\dot{\boldsymbol{\omega}}$ and $\boldsymbol{\omega}^2$ are independent of the sensor's distance to the origin, but inversely proportional to the separation between the sensors themselves. In practice an overall increase in the volume of the sensor occupying cube and in turn separation of the sensors should be aimed for. Indeed Lin, Komsuoglu, et al. (2006) explicitly noted that the small volume that their AO-IMU occupied severely limited the performance of their system and they had to rely on gyroscopes for the angular velocity measurements. Madgwick et al. also discussed issues regarding the systems capability of estimating low angular velocities, noting that sensor measurement and alignment errors will result in bias errors that present primarily at these low angular velocities and that at these low angular velocities, sensor noise may become an issue.

Following this, a final issue regarding the performance AO-IMU is the estimation of the angular velocity state. In the typical AO-IMU both the linear and angular acceleration terms are available directly from the vector $\boldsymbol{x}$ however, the angular velocities appear as non-linear terms, both as quadratics and functions of one another. This is a well studied issue (Lu and Lin 2011; Cardou et al. 2011; Schopp et al. 2010; Ciblak 2007; Lu and Lin 2011) with the majority of solutions tending toward the use of Kalman style estimators or optimisation methods to find the actual angular velocity.

Although the AO-IMU has a couple of considerations and issues required to enable its successful operation, they are not insurmountable. The device's capability of directly measuring both angular acceleration and angular velocity makes it attractive for investigation in use in estimating higher order robotic joint states.

2.6 Summary and Research Aims

This review has examined the current state of robotic joint sensing, in particular the sensing methodologies currently in use when attempting to estimate the joint's position, velocity and in some cases acceleration. It is evident from the literature that researchers are indeed pushing toward incorporating higher order derivatives of joint position into their control systems and parameter estimation systems. What was found however, that those utilising these higher order derivatives such as acceleration are often relying on differentiation, estimates from models that may vary over time and other such means that offer poor estimates. The review then focussed on joint state measuring technologies. Within this it was found that the classical methods that rely on differentiation were not suited to estimating higher order states due to the inherent noise and phase lag, and those systems that employed observers and Kalman filters did not estimate higher order derivatives. Those that did found that extra information other than the information from the positional encoder was required.

The review then examined the state of mechanical acceleration sensors and found a number of solutions. The devices investigated were then either found to not measure true relative acceleration, be physically bulky and heavy due to their reliance on permanent magnets, or suffer from non-linearities.

The use of MEMs devices was then next examined. It was found that these devices showed promise when measuring acceleration and velocity directly. However, the literature showed that many of the works involving these devices aimed to employ them as a replacement for positional encoders, forgoing any estimates of the higher order terms. A few works had moved beyond this and begun employing the MEMs devices in conjunction with positional sensors to increase the performance of position and velocity estimates. Only once the works that pushed to 'lace' a whole robot with inertial sensors were introduced, did work into estimating joint acceleration terms really take hold. These systems showed positive results however, they all relied on full dynamic or kinematic models of the robot and that each robot link be instrumented with IMUs.

From here the AO-IMU was introduced as an means of obtaining estimates of joint acceleration and velocity *without* requiring any kinematic or dynamic model of the whole robot. A brief background on the device was delivered, as was an introduction into the basic operation of the concept. Finally, the issues surrounding the successful implementation of the device were discussed.

This review has highlighted a gap in robotic joint sensor technology. It was shown that although researchers wish to employ acceleration terms into their works, no good quality means of obtaining this information is readily available. The AO-IMU concept offers both velocity and acceleration estimates in an inertial frame and as such, by itself the device is not suited to joint state estimation. With extra work and by incorporating sensor fusion methods by means of Kalman style filters, the acceleration and velocity estimates obtained from the AO-IMU might be combined with position measurements from a rotary encoder. In doing so estimates of the joint's position, velocity and acceleration can be made available with no reliance on the robot's kinematic or dynamic model.

The primary aim of this work is to investigate the effectiveness of the AO-IMU concept in enabling the estimation of a robotic joints rotary position, velocity and acceleration.

In building on the base sensor system it is then aimed to investigate the effects of alternate combinations of MEMs accelerometers and gyroscopes on the system. We also look at alternate structures and their suitability on larger robotic systems.

Chapter 3

System Modelling

3.1 Introduction

In this chapter the kinematic models that define the operation of the joint sensor and calibration and alignment procedures required to compensate for the shortcomings of the inertial sensors are presented. Section 3.2 describes the inertial sensor and incremental encoder models. This is followed by the development of models describing the kinematics of the joint sensor system in Section 3.3. An accelerometer only IMU (AO-IMU) is first defined in Section 3.3.1 and is employed to obtain estimates of the linear acceleration and angular velocity and acceleration of a robotic link l_i.The system is then extended in Section 3.3.2 by considering an accelerometer attached to the previous robotic link l_{i-1} and the kinematics for obtaining the relative angular acceleration and velocity are obtained. The system modelling covers the general case for any rotational robotic joint with the specific case being examined once the general kinematics are defined.

3.2 Sensor Models

3.2.1 Accelerometer Model

An accelerometer measures real inertial acceleration such that

$$ {}^{i}\boldsymbol{a} = \boldsymbol{S}_a \, {}^{i}_{I}\boldsymbol{R}({}^{I}\boldsymbol{a} + {}^{I}\boldsymbol{g}) + {}^{i}\boldsymbol{b}_a + {}^{i}\boldsymbol{v}_a, \tag{3.1} $$

where $\boldsymbol{S}_a$ is a matrix representing the gain and off-axis effects of each axis of the accelerometer, the matrix ${}^{i}_{I}\boldsymbol{R}$ rotates quantities expressed in the inertial frame into the local sensor frame j, ${}^{I}\boldsymbol{a}$ is the acceleration in the inertial frame I as measured by the accelerometer and ${}^{I}\boldsymbol{g} = \begin{bmatrix} 0 & 0 & g \end{bmatrix}^{\mathsf{T}}$ is the gravity vector, with $g = -9.81$. The vector ${}^{i}\boldsymbol{v}_a$ represents the sensor noise and ${}^{i}\boldsymbol{b}_a$ contains the accelerometer bias terms. It is assumed the inertial frame I is oriented such that it's $\hat{\boldsymbol{z}}$ axis is in the direction $-g$.

The gain and off-axis parameters described by the matrix $\boldsymbol{S}_a$ and the bias terms in ${}^{i}\boldsymbol{b}_a$ are typical of a common MEMs accelerometer. These terms detrimentally affect the performance of the accelerometers and will lead to a reduction in the performance of a system that is reliant on them for accurate inertial information. Fortunately a simple calibration procedure as outlined in Section 5.4.1 is sufficient to compensate for these effects and once compensated for, the accelerometer model (5.6) can be simplified to

$$ {}^{i}\boldsymbol{a} = {}^{i}_{I}\boldsymbol{R}({}^{I}\boldsymbol{a} + {}^{I}\boldsymbol{g}) + {}^{i}\boldsymbol{v}_a. \tag{3.2} $$

Within this work the experimental time frames are short and as such accelerometer moving bias and temperature dependent effects are not considered.

3.2.2 Gyroscope Model

While the joint sensor system is not dependent on gyroscope sensors, the system is augmented to include them in later experiments. We also aim to compare the performance of the joint sensor system to those systems incorporating the use of gyroscope sensors. A MEMs gyroscope measures real inertial angular velocity and as with the accelerometer it too will suffer from some level of bias and cross axis effects inherent to the device design. A gyroscope can be described by the model

$$ {}^{i}\boldsymbol{g} = \boldsymbol{S}_g \, {}^{i}_{I}\boldsymbol{R}^{I}\boldsymbol{\omega} + {}^{i}\boldsymbol{b}_g + {}^{i}\boldsymbol{v}_g, \tag{3.3} $$

where $\boldsymbol{S}_g$ is a matrix of gain parameters, ${}^{I}\boldsymbol{\omega}$ is the true angular velocity in the inertial frame and ${}^{i}\boldsymbol{v}_g$ is the sensor noise vector. The vector ${}^{i}\boldsymbol{b}_g$ describes the gyroscope bias terms.

As with the accelerometer, the gains in the matrix $\boldsymbol{S}_g$ along with the bias terms in ${}^{i}\boldsymbol{b}_g$ can found via the simple calibration procedure, similar to that covered in Section 5.4.2. In aligning the device and removing the bias, the gyroscope can be described by the simplified model

$$ {}^{i}\boldsymbol{g} = {}^{i}_{I}\boldsymbol{R}^{I}\boldsymbol{\omega} + {}^{i}\boldsymbol{v}_g. \tag{3.4} $$

As the experimental time frames are short the moving bias and temperature effects need not be considered.

3.2.3 Encoder Model

In this work a 16 bit incremental encoder is employed obtain the relative angle between two links. Within this the encoder is modelled as taking the real angle as seen from link l_i and augmenting it with a noise term as

$$ {}^{i}\theta_{\text{enc}} = S_e({}^{i}\theta_{\text{real}} + {}^{i}v_e), \tag{3.5} $$

where S_e simply scales the raw encoder output ${}^{i}\theta_{\text{real}}$ counts to radians.

Although not strictly correct the encoder noise is considered as zero mean white noise. As outlined later, this allows the use of a computationally efficient form of the UKF. The results will show that this assumption is sufficient, however future work might consider the effects of this choice on the performance of the system. As the quantisation noise is negligible for this application the encoder signal is not filtered. Further details on the encoder are presented in 5.2.2.2.

In the remainder of the work, the subscript of a vector expressed in its own frame is dropped. For example ${}^{i}\dot{\boldsymbol{\omega}}_i = {}^{i}\dot{\boldsymbol{\omega}}$.

3.3 Kinematic Models

For any two series robotic links l_i and l_{i-1} hinged about point o we wish to obtain the relative joint position, velocity and acceleration. In this it is assumed that for the a general case the joint is not constrained to rotate about a single axis and it is also assumed that the positions of all the inertial sensors are known[1].

The kinematic modelling of the joint sensor system is split into two major components. First an accelerometer only inertial measurement unit is attached to link l_i and defines the linear and angular acceleration and the angular velocity of that link in an inertial frame. The system is then extended to define the same components for the previous link l_{i-1} by

[1] Within reason, small misalignments in the sensor positions will be compensated for.

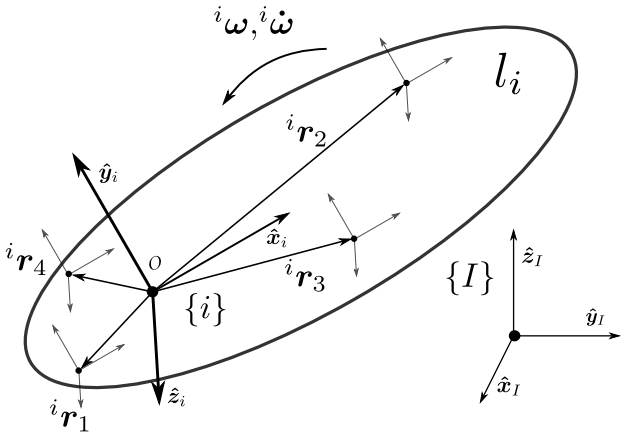

Figure 3.1: Accelerometer only IMU.

incorporating a single three axis accelerometer placed on this link, along with an incremental encoder which reads the relative position between the links. Once the angular velocities and accelerations of links l_i and l_{i-1} are known, the rule of summation of angular velocities and its derivative is employed to extract the relative joint acceleration and velocity.

3.3.1 Accelerometer-Only IMU Model

The accelerometer only IMU formulation typically involves fixing arrays of accelerometers arranged in specific three dimensional spatial patterns to a body of interest. The schematic in Figure 3.1 depicts four tri-axial accelerometers placed on a body l_i at points $^i\boldsymbol{r}_j$, where $j = 1, 2, 3, 4$. The acceleration of a point j on a rigid body l_i can be described by

$$^i\boldsymbol{a}_j = {}^i\boldsymbol{a}_o + {}^i\dot{\boldsymbol{\omega}} \times {}^i\boldsymbol{r}_j + {}^i\boldsymbol{\omega} \times ({}^i\boldsymbol{\omega} \times {}^i\boldsymbol{r}_j), \tag{3.6}$$

with the link's linear acceleration $^i\boldsymbol{a}_o$, angular acceleration $^i\dot{\boldsymbol{\omega}}$ and the angular velocity $^i\boldsymbol{\omega}$ being unknown and the known sensor position j relative to body i's origin o being given by the vectors $^i\boldsymbol{r}_j$. For the sake of simplicity the vectors from (3.6) are reduced to their components and are written as

$$\begin{aligned} ^i\boldsymbol{a}_o &= \begin{bmatrix} a_x & a_y & a_z \end{bmatrix}^\mathsf{T}, \\ ^i\dot{\boldsymbol{\omega}} &= \begin{bmatrix} \dot{\omega}_x & \dot{\omega}_y & \dot{\omega}_z \end{bmatrix}^\mathsf{T}, \\ ^i\boldsymbol{\omega} &= \begin{bmatrix} \omega_x & \omega_y & \omega_z \end{bmatrix}^\mathsf{T}, \\ ^i\boldsymbol{r}_j &= \begin{bmatrix} r_x & r_y & r_z \end{bmatrix}^\mathsf{T}. \end{aligned} \tag{3.7}$$

Once the kinematic equation of motion for acceleration *for each accelerometer measurement* is applied, the problem can be manipulated further (Schopp et al. 2010) to be written as the

matrix equation

$$
{}^{i}\boldsymbol{a}_j = \begin{bmatrix} 1 & 0 & 0 \\ 0 & 1 & 0 \\ 0 & 0 & 1 \\ 0 & -r_z & r_y \\ r_z & 0 & -r_x \\ -r_y & r_x & 0 \\ r_y & r_x & 0 \\ r_z & 0 & r_x \\ 0 & r_z & r_y \\ 0 & -r_y & -r_z \\ -r_x & 0 & -r_z \\ -r_x & -r_y & 0 \end{bmatrix}^{\mathsf{T}} \begin{bmatrix} a_x \\ a_y \\ a_z \\ \dot{\omega}_x \\ \dot{\omega}_y \\ \dot{\omega}_z \\ \omega_x\omega_y \\ \omega_x\omega_z \\ \omega_y\omega_z \\ \omega_x^2 \\ \omega_y^2 \\ \omega_z^2 \end{bmatrix} = \boldsymbol{B}_j\boldsymbol{x}, \tag{3.8}
$$

where the invariant acceleration position ${}^{i}\boldsymbol{r}_j$ forms the matrix $\boldsymbol{B}_j$ and the linear and angular accelerations, and angular velocities form the time varying vector $\boldsymbol{x}$.

The body motion in (3.6) is described by the vector parameters ${}^{i}\boldsymbol{a}_o$, ${}^{i}\dot{\boldsymbol{\omega}}$ and ${}^{i}\boldsymbol{\omega}$ which are comprised of nine unknown components. A recurring and well studied issue (Lin, Komsuoglu, et al. 2006; Schopp et al. 2010) in the formulation of the AO-IMU is that the angular velocity components in (3.8) appear in both quadratic form and as products of them selves and one another. With only nine sensors it is not possible to find a unique solution for ${}^{i}\boldsymbol{\omega}$ (Schopp et al. 2010) and as such 12 sensor are deployed as four three-axis accelerometers. The four three axis accelerometers are installed onto the link at positions ${}^{i}\boldsymbol{r}_j$, with $j = 1, 2, 3, 4$ and the measurements ${}^{i}\boldsymbol{a}_j$ and position matrix $\boldsymbol{B}_j$ stacked as

$$
\boldsymbol{y} = \begin{bmatrix} \boldsymbol{a}_1 & \boldsymbol{a}_2 & \boldsymbol{a}_3 & \boldsymbol{a}_4 \end{bmatrix}^{\mathsf{T}}, \tag{3.9}
$$

and

$$
\boldsymbol{B} = \begin{bmatrix} \boldsymbol{B}_1 & \boldsymbol{B}_2 & \boldsymbol{B}_3 & \boldsymbol{B}_4 \end{bmatrix}^{\mathsf{T}}, \tag{3.10}
$$

which results in a matrix equation of the form

$$
\boldsymbol{y} = \boldsymbol{B}\boldsymbol{x}, \tag{3.11}
$$

from which a solution might be found for $\boldsymbol{x}$.

The structure matrix $\boldsymbol{B}$ is solely a function of the accelerometer positions ${}^{i}\boldsymbol{r}_j$ (Lu and Lin 2011) and as such extracting the vector $\boldsymbol{x}$ becomes dependent on the numerical condition of $\boldsymbol{B}$. In turn, the numerical condition of $\boldsymbol{B}$ is dependent on the geometrical structure the accelerometer array forms when fixed to a rigid body. The literature shows (Lu and Lin 2011; Madgwick et al. 2013; Schopp et al. 2010) that three dimensional structures are required to ensure linear independence of the rows of $\boldsymbol{B}$ and as such systems employing planar structures are not capable of recovering $\boldsymbol{x}$ as $\boldsymbol{B}$ becomes rank deficient. Lu and Lin; Madgwick et al. go on to demonstrate that cube structures with the accelerometers placed at opposing corners offer the best performance in AO-IMU formulations. General guidelines advise placing the origin o at the centre of the cube structure, while maximising the structure's volume. In this work the four accelerometers are placed in a cuboid manner, with the forward accelerometers extending up the link's $\hat{\boldsymbol{x}}$ axis. This is covered further in Section 5.2.1.

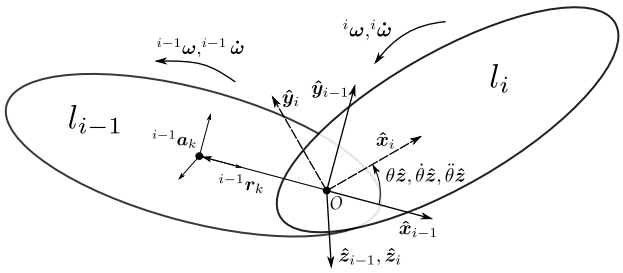

Figure 3.2: Relative kinematics.

3.3.2 Relative Acceleration Model

The AO-IMU system derived in Section 3.3.1 fully defines the angular acceleration and velocity of the link l_i in the inertial frame. However, in robotics applications it is more useful to know the angular acceleration, velocity and position of the link l_i relative to the previous link l_{i-1}. In this section the AO-IMU concept is built upon to obtain the relative joint state information. In doing this an extra accelerometer is placed on the previous link l_{i-1} and the acceleration obtained from this sensor, along with information obtained from the AO-IMU, is employed to derive the relative joint acceleration and velocity. Within this section it is assumed that issues regarding recovering the angular velocity from the AO-IMU are accounted for and the linear and angular acceleration vectors ${}^{i}\boldsymbol{a}_o$ and ${}^{i}\dot{\boldsymbol{\omega}}$, along with the angular velocity vector ${}^{i}\boldsymbol{\omega}$ are fully available.

As in Section 3.3.1 obtaining the relative components is based on finding the acceleration of a point on on a rigid body. The acceleration of this point k on the relative link l_{i-1} can be described by

$$ {}^{i-1}\boldsymbol{a}_k = {}^{i-1}\boldsymbol{a}_o + {}^{i-1}\dot{\boldsymbol{\omega}} \times {}^{i-1}\boldsymbol{r}_k + {}^{i-1}\boldsymbol{\omega} \times ({}^{i-1}\boldsymbol{\omega} \times {}^{i-1}\boldsymbol{r}_k), \tag{3.12} $$

again with the linear acceleration ${}^{i-1}\boldsymbol{a}_o$, angular acceleration ${}^{i-1}\dot{\boldsymbol{\omega}}$ and angular velocity ${}^{i-1}\boldsymbol{\omega}$ being unknown and the known sensor position k relative to link l_{i-1}'s origin o being given by ${}^{i-1}\boldsymbol{r}_k$.

With only one accelerometer (3.12) cannot be directly solved. However as the acceleration and velocity of l_i have been defined previously, we seek to express the quantities in l_{i-1} in terms of those in l_i. Referring to Figure 3.2 the two links l_i and l_{i-1} are constrained to rotate about a point at o. This constraint is typical of serial robotic systems and in this case enables propagation of the quantities to the previous link, given that the rotation is known. The acceleration vector ${}^{i-1}\boldsymbol{a}_o$ is coincident with ${}^{i}\boldsymbol{a}_o$ but simply rotated by some quantity as

$$ {}^{i-1}\boldsymbol{a}_o = {}^{i-1}_{i}\boldsymbol{R}\ {}^{i}\boldsymbol{a}_o. \tag{3.13} $$

The angular velocity of link l_{i-1} can be related to the angular velocity of link l_i through the summation of angular velocities as

$$ {}^{i}\boldsymbol{\omega} = {}^{i}\boldsymbol{\omega}_{i-1} + {}^{i}\boldsymbol{\omega}_{i-1,i}, \tag{3.14} $$

where ${}^{i}\boldsymbol{\omega}_{i-1,i}$ is the angular velocity of link l_{i-1} relative to i in frame i. Rearranging and rotating into frame $i-1$ gives

$$ {}^{i-1}\boldsymbol{\omega} = {}^{i-1}_{i}\boldsymbol{R}({}^{i}\boldsymbol{\omega} - {}^{i}\boldsymbol{\omega}_{i-1,i}). \tag{3.15} $$

To obtain a similar relationship for angular acceleration, (3.14) is differentiated to give

$$ {}^{i}\dot{\boldsymbol{\omega}} = {}^{i}\dot{\boldsymbol{\omega}}_{i-i} + {}^{i}\dot{\boldsymbol{\omega}}_{i-1,i} + {}^{i}\boldsymbol{\omega}_{i-1} \times {}^{i}\boldsymbol{\omega}, \tag{3.16} $$

where ${}^{i}\dot{\boldsymbol{\omega}}_{i-1,i}$ is the angular acceleration of link l_{i-1} relative to i, expressed in frame i. Rearranging and rotating into frame $i-1$ gives

$$ {}^{i-1}\dot{\boldsymbol{\omega}} = {}^{i-1}_{i}\boldsymbol{R}({}^{i}\dot{\boldsymbol{\omega}} - {}^{i}\dot{\boldsymbol{\omega}}_{i-1,i} - {}^{i}\boldsymbol{\omega}_{i-1} \times {}^{i}\boldsymbol{\omega}). \tag{3.17} $$

These equations represent a generalised form of the relative accelerometer model. For the specific case in this work, links l_i and l_{i-1} are rotational robotic joints and are constrained to rotate about the local $\hat{\boldsymbol{z}}$ axis in as shown in Figure 3.2. In this case the rotation can be described by

$$ {}^{i-1}_{i}\boldsymbol{R} = \boldsymbol{R}_z(\theta), \tag{3.18} $$

where $\boldsymbol{R}_z(\theta)$ is the rotation matrix

$$ \boldsymbol{R}_z(\theta) = \begin{bmatrix} \cos(\theta) & -\sin(\theta) & 0 \\ \sin(\theta) & \cos(\theta) & 0 \\ 0 & 0 & 1 \end{bmatrix}, \tag{3.19} $$

and θ represents the joint angle obtained from an encoder measurement.

As this rotation is constrained about the $\hat{\boldsymbol{z}}$ axis the angular velocity and acceleration components in (3.15) and (3.17) are independent of the rotational angle, and consequently the cross product term in (3.17) reduce to zero.

The relative angular velocity and acceleration about the local $\hat{\boldsymbol{z}}$ axis can then be expressed as

$$ \begin{aligned} {}^{i}\boldsymbol{\omega}_{i-1,i} &= \dot{\theta}\hat{\boldsymbol{z}} \\ {}^{i}\dot{\boldsymbol{\omega}}_{i-1,i} &= \ddot{\theta}\hat{\boldsymbol{z}}, \end{aligned} \tag{3.20} $$

and the relative kinematic relationship for this work can be given as

$$ \begin{aligned} {}^{i-1}\boldsymbol{\omega}_{i-1} &= {}^{i-1}_{i}\boldsymbol{R}({}^{i}\boldsymbol{\omega}_{i} - \dot{\theta}\hat{\boldsymbol{z}}) \\ {}^{i-1}\dot{\boldsymbol{\omega}}_{i-i} &= {}^{i-1}_{i}\boldsymbol{R}({}^{i}\dot{\boldsymbol{\omega}}_{i} - \ddot{\theta}\hat{\boldsymbol{z}}). \end{aligned} \tag{3.21} $$

These equations are directly employed in the state estimation section 4.4.2.

Chapter 4

State Estimation

4.1 Introduction

In this Section the issues regarding the estimating of the joint sensor states are addressed. In examining the system models in Chapter 3 it is shown that the AO-IMU vector $\boldsymbol{x}$ is not in a form that is directly useful within the sensor system. Specifically issues arises when attempting to recover the angular velocity. Both the linear and angular acceleration are directly available from the vector $\boldsymbol{x}$, however the angular velocity components appear as non-linear terms, both in quadratic forms and as products of one another. This issue is well known in the literature and results in sign ambiguity when attempting to extract the angular velocity components from the AO-IMU state. Ideally the AO-IMU will be fully exploited for its angular acceleration and velocity information and as such some means of recovering both of these states is desirable. In making these states measurable the concept of sensor fusion can be employed, whereby the overall system performance can be improved by incorporating the multiple sensor measurements. The relative component of the joint sensor system can also benefit from the use of state estimators. In a similar manner to the AO-IMU, measurements from both the inertial sensors and the incremental encoder will enable some measurement of relative acceleration, velocity and position and again, we can take advantage of sensor fusion methods to ensure consistency between the states.

The system presented in this section will not require knowledge of the overall robotic system dynamic model, only that the joints be rotational. Due to this the sensor will be robust to dynamics modelling errors or disturbances and as such common robotics tasks such as picking up objects will not reduce the sensor system performance. Finally, all system states are computed from sensor measurements and no knowledge of the robotic state (such as input torques) is required.

4.2 Unscented Kalman Filter

In deriving the sensor system models it is evident that both the AO-IMU component and the relative component are based on some level of non-linear measurement model. A standard Kalman Filter is not suited to the estimation of non-linear systems and as such the Unscented Kalman Filter (UKF) was selected for the sensor fusion task. The UKF does not approximate the non-linear function as in the Extended Kalman Filter (EKF), rather the probability distribution is approximated and propagated through a non-linear model. The UKF is arguably simpler to implement than the EKF as derivations of Jacobian matrices are not required (Van Der Merwe and Wan 2004) and the UKF formulation offers a 3rd order approximation of the non-linear system, whereas the EKF is only capable of 1st order

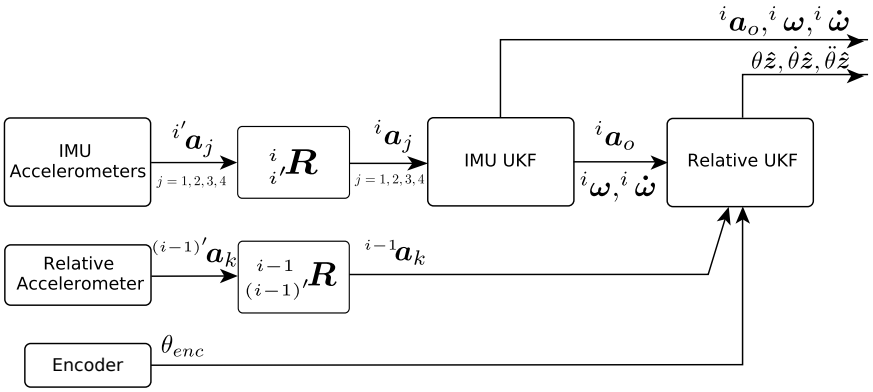

Figure 4.1: Sensor and UKF data flow.

approximations (Van Der Merwe and Wan 2004).

This work does not cover the internal operation of the UKF in depth, rather attention is given to the formulation of the system and the computation considerations required. The UKF is covered in depth by Wan, Van Der Merwe, et al. (2000) and the additive (zero-mean) UKF algorithm employed in this work is presented in Appendix B.

Figure 4.1 depicts the flow of information within the sensor system. The data entering the system from the left is considered scaled and calibrated. The accelerometer measurements are then rotated to ensure body frame alignment before being passed to their respective estimators. Finally the output of the IMU UKF is passed to the relative UKF and the relative states are estimated.

4.3 Computational Considerations

In perusing the literature it has become evident that the EKF is still more common in state estimation systems over the UKF. Unfortunately the computational requirements of the UKF overshadow its ease of implementation and superior performance. However, many variations of the UKF formulation exist. Once calibrated the inertial sensors can be modelled as having zero mean additive noise[1] which enables the use of the additive zero mean UKF formulation (Wan, Van Der Merwe, et al. 2000). In this method the system state does not need to be augmented with noise variables and the dimension of the state vector and the number of sigma points is reduced. Achieving this is straight forward: the covariances of the measurement and state noise are simply added during the time update and measurement update procedure. In making this assumption and employing this specific UKF formulation the complexity of the UKF is reduced to order $O(n^3)$, for n states, which is the same as the EKF.

Early simulation work on a single UKF based system showed that time wise performance degradation was evident due to the large number of states to be estimated. Thus, to reduce the computational requirements further the estimation of the system states is split into two separate and sequential UKF implementations. From Figure 4.1 it is noted that there is a one way flow of information from the AO-IMU to the relative components, in that the relative components depend on data from the AO-IMU but not vice-versa. As such two separate UKF implementations are constructed for the joint sensor system, with the first estimating the states of the AO-IMU and the second estimating the relative components. In doing so the total execution time is reduced from order $O(19^3)$ for a combined formulation

[1] It is worth restating here that this is not strictly correct for the case of the incremental encoder, however the encoder quantisation noise is minimal and thus the assumption is sufficient.

to order $O(4^3) + O(15^3)$ for a split formulation. Further simulation work on the sensor system showed a decrease in simulation execution time, however no study into the effects of the AO-IMU sigma points no longer being propagated through the relative component was carried out. It is suspected that a small decrease in system accuracy may be apparent. Examining these effects is left as future work.

4.4 UKF Implementation

4.4.1 AO-IMU UKF

The AO-IMU UKF implementation enables the estimation of the angular velocity term from the quadratic and product measurements in the vector $\boldsymbol{x}$. In doing this the UKF also enables fusion of the successive states while ensuring that they remain consistent.

A robot undergoing some motion in an unknown environment may be subject to abrupt changes in acceleration, particularly in machines that experience unknown contacts with the environment such as walking robots. It is also noted that within the sensor system both the acceleration and velocity terms are directly observable. As such a constant jerk model is adopted and it is assumed that both the angular and linear jerk terms are constant in between time steps k and any variation is accounted for through the addition of process noise via the UKF.

The vector $\boldsymbol{x}_{\text{imu}}$ that contains the IMU states to be estimated is given as

$$\boldsymbol{x}_{\text{imu}} = \begin{bmatrix} \boldsymbol{a}_x & \boldsymbol{a}_y & \boldsymbol{a}_z & \boldsymbol{\omega}_x & \boldsymbol{\omega}_y & \boldsymbol{\omega}_z \end{bmatrix}^{\mathsf{T}}. \tag{4.1}$$

Writing $s = x, y, z$, the linear acceleration components and the angular acceleration and velocity components contained in (4.1) are then given as

$$\begin{aligned} \boldsymbol{a}_s &= \begin{bmatrix} \dot{a}_s & a_s \end{bmatrix}, \\ \boldsymbol{\omega}_s &= \begin{bmatrix} \ddot{\omega}_s & \dot{\omega}_s & \omega_s \end{bmatrix}. \end{aligned} \tag{4.2}$$

At each time step k, for a sample time Δt the state is updated by the UKF via a state model of the form $\boldsymbol{x}_{\text{imu},k} = f_{\text{imu}}(\boldsymbol{x}_{\text{imu},k-1}, \boldsymbol{v}_{\text{imu},k-1})$. The transition function $f_{\text{imu}}(\cdot)$ is constructed from the linear and angular components of the state vector and integrated via simple Euler integration as

$$\begin{aligned} \boldsymbol{a}_{x,y,z,k} &= \begin{bmatrix} \dot{a} \\ a + \dot{a}\Delta t \end{bmatrix}_{k-1} \\ \boldsymbol{\omega}_{x,y,z,k} &= \begin{bmatrix} \ddot{\omega} \\ \dot{\omega} + \ddot{\omega}\Delta t \\ \omega + \dot{\omega}\Delta t + \frac{1}{2}\ddot{\omega}\Delta t^2 \end{bmatrix}_{k-1}. \end{aligned} \tag{4.3}$$

In this model the $\boldsymbol{v}_{\text{imu}}$ term is a random variable that accounts for any uncertainty in the linear and angular components, particularly the jerk and angular velocity components which have no sensor directly associated with them. By incorporating this term the covariances of the of the noise source can be simply added. As such $\boldsymbol{v}_{\text{imu}}$ can be seen as a tuning parameter for the UKF.

During the UKF update the state prediction (4.3) is corrected by an observation of the sensors at each time step k. The observation model $\boldsymbol{y}_{\text{imu},k} = h_{\text{imu}}(\boldsymbol{x}_{\text{imu},k}, \boldsymbol{w}_{\text{imu},k})$ transforms the predicted states into predicted measurements so that they may be compared with actual sensor readings.

The observation model for the IMU component is constructed from (3.11), with $\boldsymbol{x}$ being constructed from $\boldsymbol{x}_{\text{imu},k}$ as

$$\boldsymbol{y}_{\text{imu},k} = \boldsymbol{B}h_{\text{ix}}(\boldsymbol{x}_{\text{imu},k}) + \boldsymbol{w}_{\text{imu},k}, \tag{4.4}$$

where $\boldsymbol{B}$ includes the calibrated position estimates as given in (5.17) and $h_{\text{ix}}(\cdot)$ being a non-linear operation that transforms the estimated state into the vector $\boldsymbol{x}$. The observation noise vector $\boldsymbol{w}_{\text{imu}}$ accounts for sensor noise and is derived from the hardware data sheets.

4.4.2 Relative UKF

The relative component UKF formulation follows the IMU component UKF and adopts a constant jerk model. In this case the relative state vector

$$\boldsymbol{x}_{\text{rel}} = \begin{bmatrix} \dddot{\theta} & \ddot{\theta} & \dot{\theta} & \theta \end{bmatrix}^{\mathsf{T}} \tag{4.5}$$

is comprised of the relative link angular jerk $\dddot{\theta}$, acceleration $\ddot{\theta}$, velocity $\dot{\theta}$ and relative link position θ.

The state propagation model for the relative component is given as

$$\boldsymbol{x}_{\text{rel},k} = \begin{bmatrix} \dddot{\theta} \\ \ddot{\theta} + \dddot{\theta}\Delta t \\ \dot{\theta} + \ddot{\theta}\Delta t + \frac{1}{2}\dddot{\theta}\Delta t^2 \\ \theta + \dot{\theta}\Delta t + \frac{1}{2}\ddot{\theta}\Delta t^2 + \frac{1}{6}\dddot{\theta}\Delta t^3 \end{bmatrix}_{\text{rel},k-1} + \boldsymbol{v}_{\text{rel},k-1}, \tag{4.6}$$

again, where Δt is the sample time and $\boldsymbol{v}_{\text{rel}}$ is the process noise that accounts for any uncertainty in the process model and serves as a tuning parameter for the relative UKF component.

As with the IMU component the relative state prediction $\boldsymbol{x}_{\text{rel},k}$ is corrected by an observation of the sensors via the observation model $\boldsymbol{y}_{\text{rel},k} = h_{\text{rel}}(\boldsymbol{x}_{\text{rel},k}, \boldsymbol{w}_{\text{rel},k})$. In this model the predicted state is compared against both the relative accelerometer and the incremental encoder. The accelerometer observation is constructed in a similar manner to the IMU observation, however in this case only one accelerometer is compared against. The observation model is

$$\boldsymbol{y}_{\text{rel},k} = \begin{bmatrix} {}^{i-1}\boldsymbol{a}_k & \theta_{\text{rel}} \end{bmatrix}_k^{\mathsf{T}} + \boldsymbol{w}_{\text{rel},k}, \tag{4.7}$$

with θ_{rel} being the relative angular position to be compared to an incremental encoder measurement and ${}^{i-1}\boldsymbol{a}_k$ being the accelerometer estimate taken from (3.12). In this case we recall that the relative accelerometer estimates are derived from both the IMU estimated state and the relative estimated state. Substituting (3.13) and (3.21) into (3.12) and letting ${}^{i-1}_{i}\boldsymbol{R} = \boldsymbol{R}_z(\theta_{\text{rel}})$ gives the relative accelerometer observation equation,

$${}^{i-1}\boldsymbol{a}_k = \boldsymbol{R}_z(\theta_{\text{rel}})\boldsymbol{a}_{\text{imu}} + \dot{\boldsymbol{\omega}}_{\text{rel}} \times {}^{i-1}\boldsymbol{r}_k + \boldsymbol{\omega}_{\text{rel}} \times (\boldsymbol{\omega}_{\text{rel}} \times {}^{i-1}\boldsymbol{r}_k). \tag{4.8}$$

In our specific case the rotation about the $\hat{\boldsymbol{z}}$ axis has no effect on the angular velocity and acceleration and these terms simplify to

$$\begin{aligned} \dot{\boldsymbol{\omega}}_{\text{rel}} &= \dot{\boldsymbol{\omega}}_{\text{imu}} - \ddot{\theta}_{\text{rel}}\hat{\boldsymbol{z}}, \\ \boldsymbol{\omega}_{\text{rel}} &= \boldsymbol{\omega}_{\text{imu}} - \dot{\theta}_{\text{rel}}\hat{\boldsymbol{z}}. \end{aligned} \tag{4.9}$$

4.5 Building Process Noise Matrices

Given that the joint sensor system executes on a digital computer discrete state propagation models have been used for both the AO-IMU and relative estimators. In doing this discretisation of the process noise matrices $\boldsymbol{Q}$ is required.

A linear system can be described by the model

$$f(x) = \boldsymbol{F}\boldsymbol{x} + \boldsymbol{\Gamma}\boldsymbol{v} \tag{4.10}$$

where $\boldsymbol{\Gamma}$ is the noise gain of the system and $\boldsymbol{v}$ is some white noise process that represents the highest order term. Although this model represents a linear system, it sufficiently describes the models used in the prediction steps in all three UKF components and in these cases $\boldsymbol{v}$ represents the 'motion' of the jerk term between time steps. Within this it is assumed that the system jerk is constant for each time step, but may vary between successive time steps. A process noise matrix $\boldsymbol{Q}$ can then be obtained from an equation of the form

$$\boldsymbol{Q} = \boldsymbol{\Gamma}\sigma^2\boldsymbol{\Gamma}^\mathsf{T}, \tag{4.11}$$

where the variance σ^2 can be seen as a tuning parameter for the system.

As discussed in Section 4.4.1 the AO-IMU state update model is separated into linear and rotational components. Consequently, obtaining the process noise matrices are also split into linear and rotational components. The linear AO-IMU component is described by a first order process where the noise term $\boldsymbol{\Gamma}$ and is written as

$$\boldsymbol{\Gamma} = \begin{bmatrix} 1 & \Delta t \end{bmatrix}^\mathsf{T}. \tag{4.12}$$

The matrix $\boldsymbol{Q}_{\text{imu,lin},n}$ for each axis n is then obtained from the equation

$$\begin{aligned} \boldsymbol{Q}_{\text{imu,lin},n} &= \boldsymbol{\Gamma}\sigma^2_{imu,lin}\boldsymbol{\Gamma}^\mathsf{T} \\ &= \begin{bmatrix} 1 & \Delta t \\ \Delta t & \Delta t^2 \end{bmatrix} \sigma^2_{\text{imu,lin}}. \end{aligned} \tag{4.13}$$

The rotational components requiring estimation of jerk, acceleration and velocity are based on a second order process. In a similar manner the noise term $\boldsymbol{\Gamma}$ is given as

$$\boldsymbol{\Gamma} = \begin{bmatrix} 1 & \Delta t & \frac{1}{2}\Delta t^2 \end{bmatrix}^\mathsf{T}, \tag{4.14}$$

and again the matrix $\boldsymbol{Q}_{\text{imu,rot},n}$ for each axis n is obtained from

$$\begin{aligned} \boldsymbol{Q}_{\text{imu,rot},n} &= \boldsymbol{\Gamma}\sigma^2_{imu,rot}\boldsymbol{\Gamma}^\mathsf{T} \\ &= \begin{bmatrix} 1 & \Delta t & \frac{1}{2}\Delta t^2 \\ \Delta t & \Delta t^2 & \frac{1}{2}\Delta t^3 \\ \frac{1}{2}\Delta t^2 & \frac{1}{2}\Delta t^3 & \frac{1}{4}\Delta t^4 \end{bmatrix} \sigma^2_{\text{imu,rot}}. \end{aligned} \tag{4.15}$$

The final AO-IMU process noise matrix is then assembled as

$$\boldsymbol{Q}_{\text{imu}} = \begin{bmatrix} \boldsymbol{Q}_{\text{imu,lin},x} & 0 & 0 & 0 & 0 & 0 \\ 0 & \boldsymbol{Q}_{\text{imu,lin},y} & 0 & 0 & 0 & 0 \\ 0 & 0 & \boldsymbol{Q}_{\text{imu,lin},z} & 0 & 0 & 0 \\ 0 & 0 & 0 & \boldsymbol{Q}_{\text{imu,rot},x} & 0 & 0 \\ 0 & 0 & 0 & 0 & \boldsymbol{Q}_{\text{imu,rot},y} & 0 \\ 0 & 0 & 0 & 0 & 0 & \boldsymbol{Q}_{\text{imu,rot},z} \end{bmatrix}, \tag{4.16}$$

noting that the zeros in the off-axis terms show that it is assumed that the noise between the axes is independent.

Unlike the AO-IMU component the relative UKF component only estimates quantities about the local $\hat{z}$ axis. These rotational components are based on a third order process where jerk, acceleration, velocity and position are all estimated. In this case the noise term $\mathbf{\Gamma}$ is given as

$$\mathbf{\Gamma} = \begin{bmatrix} 1 & \Delta t & \frac{1}{2}\Delta t^2 & \frac{1}{6}\Delta t^3 \end{bmatrix}^{\mathsf{T}}, \tag{4.17}$$

and finally the relative component process noise matrix is constructed as

$$\begin{aligned} \boldsymbol{Q}_{\text{rel}} &= \mathbf{\Gamma}\sigma^2_{\text{rel,rot}}\mathbf{\Gamma}^{\mathsf{T}} \\ &= \begin{bmatrix} 1 & \Delta t & \frac{1}{2}\Delta t^2 & \frac{1}{6}\Delta t^3 \\ \Delta t & \Delta t^2 & \frac{1}{2}\Delta t^3 & \frac{1}{6}\Delta t^4 \\ \frac{1}{2}\Delta t^2 & \frac{1}{2}\Delta t^3 & \frac{1}{4}\Delta t^4 & \frac{1}{12}\Delta t^5 \\ \frac{1}{6}\Delta t^3 & \frac{1}{6}\Delta t^4 & \frac{1}{12}\Delta t^5 & \frac{1}{36}\Delta t^6 \end{bmatrix} \sigma^2_{\text{rel,rot}}. \end{aligned} \tag{4.18}$$

The values for the noise parameters σ for each of the UKF components, along with the time step Δt are detailed in Table 5.3.

Chapter 5

System Hardware and Experimental Results

5.1 Introduction

This chapter details the experimental methods and results employed in this study. Within this the test apparatus employed to assess the performance of the sensor system is first examined. The test apparatus is a simple two degree of freedom pendulum that when fixed to the lower joint, enables testing of the sensor system as it moves through space.

Section 5.4 goes on to detail the calibration procedure required to reduce the effects of the non-ideal off-axis and bias effects inherent to MEMs accelerometers. This section also details a calibration technique used to compensate for any misplacement or misalignment that will occur when physically attaching the sensors to the body frame.

In Section 5.5 the performance of the system is examined under two motion profiles. As the sensor system relies only on measurements from sensors and does not rely on information from the robot's state or model, a chaotic motion profile is first used to investigate the performance of the system when experiencing unknown motions. This is followed by a low velocity profile which is employed to examine the performance impacts of the AO-IMU design choices and when the inertial sensors are nearing their noise floor.

The experimental system output from these motion profiles is compared against online and offline methods. The system output is then compared to three online methods that are each subject to the same motion profiles. The online methods serve to enable comparing the sensor performance to modern joint state estimation methods. The sensor system outputs and the online methods are then compared to two offline joint state estimation methods, with a forward/backward zero phase delay Kalman filter based system serving as a baseline for all system performances to be compared against.

Within this chapter the test rig hardware and construction is first detailed. The experimental considerations for the sensing elements are then discussed, followed by the details of the data capture system. The UKF experimental parameters are then detailed.

The online and offline systems used to compare the system performance are then detailed in Section 5.3, then the system calibration procedure is outlined. This is then followed by a discussion on the system results and an examination of the effects of calibration and system misalignment.

5.2 Test Rig

5.2.1 Pendulum Geometry and Hardware

Testing for the joint sensor system was carried out on the two degree of freedom pendulum shown in Figure 5.6. A schematic for the test rig is given in Figure 5.1. The rig is an unactuated two degree of freedom pendulum with both moving axes constrained to rotate only about the local $\hat{z}$ axis. The hardware test rig allows testing of the standard joint sensor system as the joint of interest moves through space. The design of the rig also allows further exploration of augmented sensor systems such as multiple joint sensors. These systems explored are covered in Chapter 6.

The rig construction is based around parts cut on a waterjet from flat aluminium plate, which were then built into a three dimensional structure. This method allows retaining desirable physical properties of the aluminium, such as rigidity and dimensional stability while keeping the costs and manufacture time low. Each link can then be considered to be a rigid body for the purpose of the experiment. The inertial sensors themselves, along with the electrical components of the incremental encoders require mounting to the test rig. Suitable mounts were 3D printed from PLA plastic and serve to electrically isolate the printed circuit boards (PCBs). The PCBs were glued to the plastic mounts, which were then in turn glued to the rig frame.

The physical placement of both the inertial sensors and the incremental encoders are subject to some constraints. The review of the literature and in particular in the work by Lu and Lin (2011) shows that the inertial sensors placed at opposing corners of a cuboid structure centred about the origin o offers the best performance. It was also shown by Madgwick et al. (2013) that the separation of the sensors directly affects the system performance and thus the volume of the cuboid structure formed by the placement of the accelerometers should be maximised. A cuboid structure of maximised volume on a slender robotic link is not practically achievable and may lead to decreased performance. An alternative structure is proposed: referring to Figure 5.1 the accelerometers are placed in a cuboid like manner with the centre being offset at point o. If it were to be that a strict cuboid formation be employed then the forward accelerometers at x_p would be placed much closer to the origin, resulting in a violation of the sensor separation guidelines and a reduction in AO-IMU performance would be seen. As such we take advantage of the pendulum link length and place the accelerometers much farther up the link, and in a sense trade off performance by mitigating the non-ideal cuboid structure by increasing the forward accelerometer separation.

As depicted in Figure 5.1 four accelerometer units are placed on both the upper (l_{i-1}) and lower (l_i) links. Four accelerometers are placed on the upper link, however only the sensor placed at ${}^k\boldsymbol{r}_2$ is employed as a relative sensor in the standard system. The extended works in Chapter 6 make use of all the upper link accelerometers.

Finally the incremental encoder installation is considered. For this the manufacturer outlines a requirement for the sensing read head to be placed between 0.3–0.6mm above the rotating magnetic ring. This was achieved by mounting the sensor element on the PCB at a fixed height and adjusting the magnetic ring carrier until the sensor reported adequate readings.

Table 5.1: Test rig physical parameters.

Upper link length	L_{ul}	200 mm
Lower link length	L_{ll}	200 mm
Positive x axis accelerometer	x_p	100 mm
Negative x axis accelerometer	x_n	−15 mm
Positive y axis accelerometer	y_n	26 mm
Negative z axis accelerometer	y_p	−26 mm
Positive upper link z axis accelerometer	$z_{p,ul}$	21 mm
Negative upper link z axis accelerometer	$z_{n,ul}$	−21 mm
Positive lower link z axis accelerometer	$z_{p,ll}$	26.6 mm
Negative lower link z axis accelerometer	$z_{n,ll}$	−26.6 mm

Table 5.2: Accelerometer position vectors built from test rig physical parameters.

l_i	l_{i-1}
${}^{i}\boldsymbol{r}_1 = \begin{bmatrix} x_n & y_n & z_{p,ll} \end{bmatrix}$	${}^{i-1}\boldsymbol{r}_1 = \begin{bmatrix} x_n & y_n & z_{p,ul} \end{bmatrix}$
${}^{i}\boldsymbol{r}_2 = \begin{bmatrix} x_p & y_n & z_{n,ll} \end{bmatrix}$	${}^{i-1}\boldsymbol{r}_2 = \begin{bmatrix} x_p & y_n & z_{n,ul} \end{bmatrix}$
${}^{i}\boldsymbol{r}_3 = \begin{bmatrix} x_p & y_p & z_{p,ll} \end{bmatrix}$	${}^{i-1}\boldsymbol{r}_3 = \begin{bmatrix} x_p & y_p & z_{p,ul} \end{bmatrix}$
${}^{i}\boldsymbol{r}_4 = \begin{bmatrix} x_n & y_p & z_{n,ll} \end{bmatrix}$	${}^{i-1}\boldsymbol{r}_4 = \begin{bmatrix} x_n & y_p & z_{n,ul} \end{bmatrix}$

Table 5.3: Accelerometer and gyroscope sensor parameters, selected measurement ranges and UKF parameters.

Accelerometer measurement range	$\pm$ 4	G
Accelerometer max output rate	1.6	kHz
Accelerometer LPF cutoff	400	Hz
Accelerometer noise density @ measurement range	90	$\mu g/\sqrt{\text{Hz}}$
Gyroscope measurement range	$\pm$ 1000 (17.45)	°/s (rad s^{-1})
Gyroscope max output rate	1.6	kHz
Gyroscope LPF cutoff	400	Hz
Gyroscope noise density @ measurement range	7	$m°/s/\sqrt{\text{Hz}}$
Encoder Resolution	16	bits
System sample rate (Δt)	1	kHz
$\sigma_{\text{imu,lin}}$	3	m s^{-3}
$\sigma_{\text{imu,rot}}$	20	rad s^{-3}
$\sigma_{\text{rel,rot}}$	200	rad s^{-3}
$R_{\text{imu,acc}}$	0.0111	m s^{-2}
$R_{\text{rel,enc}}$	2.1343×10^{-9}	rad
α	1×10^{-3}	-
κ	0	-
β	2	-

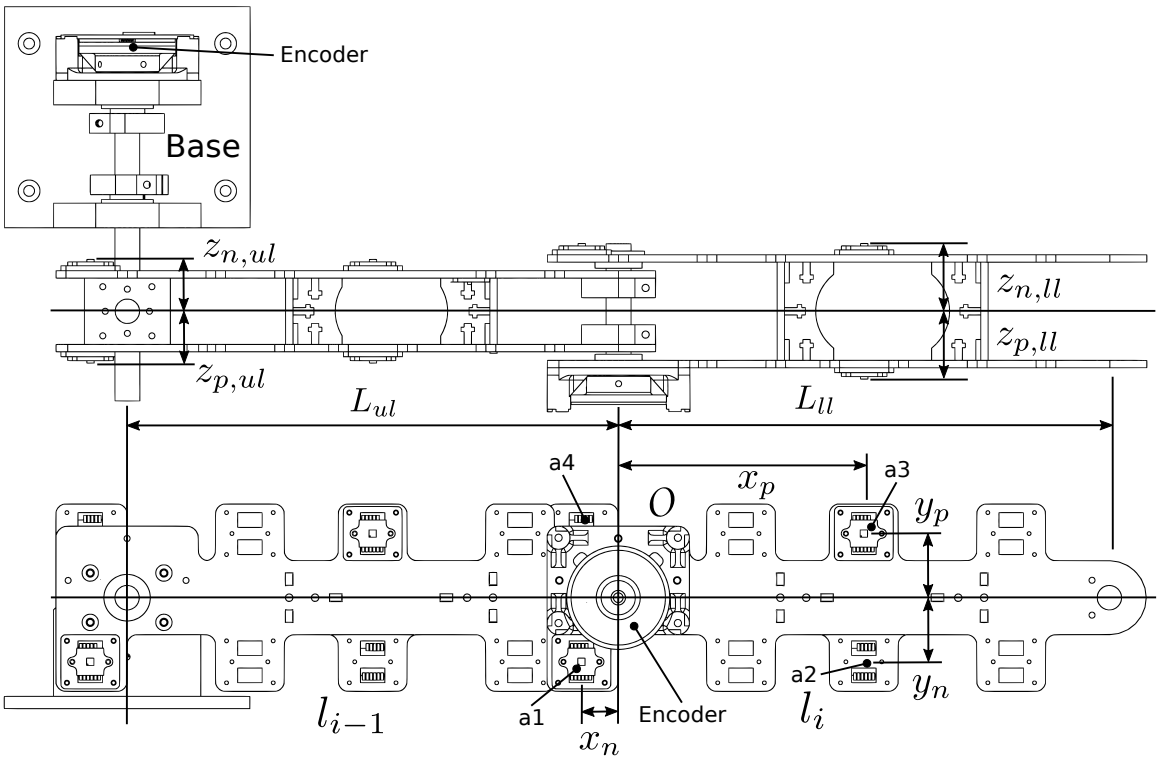

Figure 5.1: Test apparatus schematic

5.2.2 Sensing Devices

5.2.2.1 Inertial Sensors

The formulation of the AO-IMU selected relies on four three-axis accelerometer units and the relative joint component employs a single three-axis accelerometers. The ST Micro *LSM6DS3* (*LSM6DS3 iNEMO Inertial Module* 2016)[1] three-axis accelerometer and gyroscope IC was chosen for this task. The device includes a three-axis gyroscope for negligible extra cost over that of a similar accelerometer only device. The *LSM6DS3* provides a digital output of the linear acceleration and angular rate and offers many online configuration options. Of this, the linear acceleration and angular rate measurement range settings are used to set sensor ranges to give the largest signal to noise over a chosen operating range.

The ranges are chosen as a function of the vector ${}^i\boldsymbol{r}_j$ of the accelerometer furthest from the origin o and a reasonable expected maximum angular acceleration. Referring to Tables 5.1 and 5.2, the accelerometers at ${}^i\boldsymbol{r}_2$ and ${}^i\boldsymbol{r}_3$ are both much farther away from the origin than the others. From here the linear acceleration measurement range of $\pm 4G$ is selected. This gives approximately

$$\begin{aligned} \alpha &= \frac{a}{r} \\ 392\text{rad}\,\text{s}^{-2} &= \frac{(4G \times 9.81\text{m}\,\text{s}^{-2})}{0.1\text{m}}, \end{aligned} \tag{5.1}$$

which is a reasonable experimental range, noting that the measurable linear acceleration of point o on the joint will also saturate at $\pm 4G$ ($\approx \pm 40\text{m}\,\text{s}^{-2}$). Similarly, an angular velocity range for the gyroscopes was chosen and the gains selected to match. Table 5.3 shows the ranges selected and the noise properties of the sensor.

[1] An earlier version of the test rig used *LIS3DSH*(*LIS3DSH* 2011) accelerometers. All test data is based on the *LSM6DS3* devices, however the calibration effects of the two devices are examined later in 5.5.1

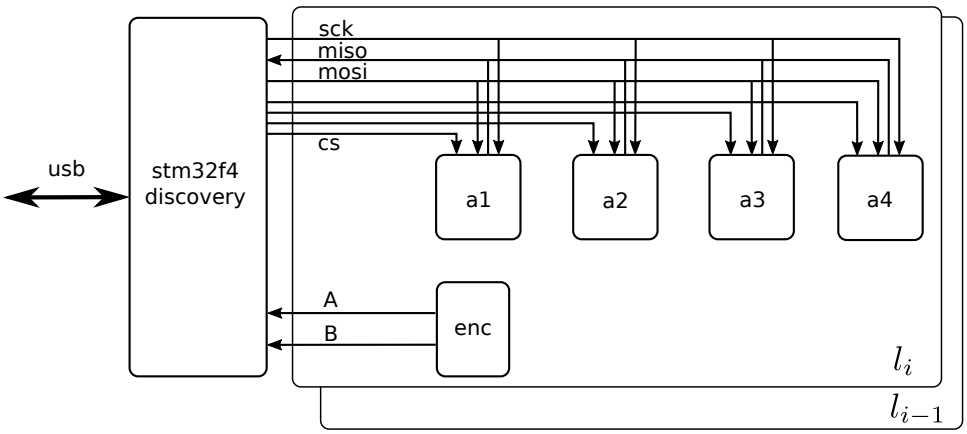

Figure 5.2: Schematic of data capture setup.

5.2.2.2 Incremental Encoders

An incremental encoder selected to measure the relative angle between the two links. A simple custom rotary encoder based on the Austria Microsystems *AS*5311 (*AS5311 High Resolution Magnetic Encoder* 2009) linear magnetic encoder was designed and assembled. This contactless device measures the position of a multi-pole magnetic ring and provides quadrature outputs at an equivalent resolution of 16 bits over a single rotation. The raw output of the encoder appears in the data capture system as 'ticks' and requires scaling. The scale parameter in (3.5) is given as $S_e = \frac{2\pi}{2^{16}}$.

5.2.2.3 Data Capture

In total the data capture system for the joint sensor must support eight accelerometers and two incremental encoders. Each accelerometer transmits and receives data over a serial peripheral interface (SPI) bus and the encoders simply output their position via a quadrature based signal. The system is to retrieve three axes of acceleration and angular rate data from the eight accelerometers, along with the positions from the encoder at a rate of 1kHz. The task of capturing the real-time sensor data was performed via an ST Micro *STM*32*F*4 Discovery board and a simple daughter board that broke out connections to the sensors. Figure 5.2 shows the schematic of the data capture system. Within this an Arm based 32bit microprocessor handled all communications between the sensors and host computer. Software was developed based on the embedded real-time operating system ChibiOS (*ChibiOS/RT Home page* 2016) that interfaced via the microprocessor's dedicated peripheral to the external sensors. The software simply requested acceleration and angular rate data from each of the inertial sensors and sampled the encoder positions. This raw data would then be transmitted via USB to the host computer for further processing.

5.2.2.4 UKF Parameters

The noise density properties of the accelerometers and encoder as taken from the device data sheets are used to build the UKF measurement noise matrix $\boldsymbol{R}$ for both estimators. In obtaining the process noise matrix $\boldsymbol{Q}$ a discrete noise process is assumed, which in turn allows the selection of a variance parameter σ for each process. The noise between the $\hat{\boldsymbol{x}}$, $\hat{\boldsymbol{y}}$ and $\hat{\boldsymbol{z}}$ axes is also assumed independent. This allows for the selection of individual axis variance if required. The variance terms for the IMU state components described in Section 4.4.1 are given by the terms $\sigma_{\text{imu,lin}}$ and $\sigma_{\text{imu,rot}}$, which describe the linear and rotational noise properties respectively. Likewise, the term $\sigma_{\text{rel,rot}}$ describes the noise properties of the relative

Table 5.4: Baseline F/B Kalman and 'derivative and filter' parameters

$\sigma_{\text{fb,kal}}$	0.82	$\text{rad}\,\text{s}^{-3}$
$R_{\text{kf,enc}}$	2.1343×10^{-9}	rad
$f_{c,\text{fb}}$	25	Hz

state in (4.5). A programmed iterative approach to obtaining the best performing σ values was adopted. In this, σ values that fitted the expected approximate jerk term were used to seed an iterative method that searched a range around the initial value. This would then find the σ that resulted in the best performance in an RMS sense. Finally, the measurement noise for the accelerometers and encoder is given by $R_{\text{imu,acc}}$ and $R_{\text{rel,enc}}$ respectively. Table 5.3 shows the final values used in the experimental system, along with the UKF parameters α, κ and β which have been selected for a normal distribution.

5.3 Performance Comparison and Baselines

5.3.1 Baseline Comparison

To evaluate the system performance the joint sensor is compared to both online and offline methods. The offline Kalman and low pass filter methods presented here serve as baseline measurements in which the performance of all the systems presented within this work can be compared to. Since it was not practical to obtain direct measurements of both joint's angular acceleration and velocity that were of higher precision than that obtained within this work, methods based on zero delay (forward/backward) Kalman filtering and 'differentiation and filtering' of the joint's position were put to use.

5.3.1.1 Zero Delay Kalman Filter

A standard Kalman filter modified to incorporate zero delay functionality from the EKF/UKF Toolbox for Matlab (Hartikainen et al. 2011) was configured with a constant jerk state transition model, similar to that given in (4.5). For the state at time step k

$$\begin{bmatrix} \dddot{\theta} & \ddot{\theta} & \dot{\theta} & \theta \end{bmatrix}_k^{\mathsf{T}} \tag{5.2}$$

the measurement matrix $\boldsymbol{H}$ can be given as

$$\boldsymbol{H} = \begin{bmatrix} 0 & 0 & 0 & 1 \end{bmatrix}. \tag{5.3}$$

Within this the measurement noise $R_{\text{kf,enc}}$ is given in Table 5.4, and in a similar manner to the formulation in Section 5.2.2.4 the process noise is described by a single variance parameter σ_{fbkal}, also given in Table 5.4.

5.3.1.2 Zero Delay 'Derivative and Filter'

A forward/backward (zero delay) low pass filter and derivative method is also employed as a baseline to compare the system performance against. The states for this estimate are obtained by taking successive derivatives of each state, starting with position and filtering them via the Matlab $filtfilt$ command with a -6dB filter cutoff set at $f_{c,\text{fb}}$ (Table 5.4). The filter is based on a simple first order moving average structure. The gains $\sigma_{\text{fb,kal}}$ and $f_{c,\text{fb}}$ for the two baselines were derived through matching the state of a simulation of the sensor system to that of the real system. This simulation was in turn based on fixing the upper

Table 5.5: Online Kalman, 'derivative and filter' and encoder and gyro system parameters

$\sigma_{\text{kf,online}}$	0.82	$\text{rad}\,\text{s}^{-3}$
$R_{\text{kf,enc}}$	6.9787×10^{-5}	rad
$f_{c,\text{fb}}$	25	Hz
$\sigma_{\text{ukf,online}}$	0.82	$\text{rad}\,\text{s}^{-3}$
$R_{\text{ukf,enc}}$	2.1343×10^{-9}	rad
$R_{\text{ukf,gyro}}$	6.9787×10^{-5}	$\text{rad}\,\text{s}^{-1}$

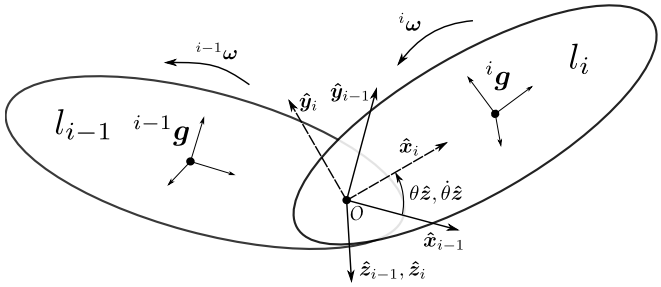

Figure 5.3: Gyro and Encoder only kinematics.

link such that the lower link became a single link pendulum, then lifting the lower link to an angle of $\theta = \pi/2$ and letting it drop. The acceleration and velocity were extracted from the simulation and the filter gains were adjusted until the simple pendulum state closely matched that of the simulation.

5.3.2 Online Comparison

The sensor is also compared to three online methods that are frequently used in robotic systems. Similarly to the baseline methods, the online methods are based on a standard Kalman filter and a 'derivative and filter' method. An extra online method based on fusing the position encoder with a MEMs gyro is also included in the system performance comparison. The plain Kalman filter and 'derivative and filter' method will not be detailed as they are configured in the same manner as the baseline comparison, except they omit the forward/backward component. The gains for the online Kalman filter ($\sigma_{\text{kf,online}}$ and $R_{\text{kf,enc}}$) and the gains for the 'derivative and filter' ($f_{c,\text{fb}}$) are given in Table 5.5.

5.3.2.1 Online Gyro and Encoder System

The gyroscope and encoder system is based on a constant jerk UKF formulation. Being a linear system the gyro and encoder formulation could have used a standard Kalman filter, however the choice of a UKF in this particular case was that of convenience. During the measurement update section of the UKF the estimated state is compared to both an encoder and the difference between two gyroscopes placed on each link. The gyro component of the measurement function is based on summation of angular velocities as given in (3.14). This is then written as

$$^{i}\boldsymbol{\omega}_{i-1,i} = {}^{i}\boldsymbol{\omega} - {}^{i}\boldsymbol{\omega}_{i-1}. \tag{5.4}$$

The angular velocities are expressed in the frame in which they are obtained as

$$^{i}\boldsymbol{\omega}_{i-1,i} = {}^{i}\boldsymbol{\omega} - {}^{i}_{i-1}\boldsymbol{R}({}^{i-1}\boldsymbol{\omega}_{i-1}), \tag{5.5}$$

and in this case, the rotation is about the $\hat{z}$ axis and has no effect. The relative angular velocity is then simply given as

$$ {}^{i}\boldsymbol{\omega}_{i-1,i} = {}^{i}\boldsymbol{\omega} - {}^{i-1}\boldsymbol{\omega}. \tag{5.6} $$

Equation (5.6), whose values are obtained from the gyroscopes and the position measurement from the encoder are then directly compared to during the measurement update via the function

$$ \begin{bmatrix} ({}^{i}\boldsymbol{\omega} - {}^{i-1}\boldsymbol{\omega})\hat{\boldsymbol{z}} \\ {}^{i}\theta_{\text{enc}} \end{bmatrix}_k = \begin{bmatrix} \dot{\theta}_{\text{rel}} \\ \theta_{\text{rel}} \end{bmatrix}_k + \boldsymbol{w}_{\text{rel},k}. \tag{5.7} $$

The state transition variance parameter ($\sigma_{\text{ukf,online}}$) and the measurement noise parameters ($R_{\text{ukf,enc}}$ and $R_{\text{ukf,gyro}}$) are given in Table 5.5.

5.4 Accelerometer Calibration

The two significant sources of error that affect the performance of the joint sensor system can be compensated for by offline calibration procedures. The first source of error originates directly from the sensors themselves in the form of manufacturing error, temperature dependent errors and bias errors. Manufacturing errors result in the sensor axes being not orthogonal upon which coupling of the axes becomes apparent at the output. The sensors themselves will also experience some level of non-linearity in their output, however in the devices selected this effect is negligible and not considered in this work. Sensor bias errors appear as some non-zero signal being presented at the sensor output when the device is stationary. In the case of the accelerometer it is expected that the device will measure acceleration due to gravity when stationary, however bias terms will still affect the device output if not accounted for. Temperature dependent effects are not considered in this work, as short experimental times are employed. If considered these effects would appear as a temperature dependent bias and scaling of the sensor output. Interestingly, although the sensors chosen are low cost they are relatively robust to temperature dependent effects with the *LSM6DS3* device experiencing a change from zero of 0.5mg/°C.

The second source of error originates from the placement and orientation of the accelerometer during construction of the sensor system. Ideally the sensors will be placed with their sensitive axes aligned exactly with the body frame axes. In reality placing the devices in such an exacting manner is not possible and some level of performance degradation is to be expected if this misplacement is not accounted for.

In both cases the errors presented can be compensated for once the accelerometers are mounted for the physical hardware. In this section methods for correcting for both the sensor level errors and the positioning errors are detailed. Both methods presented are relatively straight forward in execution and do not require any special hardware other than the test rig as used throughout the system experiments.

5.4.1 Bias and Cross Axis Calibration

In this section the errors inherent to MEMs accelerometers are accounted for. Within this the sensor gain, bias and cross axis effects can easily be compensated for by exploiting the fact that when an accelerometer sits stationary it will measure acceleration due to gravity. This is a well studied technique (Frosio et al. 2009; Glueck et al. 2014; Panahandeh et al. 2010) and involves physically placing and resting the sensor system in a number of different orientations. Due to this simple method and positive results reported this method was incorporated into the sensor system as the first calibration method.

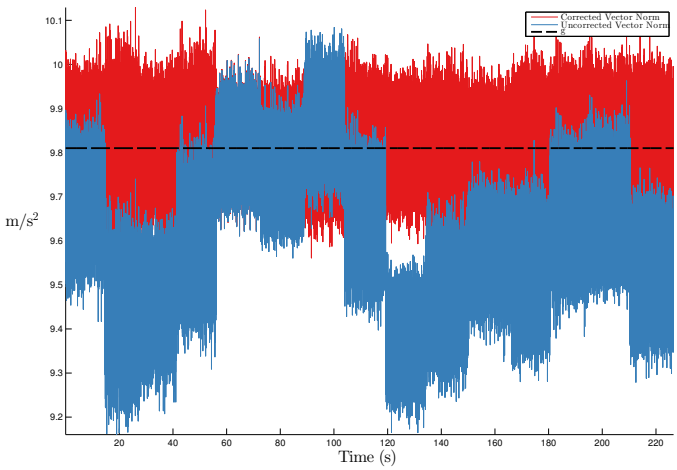

Figure 5.4: Comparison of calibrated and uncalibrated accelerometer vector norms as a result of the gravity based calibration method.

During this procedure the entire rig was removed from the upper base and fixed at the lower joint such that it became a single rigid body. As the rig was placed and rested on each side and edge, the sensor output was recorded and the data captured over the different orientations was employed in finding the unknown parameters of the sensor model in which the solution is known.

When stationary the measured magnitude of a calibrated accelerometer's output is constant and equal to the acceleration due to gravity in all directions, such that

$$\sqrt{a_x^2 + a_y^2 + a_z^2} = g. \tag{5.8}$$

Thus for a stationary uncalibrated accelerometer measurement $\boldsymbol{u}$, (3.1) can be simplified to

$$g = ||\boldsymbol{S}\boldsymbol{u} + \boldsymbol{b}||, \tag{5.9}$$

where g is the magnitude of the gravity vector $\boldsymbol{g} = \begin{bmatrix} 0 & 0 & -9.81 \end{bmatrix}^\mathsf{T}$, $\boldsymbol{S}$ is the matrix of gain parameters

$$\boldsymbol{S} = \begin{bmatrix} S_{xx} & S_{xy} & S_{xz} \\ S_{yx} & S_{yy} & S_{yz} \\ S_{zx} & S_{zy} & S_{zz} \end{bmatrix}, \tag{5.10}$$

and the vector $\boldsymbol{b}$ contains the initial bias terms

$$\boldsymbol{b} = \begin{bmatrix} b_x & b_y & b_z \end{bmatrix}^\mathsf{T} \tag{5.11}$$

and $||.||$ is the vector norm operation. The matrix $\boldsymbol{S}$ accounts for any variation in axis gain and coupling between accelerometer axes, where the term S_{mn} describes the proportion of the gain m affecting axis n (Madgwick et al. 2013). Ideally the off-axis coupling terms will equate to zero, however real accelerometers may be affected by up 2% and a calibration procedure that incorporates the off-axis coupling terms will yield a higher accuracy measurement (Frosio et al. 2009).

Imposing a symmetry constraint on $\boldsymbol{S}$ such that $S_{xy} = S_{yx}$, $S_{xz} = S_{zx}$ and $S_{yz} = S_{zy}$ and including the bias terms from $\boldsymbol{b}$ an accelerometer calibration model consisting of nine independent parameters is obtained. The nine parameters for each of the j accelerometers

$$\boldsymbol{e} = \begin{bmatrix} S_{xx} & S_{yy} & S_{zz} & S_{xy} & S_{xz} & S_{yz} & b_x & b_y & b_z \end{bmatrix}^\mathsf{T}, \tag{5.12}$$

Table 5.6: Accelerometer Calibration Components

	Position [mm]			Position Offset δ [mm]			Rotation Offset $\boldsymbol{E}$ [rad]			Gain S_{mm} [-]			Off Axis S_{mn} [m s^{-2}]			Bias b [m s^{-2}]		
Sensor	x	y	z	x	y	z	E_x	E_y	E_z	S_{xx}	S_{yy}	S_{zz}	S_{xy}	S_{xz}	S_{yz}	b_x	b_y	b_z
${}^{i}\boldsymbol{r}_1$	−15.00	−26.00	26.60	−0.42	0.26	0.99	0.00	−0.01	0.02	1.02	1.00	1.03	−0.02	0.00	0.00	0.13	−0.08	0.03
${}^{i}\boldsymbol{r}_2$	100.00	−26.00	−26.60	−1.50	−1.28	3.19	−0.01	0.00	0.02	0.99	0.99	1.00	−0.02	0.00	0.00	−0.07	0.00	0.24
${}^{i}\boldsymbol{r}_3$	100.00	26.00	26.60	−0.38	−0.59	1.98	−0.04	0.00	−0.03	1.01	0.99	1.00	−0.02	0.00	0.00	−0.02	−0.32	0.25
${}^{i}\boldsymbol{r}_4$	−15.00	26.00	−26.60	−1.40	0.23	3.06	0.02	0.01	0.01	0.99	1.03	1.00	−0.01	0.00	0.00	−0.16	−0.05	0.28
${}^{i-1}\boldsymbol{r}_k$	−90.00	0.00	−10.00	0.60	−0.27	0.37	0.02	−0.01	0.02	1.01	1.02	0.97	−0.02	0.00	0.00	−0.097	−0.28	0.05

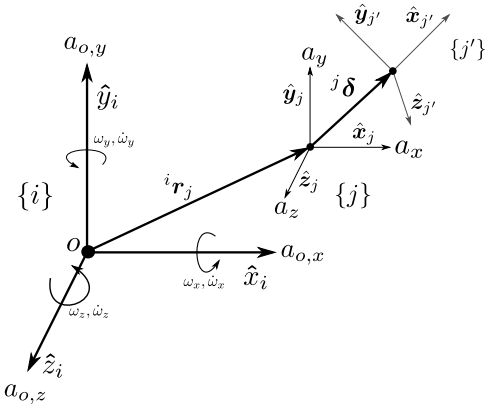

Figure 5.5: Placement of accelerometer j on the rigid body i.

may be found as a solution to the problem

$$\boldsymbol{e}_j = \min_{\boldsymbol{S}_j, \boldsymbol{b}_j} \sum_i (g - ||\boldsymbol{S}_j \boldsymbol{u}_{j,i} + \boldsymbol{b}_j||)^2, \tag{5.13}$$

over i recorded orientations.

During the calibration procedure the test rig was manually rotated and rested on most faces and edges of a cube, for a total of 15 orientations. The rig was rested at each orientation for a period of approximately 15 seconds and during this time a dataset was collected concurrently for each of the accelerometers. Figure 5.4 shows both the calibrated and uncalibrated vector norms of a stationary accelerometer and it can be seen that the calibration procedure successfully corrects the output of the accelerometers. Table 5.6 presents the gain, off-axis and bias parameters obtained for the accelerometers. It is apparent from this data that the bias term is a significant source of error that affects the accelerometer outputs. At a minimum, if this calibration procedure not employed in future work then the accelerometer bias should at least be compensated for.

5.4.2 Accelerometer Alignment

The second source of error affecting the output of the joint sensor system comes about from the physical placement of the sensors onto the actual links. Ideally the accelerometers placed on the test rig will be aligned with that particular link's axes. Due to manufacturing and construction tolerances, in practice this is not easily achieved and the accelerometers will be placed with some rotational and translational misalignment that can lead to significant errors in the estimated states (Madgwick et al. 2013). In this calibration procedure we aim to correct for both rotational misalignment of the accelerometer's sensitive axes from the link's axes and positional misalignment from the sensor's origin from the ideal position.

Consider an accelerometer in Figure 5.5 placed on the link l_i at point ${}^{i}\boldsymbol{r}_j$ that is ideally aligned with the body's coordinate frame. The accelerometer measures the acceleration ${}^{i}\boldsymbol{a}_j$ at that point. In a practical implementation the accelerometer will not be accurately placed at j,

rather it will be placed at j' which is some arbitrary frame aligned to the accelerometer's axes.

5.4.2.1 Orientation

The orientation of j' relative to j can be described by a rotation matrix ${}^{j}_{j'}\boldsymbol{R}$ such that

$$ {}^{i}\boldsymbol{a}_j = {}^{j}_{j'}\boldsymbol{R}\, {}^{j'}\boldsymbol{a}, \tag{5.14} $$

and the position of j' relative to j can be given by the vector ${}^{i}\boldsymbol{\delta}$. For a small angle deviation the rotation matrix ${}^{j}_{j'}\boldsymbol{R}$ can be given by the first order approximation (Nilsson et al. 2014),

$$ {}^{j}_{j'}\boldsymbol{R} = (\boldsymbol{I} + \boldsymbol{E}_{\times})\tilde{\boldsymbol{R}}. \tag{5.15} $$

In this, ${}^{j}\boldsymbol{E} = \begin{bmatrix} E_x & E_y & E_z \end{bmatrix}^{\mathsf{T}}$ is a vector of small rotational alignment errors and $\boldsymbol{E}_{\times}$ is the skew symmetric representation of the alignment error vector ${}^{j}\boldsymbol{E}$ and is given by

$$ \boldsymbol{E}_{\times} = \begin{bmatrix} 0 & -E_z & E_y \\ E_z & 0 & -E_x \\ -E_y & E_x & 0 \end{bmatrix}. \tag{5.16} $$

Finally $\boldsymbol{I}$ is the 3×3 identity matrix and $\tilde{\boldsymbol{R}}$ represents the ideal rotation if the accelerometer were mounted without any alignment error. Typically $\tilde{\boldsymbol{R}}$ might be the identity matrix $\boldsymbol{I}$, however in this work the accelerometers are mounted to the test apparatus in the most convenient manner and so $\tilde{\boldsymbol{R}}$ ideally rotates the accelerometers as mounted to the test apparatus into the sensor body frame. See Appendix A for the mappings that transform the accelerometer measurements from the test rig frame to the ideal model frame.

5.4.2.2 Translation

The alignment procedure must also consider that the accelerometers may be placed with some translational error from the ideal positions ${}^{i}\boldsymbol{r}_j$. To compensate for the misplacement the position vectors ${}^{i}\boldsymbol{r}_j$ in (3.6) are augmented with some error ${}^{j}\boldsymbol{\delta}$ such that

$$ {}^{i}\boldsymbol{r}_j = \begin{bmatrix} r_x + \delta_x & r_y + \delta_y & r_z + \delta_z \end{bmatrix}^{\mathsf{T}}, \tag{5.17} $$

where the vector components δ are to be discovered through calibration.

5.4.2.3 Compensating For Misalignment

For each accelerometer in the system the aim of the alignment procedure is to find a vector $\boldsymbol{e} = \begin{bmatrix} {}^{j}\boldsymbol{E} & {}^{j}\boldsymbol{\delta} \end{bmatrix}^{\mathsf{T}}$ of small angle and position deviations that will correct for any linear and rotary misalignment of the accelerometer.

Recalling from (3.6), the accelerations ${}^{i}\boldsymbol{a}_j$ can be found from the kinematics of a rigid body. Equation (3.6) is reformulated into the matrix Equation (3.8). In this calibration section the matrix of known accelerometer positions $\boldsymbol{B}_j$ is augmented with the unknown translational error terms ${}^{j}\boldsymbol{\delta}$. The vector $\boldsymbol{x}$ containing velocity and acceleration components is replaced with an estimate $\hat{\boldsymbol{x}}$ such that

$$ {}^{i}\boldsymbol{a}_j = \boldsymbol{B}_j\hat{\boldsymbol{x}}. \tag{5.18} $$

The estimate $\hat{\boldsymbol{x}}$ of the state is obtained by manually rotating the test rig back and forward

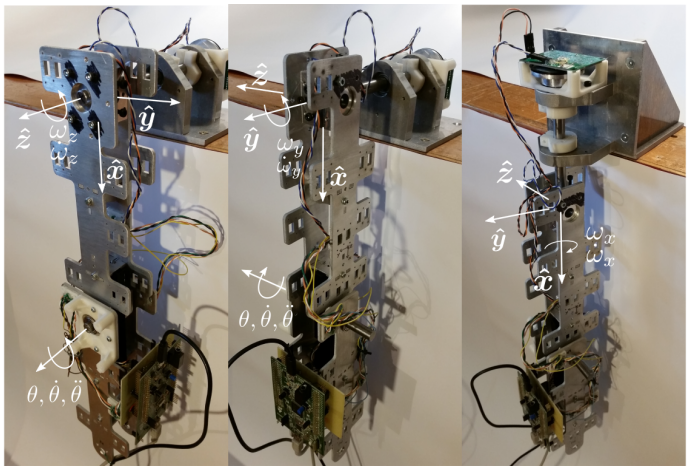

Figure 5.6: Hardware rig in calibration configuration showing rotation about each axis.

about each of the $\hat{x}$, $\hat{y}$ and $\hat{z}$ axes as depicted in Figure 5.6. During this, readings ${}^{j'}\boldsymbol{a}_x$, ${}^{j'}\boldsymbol{a}_y$ and ${}^{j'}\boldsymbol{a}_z$ are taken from the accelerometers, along with the angular positions θ_x, θ_y, and θ_z obtained from an incremental encoder. Since the encoder, shaft and mounting block (Figure 5.6) are constructed from machined components, is assumed that the encoder measurements are aligned with the body frame in a more accurate manner than the accelerometers are placed and thus are suitable as a baseline measurement.

For each axis the perceived angular velocity and acceleration for the off-axis components are zero. From this the estimate $\hat{\boldsymbol{x}}$ of the vector $\boldsymbol{x}$ is formed, noting that the linear acceleration of the origin of the test rig is only affected by the acceleration due to gravity,

$$\begin{aligned}
\hat{\boldsymbol{x}}_x &= \begin{bmatrix} {}^i\boldsymbol{g}_x & \hat{\dot{\boldsymbol{\omega}}}_x & 0 & 0 & 0 & 0 & 0 & \hat{\boldsymbol{\omega}}_x^2 & 0 & 0 \end{bmatrix}^\mathsf{T} \\
\hat{\boldsymbol{x}}_y &= \begin{bmatrix} {}^i\boldsymbol{g}_y & 0 & \hat{\dot{\boldsymbol{\omega}}}_y & 0 & 0 & 0 & 0 & 0 & \hat{\boldsymbol{\omega}}_y^2 & 0 \end{bmatrix}^\mathsf{T} \\
\hat{\boldsymbol{x}}_z &= \begin{bmatrix} {}^i\boldsymbol{g}_z & 0 & 0 & \hat{\dot{\boldsymbol{\omega}}}_z & 0 & 0 & 0 & 0 & 0 & \hat{\boldsymbol{\omega}}_z^2 \end{bmatrix}^\mathsf{T}
\end{aligned} \tag{5.19}$$

where ${}^i\boldsymbol{g}_x = R_x(-\theta_x)\begin{bmatrix} -g & 0 & 0 \end{bmatrix}^\mathsf{T}$, ${}^i\boldsymbol{g}_y = R_y(-\theta_y)\begin{bmatrix} 0 & 0 & -g \end{bmatrix}^\mathsf{T}$ and ${}^i\boldsymbol{g}_z = R_z(-\theta_z)\begin{bmatrix} 0 & -g & 0 \end{bmatrix}^\mathsf{T}$. In this case the three vectors representing gravity are the gravity as seen in the local frame i. The test rig is reasonably aligned such that the $\hat{\boldsymbol{x}}$ axes are aligned with the gravity vector in the inertial frame when $\theta_x = 0$, $\theta_y = -\pi/2$ and $\theta_z = -\pi/2$. Section 5.5.2 examines the effects of misalignment on the system and how this might be compensated.

The angular velocity and acceleration estimates are then obtained offline via zero phase delay forward/backward Kalman filter (detailed in 5.3.1.1) as

$$\begin{aligned}
\begin{bmatrix} \hat{\dot{\boldsymbol{\omega}}}_x & \hat{\boldsymbol{\omega}}_x \end{bmatrix} &= Kalman(\theta_x), \\
\begin{bmatrix} \hat{\dot{\boldsymbol{\omega}}}_y & \hat{\boldsymbol{\omega}}_y \end{bmatrix} &= Kalman(\theta_y), \\
\begin{bmatrix} \hat{\dot{\boldsymbol{\omega}}}_z & \hat{\boldsymbol{\omega}}_z \end{bmatrix} &= Kalman(\theta_z).
\end{aligned} \tag{5.20}$$

The estimated vectors from (5.19) are populated with the gravity components and the components from (5.20) and arranged into a $10 \times K$ matrix as

$$\hat{\boldsymbol{x}} = \begin{bmatrix} \hat{\boldsymbol{x}}_{x,l} & \hat{\boldsymbol{x}}_{y,m} & \hat{\boldsymbol{x}}_{z,n} \end{bmatrix}, \tag{5.21}$$

where $l = 1 \ldots L$, $m = 1 \ldots M$ and $n = 1 \ldots N$ are the number of samples taken about each axis, and $K = L + M + N$.

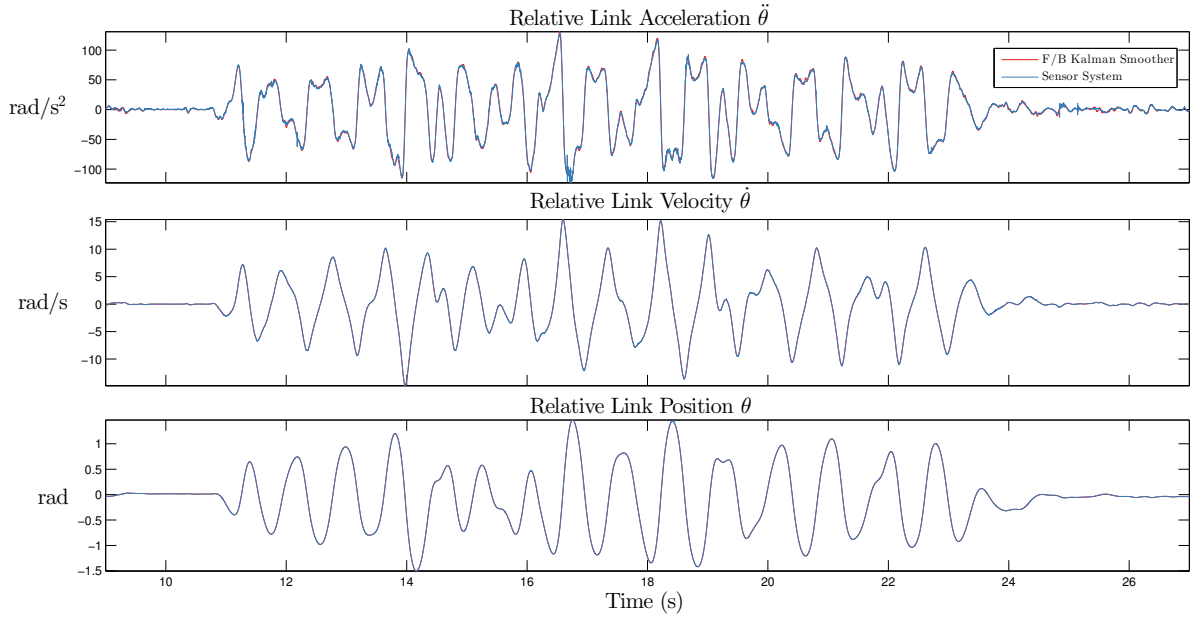

Figure 5.7: Full chaotic motion profile experiment range showing angular acceleration, velocity and position.

Similarly the acceleration components collected during the test rig rotation procedure are arranged into a $10 \times K$ matrix as

$$ {}^{j'}\boldsymbol{a} = \begin{bmatrix} {}^{j'}\boldsymbol{a}_{x,l} & {}^{j'}\boldsymbol{a}_{y,m} & {}^{j'}\boldsymbol{a}_{z,n} \end{bmatrix}. \tag{5.22} $$

The vector of error terms $\boldsymbol{e} = \begin{bmatrix} {}^{j}\boldsymbol{E} & {}^{j}\boldsymbol{\delta} \end{bmatrix}^{\mathsf{T}}$ can be found for each of the j accelerometers as the solution to

$$ \boldsymbol{e}_j = \min_{{}^{j}\boldsymbol{E},{}^{j}\boldsymbol{\delta}} \sum_{k} (||\boldsymbol{B}_j \hat{\boldsymbol{x}}_k - {}^{j}_{j'}\boldsymbol{R}\, {}^{j'}\boldsymbol{a}_k||)^2. \tag{5.23} $$

Calibration for the relative accelerometer ${}^{k'}\boldsymbol{a}$ on link l_{i-1} is carried out in the same manner. In this case the $\hat{\boldsymbol{x}}$ axis of link l_{i-1} is fixed to be collinear with the $\hat{\boldsymbol{x}}$ axis of link l_i such that they rotate fixed together as a single rigid body. The position vector ${}^{i-1}\boldsymbol{r}_k$ is modified to account for the extra length introduced by fixing the two links, with the extra length being accounted for during the system operation.

Based on data acquired from the test rig outlined in 5.2, Table 5.6 shows the ideal positions and their offsets and components that build the rotation correction matrix as computed from the calibration procedure. The significant offsets, particularly in the z components will lead to errors in the estimated states if not accounted for.

5.5 System Results

The experimental results obtained from the test apparatus are based on two motion profiles. The first motion profile aims to examine the system's performance under unknown and chaotic motion and was executed by simply actuating the upper link by hand to produce the desired motion at the lower joint and lower link. The second profile is a simple drop test whereby the pendulum starts off stationary and horizontal and is let to drop. This test aims to examine the system's performance when undergoing motions of low velocity and acceleration amplitude. During both the experiments data from all eight accelerometers and the two encoders was streamed to a host computer and captured to text file. System bandwidth is not examined within this work.

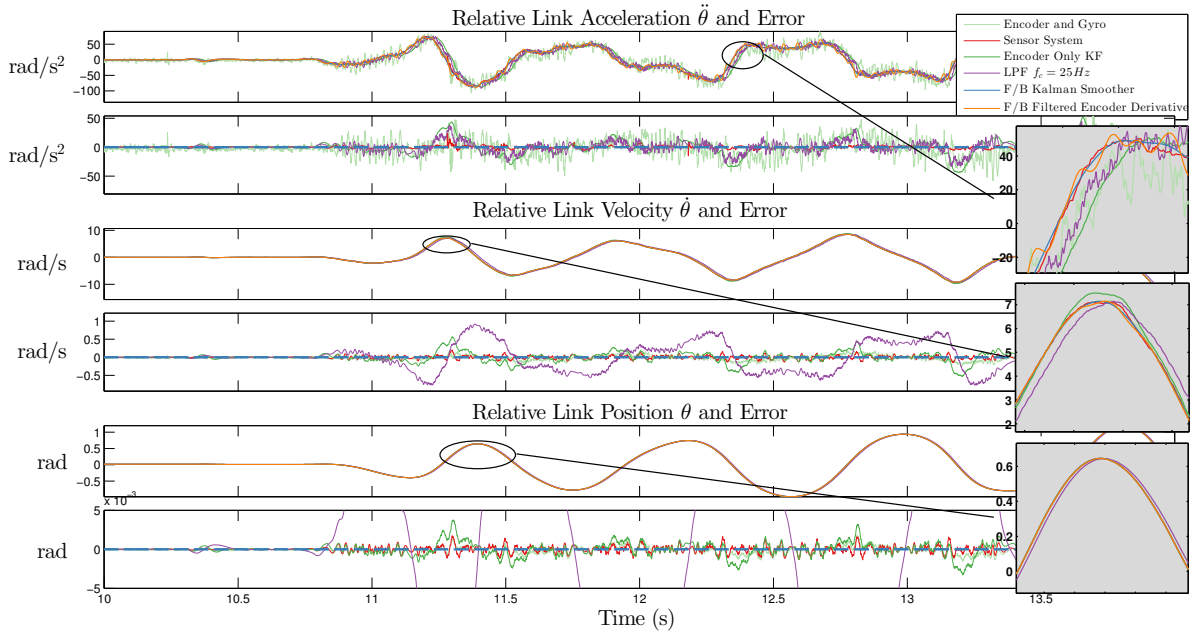

Figure 5.8: Four second window showing angular acceleration, velocity and position as measured by the joint sensor system (top) and the error from F/B Kalman filter (bottom).

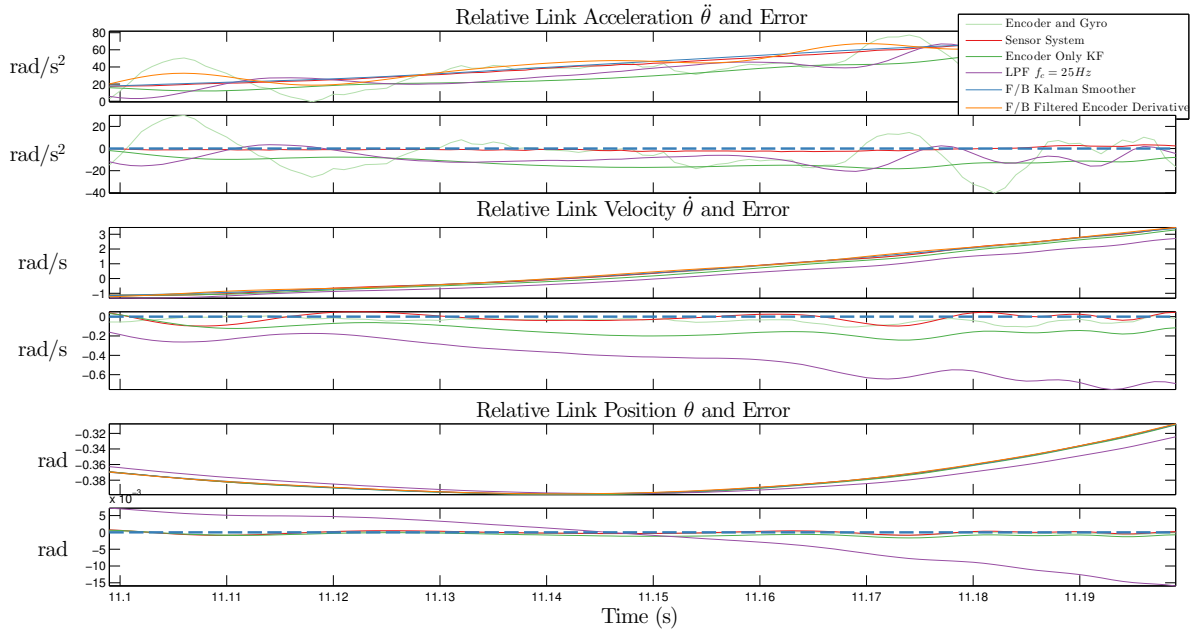

Figure 5.9: 0.1s window showing the same states as above.

Figure 5.7 shows the full experimental range of the chaotic motion test. Figures 5.8 and 5.9 go on to show the joint sensor's three relative states during a 4 second window (Figure 5.8) and 0.1 second window (Figure 5.9). Within these two plots the RMS error as compared to the zero delay (forward/backward) offline Kalman filter as detailed in Section 5.3.1.1 is given below each state.

Similarly Figure 5.10 shows the full range of the slow pendulum drop test. In this test we further examine a 4s window at 38s as presented in Figure 5.11. As with the chaotic motion test the RMS errors are also presented in this plot.

Table 5.7 compares the RMS error of each experiment to online Kalman Filter, low pass filter and gyro and encoder systems. In referring to this and the plots outlined, it is clear

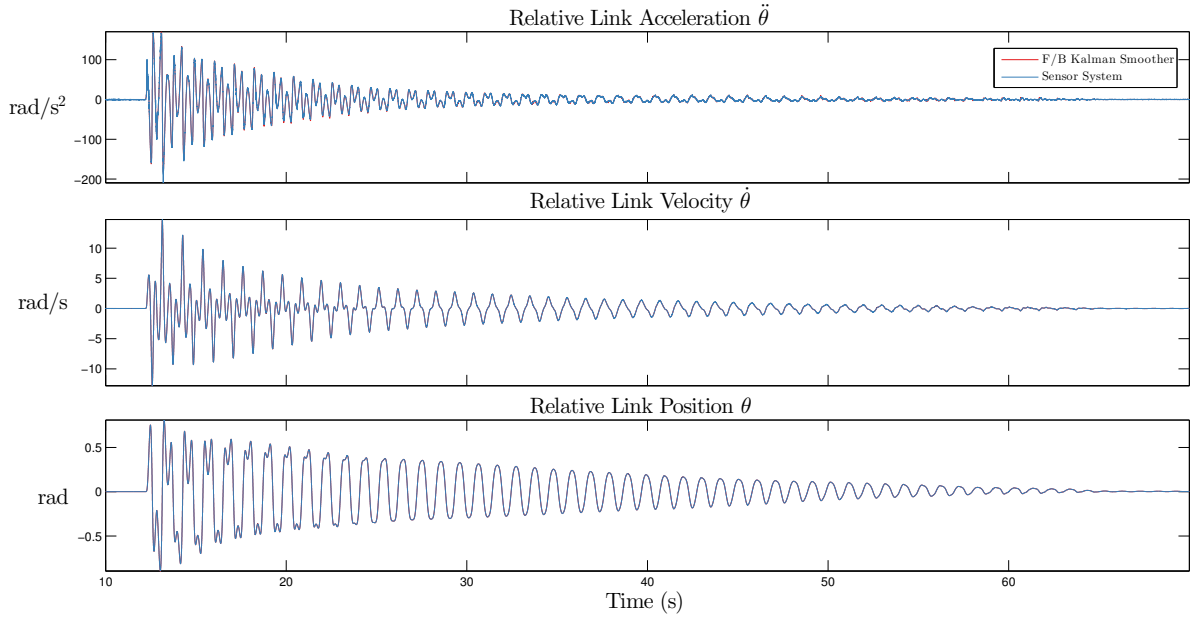

Figure 5.10: Full slow motion profile experiment range showing angular acceleration, velocity and position.

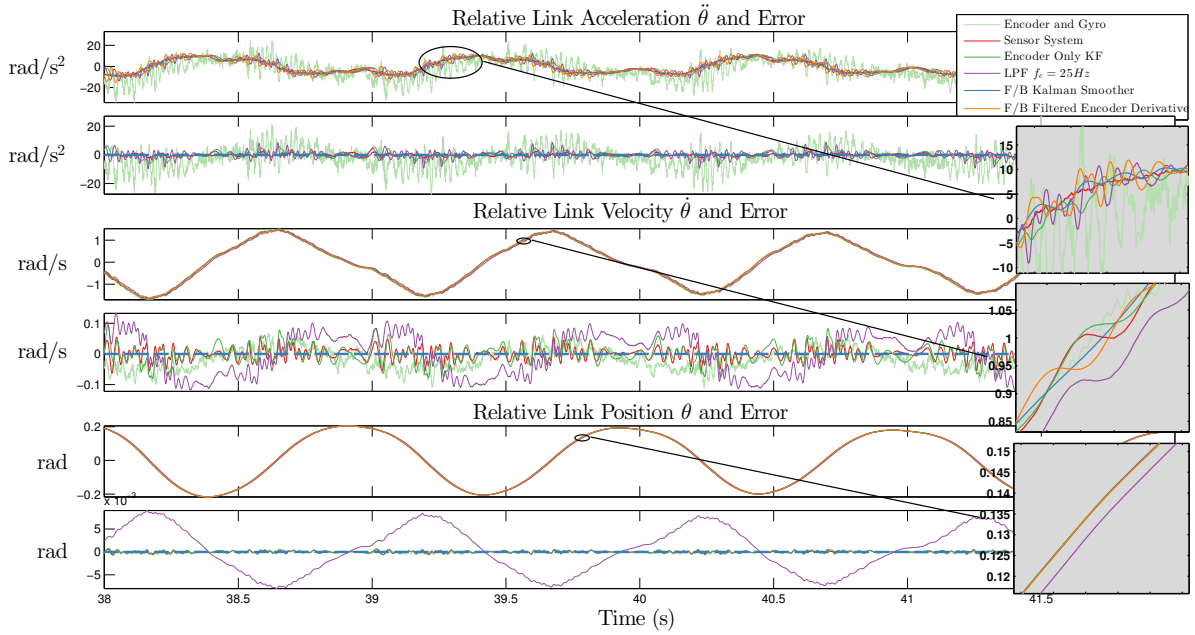

Figure 5.11: 4s window of slow motion profile showing angular acceleration, velocity and position as measured by the joint sensor system (top) and the error from F/B Kalman filter (bottom).

that the sensor system performs well when compared to these three online methods and in particular outperforms them in the velocity and acceleration states. It can be seen that the sensor system does not suffer from the significant phase delay in the acceleration and velocity terms that Kalman and LPF methods are vulnerable to. This performance increase can be attributed to the introduction of a measurement for these two states into the sensor system, whereas the online Kalman and LPF methods only have a positional measurement available.

In examining the gyro and encoder system it is shown that unlike the Kalman and LPF system this methods accurately tracks both the positional state and the velocity state

Table 5.7: RMS error of calibrated joint sensor compared with online methods, both chaotic and slow motion profiles.

		θ (rad)	$\dot{\theta}$ (rad s^{-1})	$\ddot{\theta}$ (rad s^{-2})
Chaotic Profile	Online KF Encoder	0.0008	0.1289	10.8358
	Online LPF Encoder	0.0175	0.3176	7.9664
	Online Gyro and Encoder	0.0004	0.0535	11.8972
	Full Calib Sensor	0.0004	0.0382	2.0578
Slow Profile	Online KF Encoder	0.0006	0.0964	8.2134
	Online LPF Encoder	0.0075	0.1926	5.5021
	Online Gyro and Encoder	0.0002	0.0392	7.3884
	Full Calib Sensor	0.0002	0.0187	1.3033

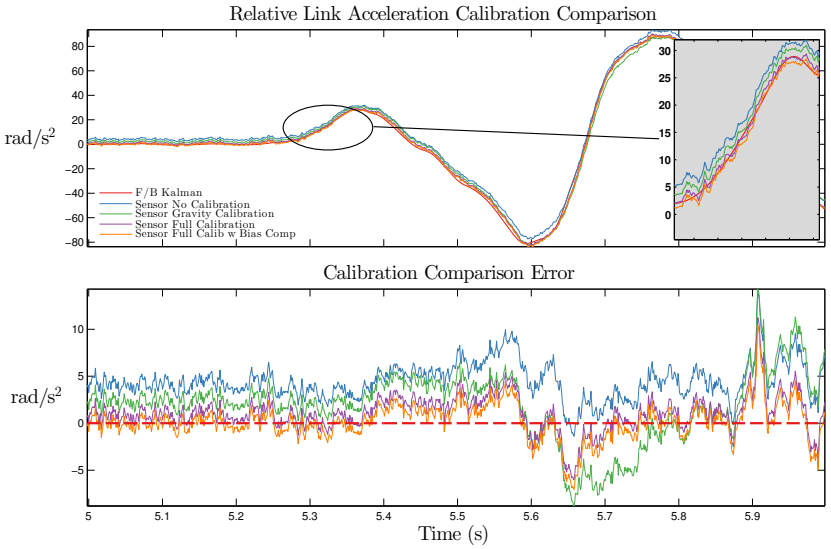

Figure 5.12: Comparison of the calibrated and uncalibrated acceleration states. Data based on *LIS3DSH* sensors.

well. However it is evident that this particular formulation is not capable of tracking the acceleration term as well as the sensor system and this term suffers from significant noise and phase delay. Comparing this system to the joint sensor system in particular highlights the benefits of providing a measurement for each state.

5.5.1 Effects of System Calibration

Figure 5.12 and Table 5.8 show the performance effects of the calibration methods on the joint sensor system. This data also shows results from an early version of the test rig. This early version employed ST Micro *LIS3DSH* accelerometers (no gyroscopes) and is included as it both demonstrates the performance of the system under a more chaotic motion profile and shows the increase in performance attributed to the calibration procedures. In this version the accelerometers were not placed as accurately as the *LSM6DS3* based test rig and as such a more severe performance increase resulted between the calibrated and uncalibrated system. This system is only presented in this section.

The plots in Figure 5.12 show the *LIS3DSH* system at the various stages of calibration. These plots show that the uncalibrated systems suffer from varying levels of bias over their experimental range. Each successive level of calibration is able to reduce these effects until

Table 5.8: RMS error of calibrated and uncalibrated joint sensor compared with online methods. These results based on the chaotic motion profile.

		θ (rad)	$\dot{\theta}$ (rad s^{-1})	$\ddot{\theta}$ (rad s^{-2})
LIS3DSH Based	Online KF Encoder	0.0017	0.2980	25.5378
	Online LPF Encoder	0.0284	0.6210	16.1780
	Uncalibrated Sensor	0.0003	0.0570	6.5242
	Gravity Calib Sensor	0.0002	0.0450	5.2277
	Full Calib Sensor	0.0002	0.0394	4.2807
	Full Calib Sensor w Bias Comp	0.0002	0.0384	4.1425
LSM6DS3 Based	Online KF Encoder	0.0008	0.1289	10.8358
	Online LPF Encoder	0.0175	0.3176	7.9664
	Uncalibrated Sensor	0.0004	0.0390	2.2345
	Gravity Calib Sensor	0.0004	0.0384	2.1065
	Full Calib Sensor	0.0004	0.0382	2.0578

only slight levels of bias become apparent.

Although the uncalibrated sensor (in both cases) still presents better estimates of the relative states than the online methods, the successive levels of calibration applied to the system will increase the performance and remove the bias effects attributed to the sensor properties and poor placement.

5.5.2 Effects of a Misaligned System

From Figure 5.12 it is evident that although the calibration procedure will eliminate the majority of the bias in the acceleration term, the sensor system may still be subject to some level of bias in this term. This bias propagates through the system into the velocity and position terms, reducing their performance and is an effect from a misalignment when zeroing the incremental encoder. If the encoder is not zeroed accurately along the $\hat{\boldsymbol{x}}$ axis of link l_{i-1} as in Figure 3.2 then the vector $\boldsymbol{a}_{\text{imu}}$ in (4.8) is not rotated correctly and a bias becomes apparent at the output.

Although the results in Table 5.8 show that in this case the bias is somewhat minimal, earlier experiments have shown that a misaligned encoder can lead a drastic reduction in the overall system performance. This bias can be corrected online by the relative UKF by augmenting the relative state vector $\boldsymbol{x}_{\text{rel},k}$ with a slow bias correcting term θ_δ

$$\boldsymbol{x}_{\text{rel\_aug},k} = \begin{bmatrix} \boldsymbol{x}_{\text{rel},k} \\ \theta_\delta \end{bmatrix}_{k-1} + \boldsymbol{v}_{\text{rel},k-1}. \tag{5.24}$$

$\boldsymbol{x}_{\text{rel\_aug},k}$ then replaces $\boldsymbol{x}_{\text{rel},k}$ as the state vector in the relative UKF component. During the measurement update, Equation (3.13) when combined with (3.18) is augmented as

$${}^{i-1}\boldsymbol{a}_o = \boldsymbol{R}_z(\theta_{\text{rel}} - \theta_\delta)\ {}^{i}\boldsymbol{a}_o. \tag{5.25}$$

and the observation equation is modified to become

$${}^{i-1}\boldsymbol{a}_k = \boldsymbol{R}_z(\theta_{\text{rel}} - \theta_\delta)\boldsymbol{a}_{\text{imu}} + \dot{\boldsymbol{\omega}}_{\text{rel}} \times {}^{i-1}\boldsymbol{r}_k + \boldsymbol{\omega}_{\text{rel}} \times (\boldsymbol{\omega}_{\text{rel}} \times {}^{i-1}\boldsymbol{r}_k). \tag{5.26}$$

The effect of the bias estimator can be seen in Figure 5.12 between 5s and 5.4s where the acceleration error is centred around zero. In our case this also results in a slightly better RMS error in the *LIS3DSH* based system in Table 5.8.

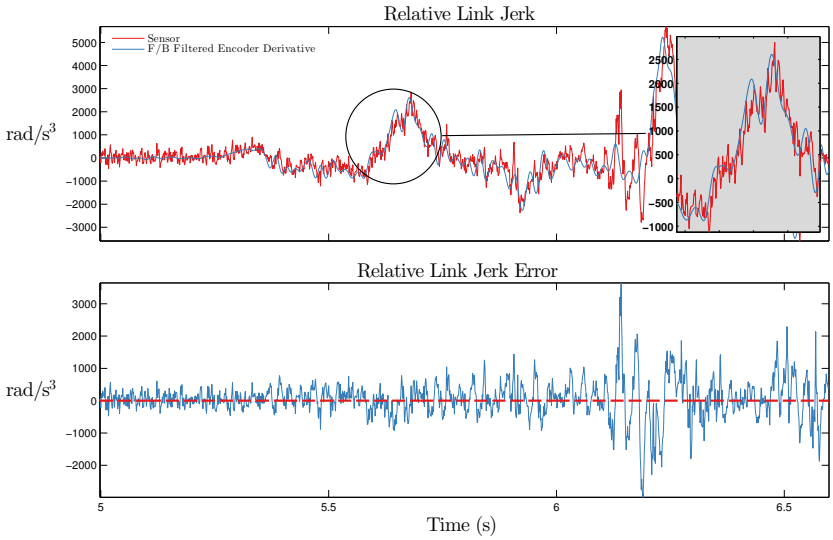

Figure 5.13: Sensor system jerk state and error.

5.5.3 Estimate of Angular Jerk

An estimate of the relative jerk is also made available by the sensor system (Figure 5.13). There is no sensor measurement associated with the angular jerk term and as such it is driven by process noise. This is similar to the gyroscope and encoder reference system in Section 5.3.2.1 where an estimate of the angular acceleration is made available, but also driven by process noise. The result of this is a jerk term that is somewhat noisy and displaying noticeable phase delay. This term may only prove useful in slower moving systems and may be a topic for future work.

5.5.4 Joint State Information from the AO-IMU

Also available from the sensor system are link states from the AO-IMU. This information describes the angular acceleration and velocity, and the linear acceleration of point o in the inertial frame. These values are used as a component of the joint sensor system, but may be made available for use in other systems.

5.6 Summary

In this section the experimental apparatus, baselines for comparison and online methods used to assess the performance of the sensor system have been detailed.

The performance of the system was assessed based on two motion profiles. Within this a chaotic motion profile was employed to assess the performance of the system when undergoing large and unknown accelerations. Along with this a zero torque drop test was employed to examine the system when undergoing low angular velocities. In both of these experiments the joint sensor system was demonstrated to perform well under the two motion profiles. Although only reasonably small gains in performance were evident in the position state, the angular velocity and in particular the angular acceleration states demonstrated much greater performance than the existing online methods.

The performance of the calibration schemes in Section 5.4 was then examined. The experiments carried out on the chaotic motion profile demonstrated that the calibration methods worked sufficiently well to reduce the effects of bias due to the sensor effects

and misalignments. Interestingly, these experiments also demonstrated that even without calibration the joint sensor system outperformed the existing online methods.

Finally the sensor system was discovered to suffer somewhat from bias effects attributed to inaccurate zeroing of the positional encoder. As correctly zeroing the encoder and ensuring it is accurately aligned with the acceleration due to gravity measured by the accelerometers may prove to be time consuming or expensive, an online method was developed to correct for this. A bias term was introduced and means for correcting the misaligned system was discussed. This system showed positive results and could be replaced with the estimated bias value once correctly estimated.

Chapter 6

Extending the Sensor System

6.1 Introduction

In this chapter the plain sensor system as detailed in the previous chapters is expanded upon. It is suspected that while the plain system performs well, it is possible that the performance of the system is hindered under low velocities. The single relative accelerometer is also believed to be a source of performance limitation. It is also suspected that alternate system structures may be more suited to larger robotic systems.

Within this chapter we aim to investigate the performance of the system when augmented with additional accelerometers and gyroscope sensors. An alternate system structure that may be more suited to larger robotic systems is also investigated.

In Section 6.2 the base sensor system is augmented to incorporate measurements from single gyroscope sensors as placed on each link. Section 6.3 builds models for and compares the performance of a system that incorporates multiple relative accelerometers as opposed to the single accelerometer employed in the base sensor system. In Section 6.4 an alternate joint sensor system structure is investigated that takes inspiration from the work done in Section 6.3. Finally, in Section 6.5 we revisit each system that incorporated gyroscope sensors and augment them to consider multiple gyroscope sensors.

The systems studied within this section are all based on the data from the chaotic motion test as shown in Figure 5.7 in Section 5.5.

6.2 Addition of Gyroscope Sensors

In recent times the cost of MEMs inertial sensors has drastically reduced while the capability of the sensors themselves has increased. In particular, not only has the specification[1] of the sensor increased, but manufacturers have move to consolidate multiple MEMs devices onto one integrated circuit. As an example, at the time of writing the ST Micro $LIS3DSH$, costing $US\$2.41$ is a three axis accelerometer unit with a digital output. In comparison ST Micro have since released the $LSM6DS3$ at a cost of $US\$3.98$. This device has both three axis accelerometer with similar specification to the $LIS3DSH$ and a three axis gyroscope built into a sensor in a package of similar size to the $LIS3DSH$.

By incorporating a gyroscope measurement the system presented in Section 5.3.2.1 demonstrated an increase in performance, particularly in the velocity state. Madgwick et al. (2013) also noted that an AO-IMU by itself may suffer from poor performance at low velocities. The addition of a gyro sensor may help resolve this issue and along with the low

[1] Such as sensor noise, drift due to temperature, accuracy, etc.

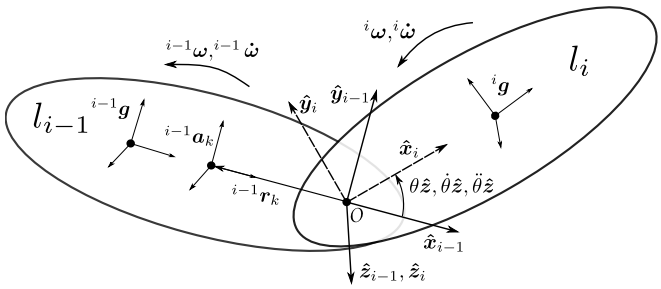

Figure 6.1: Plain system with a single gyro on each link.

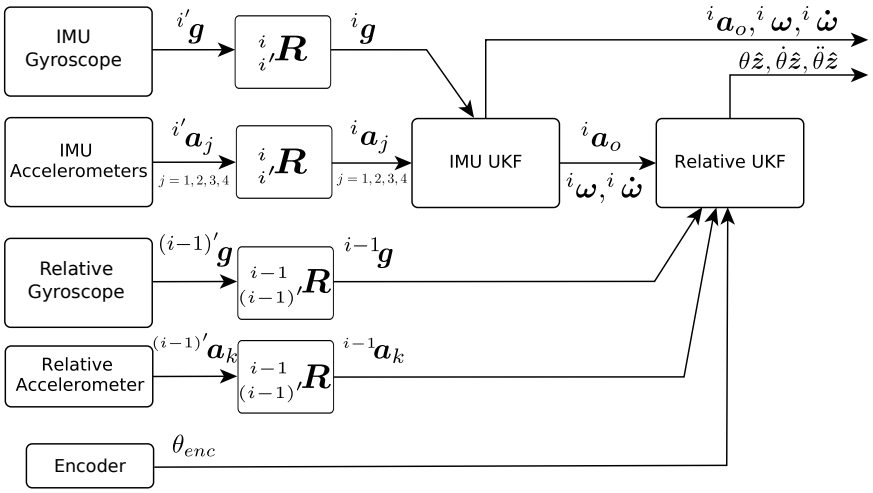

Figure 6.2: Gyro augmented plain system sensor and UKF data flow.

cost and high performance specification of the combined inertial devices, an investigation into the effects of the sensors on the joint sensor system is warranted.

In this section the plain sensor system is augmented to include measurements from a single gyroscope attached to each link and the performance of this augmented system is investigated.

6.2.1 Gyroscope Augmented System Model

The gyroscope sensor is modelled as per (3.2.2). Within this the gain parameters are set to unity as $\boldsymbol{S}_g = \left[\begin{smallmatrix} 1 & 0 & 0 \\ 0 & 1 & 0 \\ 0 & 0 & 1 \end{smallmatrix}\right]$ and the bias term $^{i}\boldsymbol{b}_g$ is simply taken from the initial gyroscope bias. The experimental time is short so moving bias is not considered.

Figure 6.1 shows the system model augmented as to incorporate the measurements from the gyroscopes and Figure 6.2 shows the data flow through the estimators for this system. In referring to Figure 6.1 the calibrated gyros are placed on links l_i and l_{i-1} and the system is modified as follows. The AO-IMU component on link l_i is first augmented to compare its estimated state against both the accelerometers and the gyroscope. The AO-IMU measurement vector $\boldsymbol{y}_{\text{imu}}$ is augmented with a gyro placed at $^{i}\boldsymbol{g}$ on the link l_i and the AO-IMU measurement function (4.4) from Section 4.4.1 is modified to directly compare the AO-IMU's angular velocity against the calibrated gyroscope output,

$$\begin{bmatrix} ^{i}\boldsymbol{a}_1 \\ ^{i}\boldsymbol{a}_2 \\ ^{i}\boldsymbol{a}_3 \\ ^{i}\boldsymbol{a}_4 \\ ^{i}\boldsymbol{g} \end{bmatrix}_k = \begin{bmatrix} \boldsymbol{B}h_{\text{ix}}(\boldsymbol{x}_{\text{imu}}) \\ \boldsymbol{\omega}_{\text{imu}} \end{bmatrix}_k + \boldsymbol{w}_{\text{imu},k}, \tag{6.1}$$

Table 6.1: Gyroscope augmented system parameters parameters

$\sigma_{\text{imu,lin}}$	3	$\text{m}\,\text{s}^{-3}$
$\sigma_{\text{imu,rot}}$	20	$\text{rad}\,\text{s}^{-3}$
$\sigma_{\text{rel,rot}}$	200	$\text{rad}\,\text{s}^{-3}$
$R_{\text{ukf,enc}}$	2.1343×10^{-9}	rad
$R_{\text{ukf,gyro}}$	6.9787×10^{-5}	$\text{rad}\,\text{s}^{-1}$

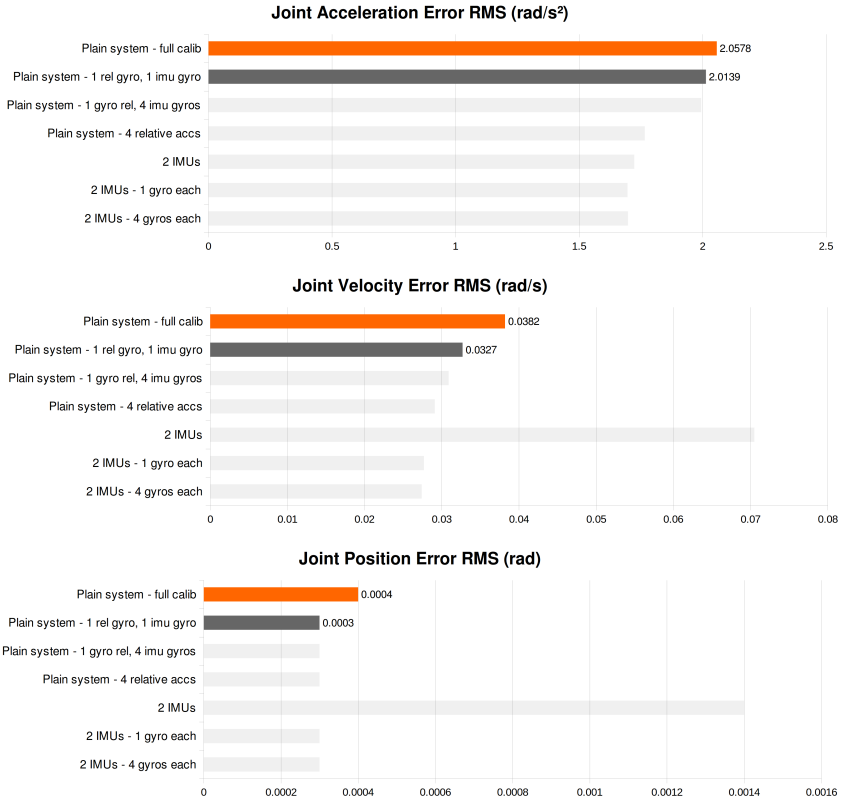

Figure 6.3: RMS error results of plain system with a single gyro on each link.

where $\boldsymbol{\omega}_{\text{imu}} = \begin{bmatrix} \omega_{\text{imu},x} & \omega_{\text{imu},y} & \omega_{\text{imu},z} \end{bmatrix}^{\mathsf{T}}$.

The relative components are then augmented to include measurements from the gyroscope. As with the IMU section the relative UKF measurement vector $\boldsymbol{y}_{\text{rel}}$ is modified to incorporate a gyro placed at ${}^{i-1}\boldsymbol{g}$ and the measurement function (4.7) is modified to compare the relative angular velocity to the gyroscope,

$$\begin{bmatrix} {}^{i-1}\boldsymbol{a}_1 \\ {}^{i-1}\boldsymbol{g} \\ \theta_{\text{enc}} \end{bmatrix}_k = \begin{bmatrix} {}^{i-1}\boldsymbol{a}_k \\ \boldsymbol{\omega}_{\text{rel}} \\ \theta_{\text{rel}} \end{bmatrix}_k^{\mathsf{T}} + \boldsymbol{w}_{\text{rel},k}, \tag{6.2}$$

where $\boldsymbol{\omega}_{\text{rel}} = \boldsymbol{\omega}_{\text{imu}} - \dot{\theta}_{\text{rel}}\hat{\boldsymbol{z}}$ is taken from (4.9) and ${}^{i-1}\boldsymbol{a}_k$ transforms the relative state to a linear acceleration measurement as given in (4.8).

6.2.2 Results

Figure 6.3 compares the RMS errors of the fully calibrated plain joint sensor system to the system as augmented with gyroscopes. It is found within this that only slight performance gains are evident in the acceleration term, however a higher performing angular velocity term is obtained from the addition of gyros. It is noted that these results present for a system

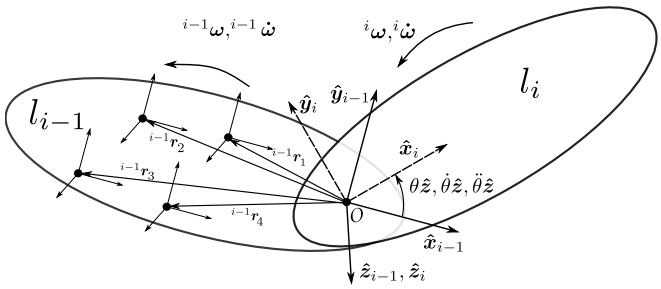

Figure 6.4: Plain system model with four relative accelerometers.

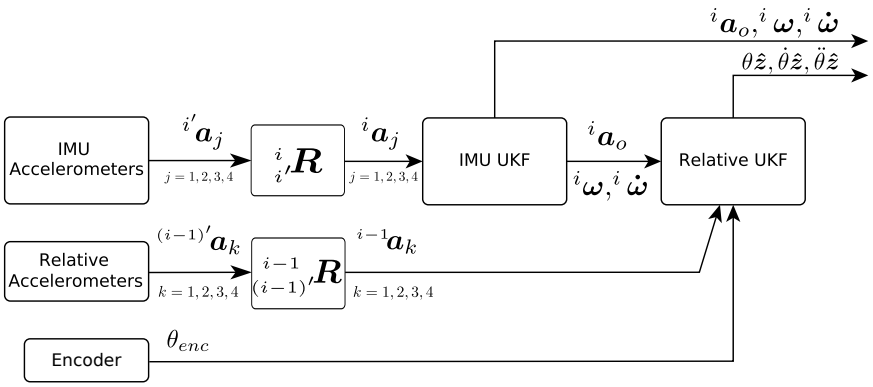

Figure 6.5: Four relative accelerometers system sensor and UKF data flow.

experiencing somewhat significant angular velocities and it is expected that while the gyros may not significantly contribute to large performance increases here, they will aid a system experiencing low angular velocities. This is further examined in Section 6.4.2.

6.3 Redundancy of Accelerometers

During early testing and experiments on the joint sensor system it became apparent that the use of a single relative accelerometer may be seen as a performance bottleneck in the output of the system. Figure 6.6 shows the system output compared to the plain AO-IMU output during a quiet period of the slow motion profile. Taking the RMS errors of the two estimates over the 1s window gives a value of $0.1721\text{rad}\,\text{s}^{-2}$ for the sensor system state and $0.0853\text{rad}\,\text{s}^{-2}$ for the AO-IMU output only. From this it is evident that the acceleration state for the sensor system output is somewhat noisier than the AO-IMU output. It is suspected that this drop in performance may be due to the AO-IMU having four accelerometers contributing to its output, whereas the relative system component goes on to compare this to a single accelerometer. The literature also confirms this suspicion. Madgwick et al. (2013) explored kinematically redundant AO-IMU based systems and demonstrated an inverse relationship exists between the RMS noise of the sensor output and the quantity of three axis accelerometers.

Given this evidence an experiment was performed to investigate the performance of the sensor system when redundant relative accelerometers were employed. Within this we simply augment the existing sensor system to incorporate four relative accelerometers and assess the performance as compared to the plain system.

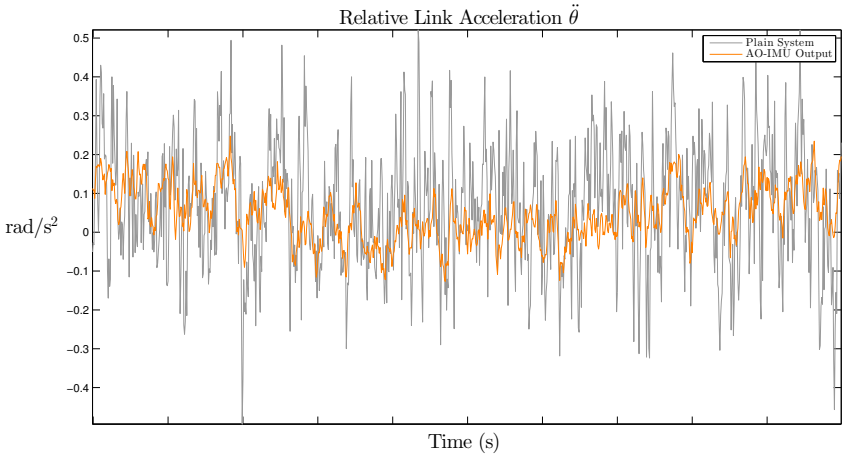

Figure 6.6: Comparison of sensor system acceleration state to AO-IMU acceleration state.

6.3.1 Redundant Accelerometer Augmented System Model

The redundant accelerometer system extends the base sensor system. Figure 6.4 shows the plain system augmented to incorporate four relative accelerometers and Figure 6.5 illustrates the flow of data, particularly data moving into the relative UKF, from the addition of the extra sensors.

From the original system relative kinematics presented in Section 3.3.2, the acceleration of a point at k on link l_{i-1} is given as

$$ {}^{i-1}\boldsymbol{a}_k = {}^{i-1}\boldsymbol{a}_o + {}^{i-1}\dot{\boldsymbol{\omega}} \times {}^{i-1}\boldsymbol{r}_k + {}^{i-1}\boldsymbol{\omega} \times ({}^{i-1}\boldsymbol{\omega} \times {}^{i-1}\boldsymbol{r}_k), \tag{6.3} $$

which is then reformulated into a matrix equation as

$$ {}^{i-1}\boldsymbol{a}_k = \boldsymbol{C}_k \boldsymbol{x}_{\text{multrel}}, \tag{6.4} $$

in a similar manner a given in the AO-IMU kinematics in 3.3.1. In this case the matrix $\boldsymbol{C}_k$ is built from the position of the accelerometers ${}^{i-1}\boldsymbol{r}_k$ placed on link l_{i-1} and the vector

$$ \boldsymbol{x}_{\text{multrel}} = \begin{bmatrix} a_x & a_y & a_z & \dot{\omega}_x & \dot{\omega}_y & \dot{\omega}_z & \omega_x\omega_y & \omega_x\omega_z & \omega_y\omega_z & \omega_x^2 & \omega_y^2 & \omega_z^2 \end{bmatrix}^\mathsf{T}, \tag{6.5} $$

forms the relative varying components. Four accelerometers are then placed on the link l_{i-1} and (6.4) is then stacked as

$$ \boldsymbol{y}_{\text{multrel}} = \boldsymbol{C}\boldsymbol{x}_{\text{multrel}}. \tag{6.6} $$

Here the acceleration measurements are stacked as

$$ \boldsymbol{y}_{\text{multrel}} = \begin{bmatrix} {}^{i-1}\boldsymbol{a}_1 & {}^{i-1}\boldsymbol{a}_2 & {}^{i-1}\boldsymbol{a}_3 & {}^{i-1}\boldsymbol{a}_4 \end{bmatrix}^\mathsf{T}, \tag{6.7} $$

and the position matrices are stacked as

$$ \boldsymbol{C} = \begin{bmatrix} \boldsymbol{C}_1 & \boldsymbol{C}_2 & \boldsymbol{C}_3 & \boldsymbol{C}_4 \end{bmatrix}^\mathsf{T}. \tag{6.8} $$

The system state estimation is now augmented to make use of the redundant relative accelerometers. The state transition function for the relative UKF given in Section 4.4.2 remains unchanged, however the measurement function is modified to incorporate the extra information from the accelerometers. The measurement equation (4.7) is modified as

$$ \begin{bmatrix} {}^{i-1}\boldsymbol{a}_1 \\ {}^{i-1}\boldsymbol{a}_2 \\ {}^{i-1}\boldsymbol{a}_3 \\ {}^{i-1}\boldsymbol{a}_4 \\ {}^{i}\theta_{\text{enc}} \end{bmatrix} = \begin{bmatrix} \boldsymbol{C}h_{\text{multrel}}(\boldsymbol{x}_{\text{imu}}, \boldsymbol{x}_{\text{rel}}) \\ \theta_{\text{rel}} \end{bmatrix}_k + \boldsymbol{w}_{\text{rel},k}. \tag{6.9} $$

Table 6.2: Redundant relative accelerometer system parameters parameters

$\sigma_{\text{imu,lin}}$	3	$\text{m}\,\text{s}^{-3}$
$\sigma_{\text{imu,rot}}$	20	$\text{rad}\,\text{s}^{-3}$
$\sigma_{\text{rel,rot}}$	200	$\text{rad}\,\text{s}^{-3}$
$R_{\text{ukf,acc}}$	0.0111	$\text{m}\,\text{s}^{-2}$
$R_{\text{rel,acc}}$	0.0111	$\text{m}\,\text{s}^{-2}$
$R_{\text{rel,enc}}$	2.1343×10^{-9}	rad

In this case k represents the time step and $h_{\text{multrel}}(\cdot)$ is a non-linear function mapping the AO-IMU states to the relative state such that $\boldsymbol{x}_{\text{multrel}} = h_{\text{multrel}}(\boldsymbol{x}_{\text{imu}}, \boldsymbol{x}_{\text{rel}})$. Again, the components for (6.5) are derived from the relative kinematics outlined in 3.3.2 and are given as

$$\begin{aligned} \boldsymbol{a}_{\text{multrel}} &= \boldsymbol{R}_z(\theta_{\text{rel}})\boldsymbol{a}_{\text{imu}}, \\ \dot{\boldsymbol{\omega}}_{\text{multrel}} &= \dot{\boldsymbol{\omega}}_{\text{imu}} - \ddot{\theta}_{\text{rel}}\hat{\boldsymbol{z}}, \\ \boldsymbol{\omega}_{\text{multrel}} &= \boldsymbol{\omega}_{\text{imu}} - \dot{\theta}_{\text{rel}}\hat{\boldsymbol{z}}. \end{aligned} \tag{6.10}$$

The four accelerometers are calibrated using the same method given in Section 5.4.

6.3.2 Results

Table 6.2 shows the parameters as used in the redundant relative system experiments. In this the same accelerometers are installed throughout the systems and as such the noise parameters $R_{\text{ukf,acc}}$ and $R_{\text{rel,acc}}$ are the same.

In referring to Figure 6.7 an increase in the performance of all the states over that of the plain system is apparent. Figure 6.8 then shows the system output compared to the plain AO-IMU states as previously shown in Figure 6.6, except in this case the angular acceleration state from the augmented system in included. For the same quiet time period as the plain system and AO-IMU previously given the augmented sensor system has an RMS error of $0.0916\text{rad}\,\text{s}^{-2}$. This is similar in performance to the plain AO-IMU output and indeed of lower noise than the plain sensor system. The four relative accelerometer system shows a clear improvement over that of the plain sensor system and confirms the belief that an increase in noise is apparent when only employing a single relative accelerometer.

Figure 6.7: RMS error results comparing the plain system with the system augmented with four relative accelerometers.

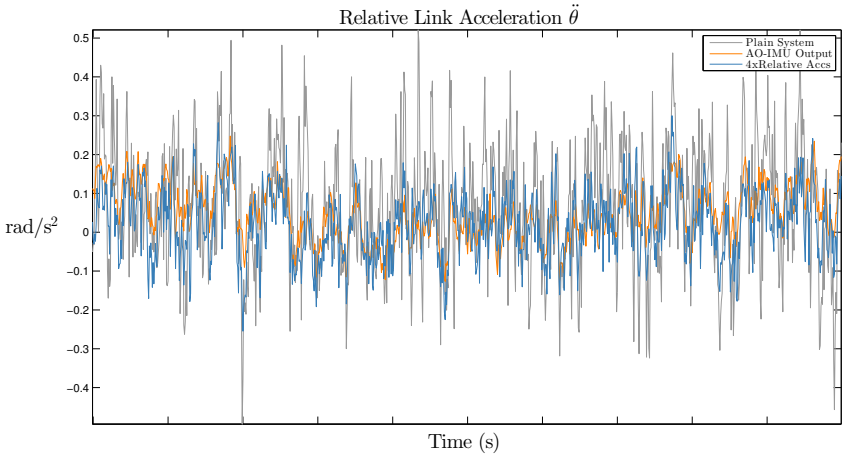

Figure 6.8: Comparison of sensor system acceleration state to AO-IMU acceleration state and augmented four relative accelerometer system.

6.4 Multiple AO-IMUs

Noting the improved performance of the multiple relative accelerometer system (Section 6.3) over that of the plain system, an interesting alternate approach is to consider placing an AO-IMU on each link and forgo the relative accelerometer altogether.

In considering the work on joint state estimation on large humanoid robotic systems in Rotella et al. and Xinjilefu where there is a requirement to estimate the state of all joints, a system such as this might be more suited to the estimation task as there would be no need place a relative accelerometer on the previous link for each of the joints whose states

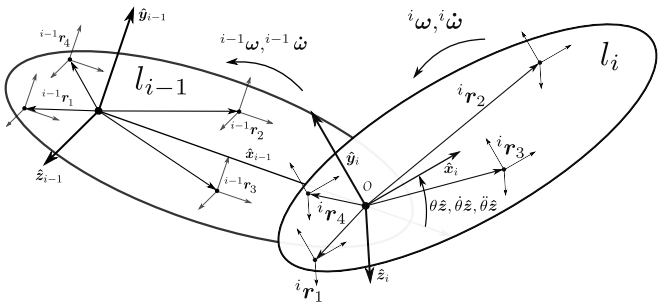

Figure 6.9: IMU placed on each link.

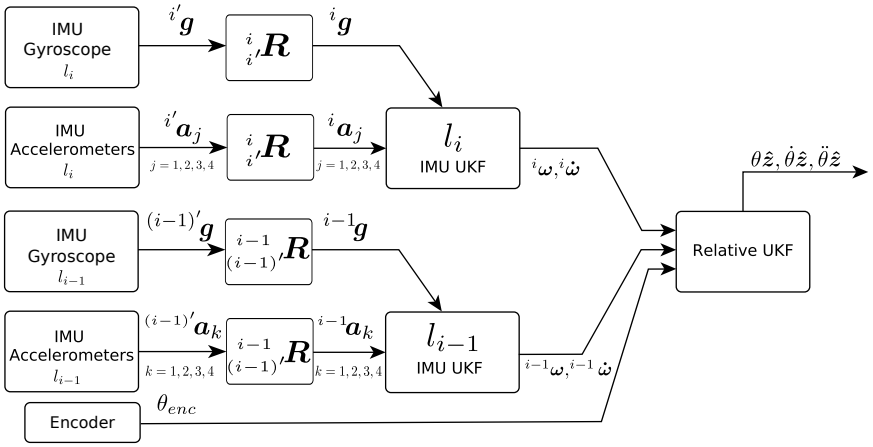

Figure 6.10: Multiple IMU system sensor and UKF data flow.

are being estimated. Instead in this revised system, the relative accelerometer would be replaced by the previous link AO-IMU and the angular joint acceleration and velocity would be obtained from the difference between the two AO-IMUs as placed on the links. A floating base robotic system would require an AO-IMU fixed to the base to define the angular acceleration and velocity of the moving base.

This section describes the modelling and compares the experimental results of a multi AO-IMU based sensor system to the plain joint sensor system.

6.4.1 Multiple IMU System Model

In this system each AO-IMU defines the angular acceleration and velocity and the linear acceleration of the link it is fixed to.

In this an IMU is placed on the link l_i and link l_{i-1}. The kinematics for each AO-IMU are then written in the same manner as given in Section 3.1. For each of the two AO-IMUs the state at time step k is updated by a separate UKF. The AO-IMU state vectors, denoted as $\boldsymbol{x}_{\text{imu},i-1}$ and $\boldsymbol{x}_{\text{imu},i}$ are constructed in the same manner given in the AO-IMU state estimation in section 4.4.1. Similarly the measurement function for each AO-IMU remains as given in Section 4.4.1.

In this formulation as each AO-IMU fully defines the angular acceleration and velocity of its respective link, the relative angular velocity and acceleration are easily obtained via the rule of summation of angular velocity and its derivative. The relative angular velocity and acceleration obtained from the two AO-IMUs, along with a positional measurement from the encoder become measurements that the relative UKF estimates are compared to. From (3.14) the relative angular velocities between the two link is given as

$$ {}^{i}\boldsymbol{\omega}_{i-1,i} = {}^{i}\boldsymbol{\omega} - {}^{i}\boldsymbol{\omega}_{i-1}, \tag{6.11} $$

Table 6.3: Multiple AO-IMU system parameters parameters

$\sigma_{\text{imu,lin}}$	3	$\text{m}\,\text{s}^{-3}$
$\sigma_{\text{imu,rot}}$	20	$\text{rad}\,\text{s}^{-3}$
$\sigma_{\text{rel,rot}}$	200	$\text{rad}\,\text{s}^{-3}$
$R_{\text{imu1,acc}}$	0.0111	$\text{m}\,\text{s}^{-2}$
$R_{\text{imu2,acc}}$	0.0111	$\text{m}\,\text{s}^{-2}$
$R_{\text{rel},\dot{\omega}}$	0.0475	$\text{rad}\,\text{s}^{-2}$
$R_{\text{rel},\omega}$	4.6435×10^{-5}	$\text{rad}\,\text{s}^{-1}$
$R_{\text{rel,enc}}$	2.1343×10^{-9}	rad
$R_{\text{imu1,gyro}}$	6.9787×10^{-5}	$\text{rad}\,\text{s}^{-1}$
$R_{\text{imu2,gyro}}$	6.9787×10^{-5}	$\text{rad}\,\text{s}^{-1}$

which is then expressed in the frame it is estimated in as

$$ {}^{i}\boldsymbol{\omega}_{i-1,i} = {}^{i}\boldsymbol{\omega} - {}^{i}_{i-1}\boldsymbol{R}({}^{i-1}\boldsymbol{\omega}_{i-1}). \tag{6.12} $$

In the experimental case, the rotation is about the $\hat{\boldsymbol{z}}$ axis and therefore has no effect. The relative angular velocity is then simply given as

$$ {}^{i}\boldsymbol{\omega}_{i-1,i} = {}^{i}\boldsymbol{\omega} - {}^{i-1}\boldsymbol{\omega}. \tag{6.13} $$

In a similar manner the relative angular acceleration between the two links is taken from (3.16) as

$$ {}^{i}\dot{\boldsymbol{\omega}}_{i-1,i} = {}^{i}\dot{\boldsymbol{\omega}} - {}^{i}\dot{\boldsymbol{\omega}}_{i-1} - {}^{i}\boldsymbol{\omega}_{i-1} \times {}^{i}\boldsymbol{\omega}, \tag{6.14} $$

which is again expressed in the respective frames as

$$ {}^{i}\dot{\boldsymbol{\omega}}_{i-1,i} = {}^{i}\dot{\boldsymbol{\omega}} - {}^{i}_{i-1}\boldsymbol{R}({}^{i-1}\dot{\boldsymbol{\omega}}_{i-1}) - {}^{i}_{i-1}\boldsymbol{R}({}^{i-1}\boldsymbol{\omega}_{i-1}) \times {}^{i}\boldsymbol{\omega}. \tag{6.15} $$

Once again, the rotation is constrained about the $\hat{\boldsymbol{z}}$ axis and has no effect and in the case of the angular acceleration the cross product term also goes to zero, resulting in the relative acceleration equation

$$ {}^{i}\dot{\boldsymbol{\omega}}_{i-1,i} = {}^{i}\dot{\boldsymbol{\omega}} - {}^{i-1}\dot{\boldsymbol{\omega}}. \tag{6.16} $$

Equations (6.13) and (6.16) are then directly employed during the relative state correction

$$ \begin{bmatrix} ({}^{i}\dot{\boldsymbol{\omega}} - {}^{i-1}\dot{\boldsymbol{\omega}})\hat{\boldsymbol{z}} \\ ({}^{i}\boldsymbol{\omega} - {}^{i-1}\boldsymbol{\omega})\hat{\boldsymbol{z}} \\ {}^{i}\theta_{\text{enc}} \end{bmatrix}_k = \begin{bmatrix} \ddot{\theta}_{\text{rel}} \\ \dot{\theta}_{\text{rel}} \\ \theta_{\text{rel}} \end{bmatrix}_k^{\mathsf{T}} + \boldsymbol{w}_{\text{rel},k}. \tag{6.17} $$

In this the angular velocity and acceleration components of link l_{i-1} are taken from $\boldsymbol{x}_{\text{imu,i}-1}$ and the same components from link l_i are taken from $\boldsymbol{x}_{\text{imu,i}}$ at time step k. In this case only the $\hat{\boldsymbol{z}}$ axis components of the two IMU's are used to form the relative measurements.

6.4.2 Results

The experimental parameters for the three UKFs are presented in Table 6.3. The measurement noise terms for the two AO-IMU estimators are given in terms $R_{\text{imu1,acc}}$ and $R_{\text{imu2,acc}}$. In the case of the noise parameters for the relative UKF the encoder noise term is given in $R_{\text{rel,enc}}$ in a similar manner to the previous systems, and the values representing the noise terms for the AO-IMU's angular velocity and angular acceleration are given in $R_{\text{rel},\omega}$ and $R_{\text{rel},\dot{\omega}}$ respectively. In these cases the values for $R_{\text{rel},\omega}$ and $R_{\text{rel},\dot{\omega}}$ are found from taking the

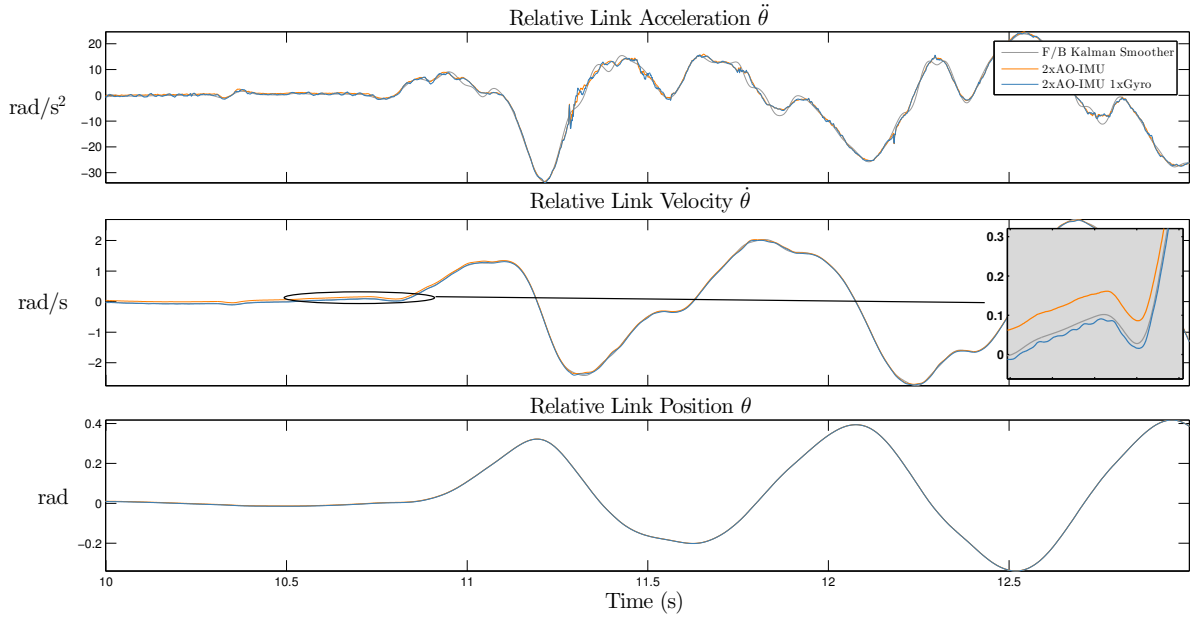

Figure 6.11: Multiple AO-IMU system showing upper joint states. Note the offset in the velocity term for the 2xAO-IMU system is not present in the 2xAO-IMU 1xGyro system.

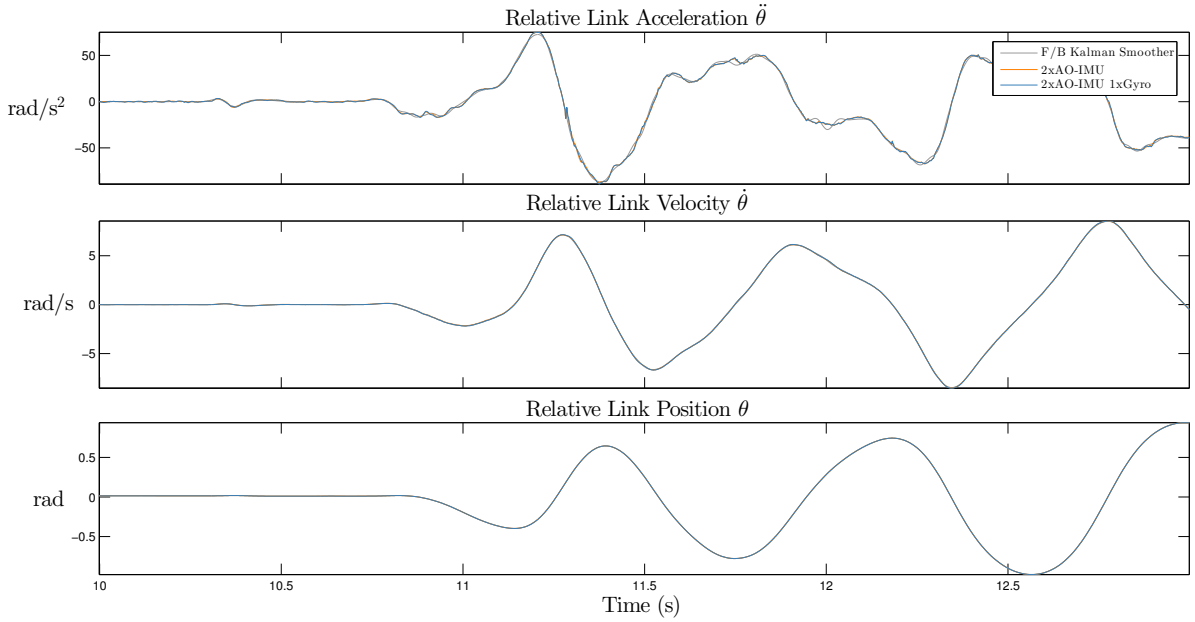

Figure 6.12: Multiple AO-IMU system showing lower (labelled as relative joint in other experiments) joint states.

variance the outputs of the AO-IMU from the plain system during a period of no movement activity. The process noise terms are given in the σ terms.

The results for this configuration as presented in Figures 6.11, 6.12 and 6.13 were interesting. It was initially expected that a performance on par with the redundant accelerometer system be seen, however it is clear from Figure 6.13 that this system suffered from poor performance, particularly in the velocity and position terms. It became apparent that the reduction in performance in these terms was due to the AO-IMU's decreasing performance when resolving low angular velocities, with further investigation into the literature (Madgwick et al. 2013) supporting this claim. In the experiments carried out the upper link AO-IMU would not experience angular velocities as large as the lower link. The result of this

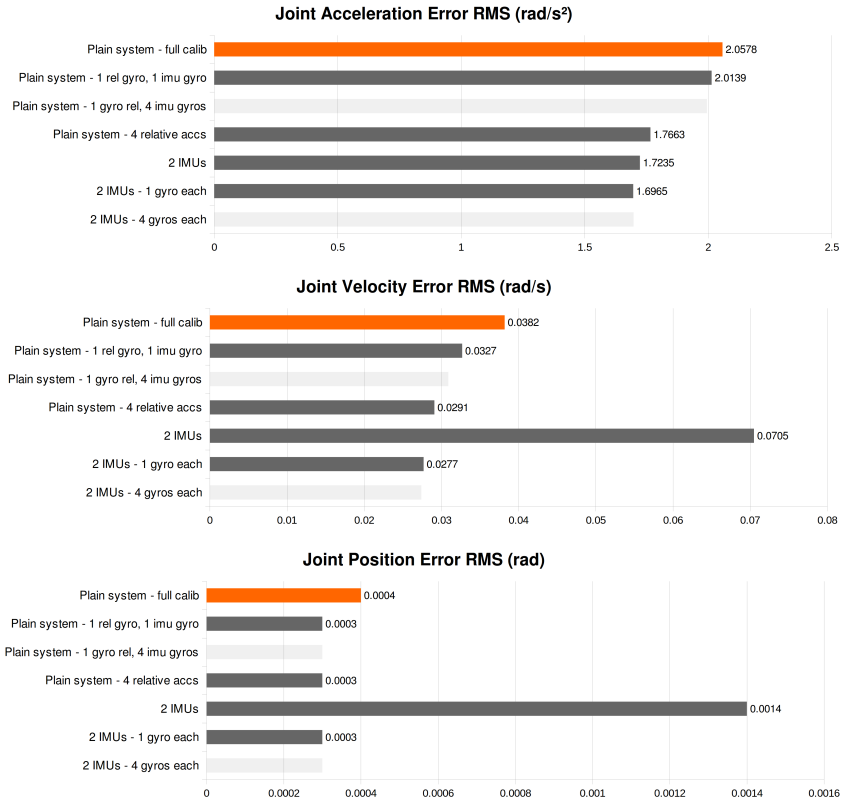

Figure 6.13: RMS error results comparing plain system to system utilising an AO-IMU on each link. Note the performance increase when augmented with a gyro.

was that the upper AO-IMU would produce a poor angular velocity estimate, which would in turn result in the relative UKF producing a velocity estimate with significant steady state bias. The bias in the upper link AO-IMU is visible in the zoomed plot on the velocity state in Figure 6.11. Evidently, the steady error introduced into the velocity component would then propagate through to the position term. Unlike the misaligned system in Section 5.5.2, tests on this system demonstrated that it was not able to be corrected with the introduction of a moving bias term. In order to combat this issue each AO-IMU system was augmented with a gyro as per the gyro configuration in 6.2.1. The addition of gyroscope sensors into this system resolved the steady state bias issue experienced at low angular velocities and increased the performance of the multi AO-IMU system to be on par with that of the redundant relative accelerometer system. The velocity plot in Figure 6.11 shows that with the addition of gyros, the AO-IMU will track low velocities more closely that the system without.

6.5 Revisiting Additional Gyros

In this section we revisit the gyro augmented system presented in Section 6.2 and the multi AO-IMU system in 6.4 with the aim of briefly exploring these systems performance with multiple gyroscope sensors. Within this the two systems are augmented to compare their respective states with measurements from four gyroscopes instead of one.

6.5.1 Additional Gyro Modelling

In these experiments the gyroscope sensor readings are calibrated, their initial bias is compensated for and the sensor readings are combined to form a virtual gyro by averaging

Table 6.4: Virtual gyroscope augmented system parameters parameters

$R_{\text{plain,vgyro}}$	2.2827×10^{-5}	$\text{rad}\,\text{s}^{-1}$
$R_{\text{imu1,vgyro}}$	2.2827×10^{-5}	$\text{rad}\,\text{s}^{-1}$
$R_{\text{imu2,vgyro}}$	2.2827×10^{-5}	$\text{rad}\,\text{s}^{-1}$

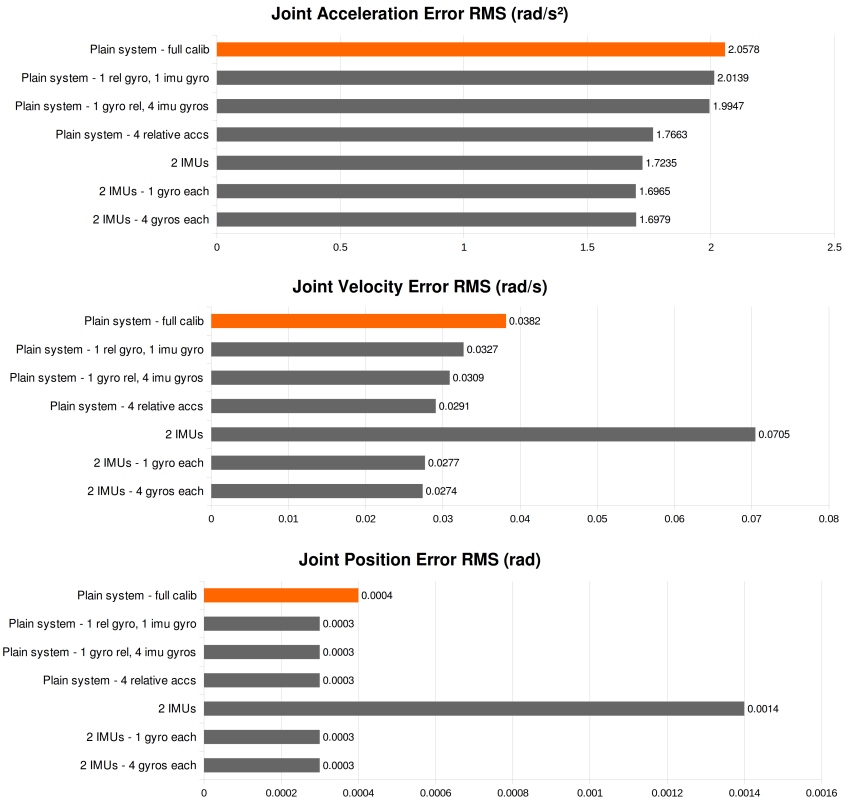

Figure 6.14: RMS error results comparing plain system all methods.

the four gyroscope sensor outputs. Chang et al. (2008) showed that a 'virtual gyroscope' whose performance will be better than that of an individual sensor can be comprised of multiple individual gyroscope sensors. Wang and Olson (2015) then go on to demonstrate that simple averaging of n sensors with independent, uncorrelated noise will see a $\sqrt{n}$ reduction in noise and in turn the optimal filtering employed in Chang et al. is not necessary. As such the gyroscope outputs are calibrated and their initial biases compensated for, and finally the outputs are averaged together and employed as a virtual gyro written as

$$^{i}\boldsymbol{g}_{v} = \frac{1}{4}\sum_{i=1}^{4} {}^{i}\boldsymbol{g}. \tag{6.18}$$

The systems presented in Section 6.2 and Section 6.4 are modified to compare their estimates to the virtual gyro. Both systems employ the same noise parameters as given in Tables 6.1 and 6.3 except the measurement noise properties for the gyros are modified to reflect the noise properties of the virtual gyro. The virtual gyro noise properties are obtained from taking the variance of the output during a period of no movement and are all identical. These values are presented in Table 6.4.

6.5.2 Results

The RMS errors of the averaged gyroscopes as compared to all other systems are given in Figure 6.14. While Wang, Wang, et al. (2015) claims there should be a $\sqrt{n}$ reduction in noise for n devices, in this case a two times reduction for four devices, the effects of this are not as evident as expected. It is evident from the RMS error that only a marginal increase in performance is gained when employing multiple gyroscopes. In comparing this to the system in Section 6.3 where multiple accelerometers were employed, the addition of multiple gyroscopes does not appear to have such a dramatic effect on the performance of the systems studied.

6.6 Summary

In this chapter alternate structures of the joint sensor system have been developed and analysed. The plain sensor system was first augmented with low cost MEMs gyroscopes in an effort to examine their performance benefits, particularly at low velocities. The results of this study showed that the addition of a single gyroscope on each link increased the basic system performance primarily within the velocity terms, and may prove to be useful in mitigating the AO-IMU's lacking velocity estimation performance.

The plain sensor system was then extended to consider multiple relative accelerometers. In this study the suspicion that the use of a single relative accelerometer led to a limit on the plain sensor system performance was confirmed. By incorporating multiple relative accelerometers it was shown that improvements to the estimation of the acceleration and velocity states performance could be made.

In building on the study into considering multiple relative accelerometers and alternate system structure was developed whereby multiple AO-IMUs were installed on each link. This system may prove more useful for larger robotic systems, however it suffered from poor velocity estimation performance. Further investigation showed that the poor performance was due to the AO-IMU's inability to estimate low angular velocities well. This was mitigated by including gyroscope sensors which in turn increased the performance to be on par with the redundant accelerometer system.

Finally the gyro augmented system and the multi AO-IMU system were revisited to investigate whether further performance gains could be found with the addition of multiple gyroscopes. This short study showed that only marginal performance gains could be achieved.

Chapter 7

Conclusion

In an effort to increase robotic control system performance and further enable the estimation of robotic system parameters, a growing trend among researchers is to begin incorporating higher order joint state terms such as acceleration into these systems. A review into the literature in Chapter 2 showed that unlike robotic joint position, access to high quality joint velocity and in particular joint acceleration information is not readily available. Within this it was found that the researchers are resorting to obtaining the information via other means, which is resulting in poorer performing systems.

The first part of the work presented in this thesis investigates a means of exploiting the use of low cost MEMs sensors and modern sensor fusion techniques to combine the information from accelerometer based IMUs and joint position sensors. From this a sensor capable of estimating a rotary robotic joint's position, velocity and acceleration was developed. Chapter 3 detailed the underlying AO-IMU and relative kinematics and derived the relationships that would allow obtaining estimates of the relative velocity and acceleration.

The state estimation and sensor fusion systems were introduced in Chapter 4. Within this the Unscented Kalman Filter that was employed to address the issues regarding estimating the velocity states within the AO-IMU was detailed. A second UKF based system was then introduced to fuse the relative velocity and acceleration obtained from the AO-IMU with positional information from an incremental encoder. This section also discussed solutions to reducing the computational complexity of the dual UKF system and detailed the methods employed to obtain the process noise matrices.

A two degree of freedom pendulum that served as a platform in which all tests were carried out on was then detailed in Chapter 5. This chapter described two calibration schemes that drastically reduced the effects of gain, bias and cross axis effect present at the MEMs sensor level and the positional and alignment errors introduced when fixing the sensors to the body frame. The offline Kalman smoother and forward/backward low pass filter and derivative systems that served as baselines for comparing the performance of the system against were then discussed. The system performance was also compared against modern online methods. An encoder based Kalman filter method, along with an encoder based derivative methods were outlined. In addition to this an online system incorporating both the position encoder and a gyroscope also served as a comparison tool.

The performance results as presented in this chapter were based on two motion profiles; an actuated chaotic profile and a zero torque drop profile that served to examine the system under low velocity conditions. The sensor system was demonstrated to perform well under both motion profiles and outperformed all the tested online methods across all states. In particular the system demonstrated far greater acceleration tracking performance than

the other online methods, with RMS error values of 2.06rad s^{-2} being achieved under full calibration over the chaotic motion profile.

The effects of the calibration methods were then examined. In this it was shown that the sensor calibration and alignment calibration schemes previously discussed indeed increased the system performance by reducing the levels of bias that appeared in the acceleration and velocity estimates. Interestingly it was demonstrated that even without the calibration schemes in place the sensor system would still outperform the existing online methods. Finally, the effects of misalignment due to inaccurate zeroing of the encoder were examined and solution to this issue was detailed.

In Chapter 6 the plain joint sensor system is expanded upon to consider additional accelerometers, the inclusion of gyroscope sensors and alternate system structures and the effects these may have on the performance of the system.

The use of gyroscopes was first considered. In this section the plain system was augmented to include an angular velocity estimate, as obtained by taking the difference between the outputs of gyroscopes placed on each link. This study aimed to examine the capability of the gyroscopes in compensating for the AO-IMU's poor performance when estimating low angular velocities. The results proved positive and it was demonstrated that by considering the output of the gyros the sensor system's angular velocity estimate could be improved upon.

The next study investigated the use of multiple relative accelerometers as opposed to the plain system's use of a single relative accelerometer. This study was introduced when the contrast between the noise performance of the AO-IMUs plain output was compared to the whole system output. The results of this experiment demonstrated that by only considering a single relative accelerometer, the plain system will suffer a limit in performance as imposed by the single device. By introducing the multiple relative accelerometers, a decrease in RMS error was seen across all states, with the acceleration term exhibiting a significant decrease from 2.06rad s^{-2} to 1.76rad s^{-2}.

The results of the multiple relative accelerometer study inspired the use of multiple AO-IMUs in the next augmented system. This study presented a system that departed from the use of the relative accelerometers, instead opting for the use of AO-IMUs attached to each link of the machine. In considering the work on larger robotic systems a system such as this was deemed possibly more suited to such larger machines. The results of this study initially proved disappointing with poor velocity state estimation being evident, resulting in an increase in the velocity term RMS error from 0.0382rad s^{-1} to 0.0705rad s^{-1}. As with the previous study that incorporated gyros, it became apparent that the poor performance was the result of the AO-IMU's declining capability when estimating low angular velocities in the upper link. The system was augmented with gyroscopes and the overall performance was improved to be on par with the multiple relative accelerometer system. In this case the velocity state RMS error was reduced to 0.0277rad s^{-1}.

Finally a short study into considering multiple gyroscopes was carried out. Within this experiment the plain system and the multiple AO-IMU system were augmented with four gyroscopes as opposed to one. The results of this showed marginal improvement over the systems employing only a single accelerometer.

References

Arteaga, Marco A (2003).
"Robot control and parameter estimation with only joint position measurements".
Automatica 39.1, pp. 67–73 (cit. on p. 2).

AS5311 High Resolution Magnetic Encoder (2009). Austria Micro Systems (cit. on p. 28).

Axelsson, Patrik, Rickard Karlsson, and Mikael Norrlof (2012).
"Tool position estimation of a flexible industrial robot using recursive Bayesian methods".
Robotics and Automation (ICRA), 2012 IEEE International Conference on. IEEE, pp. 5234–5239 (cit. on p. 8).

Baelemans, Jos (2013). "Parameter estimation of humanoid robots using the center of pressure".
PhD thesis. University of Technology (cit. on pp. 1, 2).

Baran, Eray Abdurrahman, Edin Golubovic, and Asif Sabanovic (2012).
"Functional observers for motion control systems".
Automatika–Journal for Control, Measurement, Electronics, Computing and Communications 54.2 (cit. on p. 6).

Bellini, Armando, Stefano Bifaretti, and Stefano Costantini (2003).
"A digital speed filter for motion control drives with a low resolution position encoder".
Automatika 44.12, pp. 67–74 (cit. on p. 6).

Cardou, Philippe, Guillaume Fournier, and Philippe Gagnon (2011). "A nonlinear program for angular-velocity estimation from centripetal-acceleration measurements".
Mechatronics, IEEE/ASME Transactions on 16.5, pp. 932–944 (cit. on p. 10).

Chang, Honglong et al. (2008). "An integrated MEMS gyroscope array with higher accuracy output".
Sensors 8.4, pp. 2886–2899 (cit. on p. 54).

Chen, Lisha et al. (2012).
"A novel curve fitting based discrete velocity estimator for high performance motion control".
Advanced Intelligent Mechatronics (AIM), 2012 IEEE/ASME International Conference on. IEEE, pp. 1060–1065 (cit. on p. 6).

Cheng, Peng and Bengt Oelmann (2010).
"Joint-angle measurement using accelerometers and gyroscopes A survey".
Instrumentation and Measurement, IEEE Transactions on 59.2, pp. 404–414 (cit. on pp. 7, 8).

ChibiOS/RT Home page (2016).
URL: http://www.chibios.org/dokuwiki/doku.php?id=start (visited on 10/06/2016) (cit. on p. 28).

Ciblak, Namik (2007). "Determining the Angular Motion of a Rigid Body Using Linear Accelerometers Without Integration".
Recent Advances in Space Technologies, 2007. RAST'07. 3rd International Conference on. IEEE, pp. 585–590 (cit. on p. 10).

Colton, Shane (2007). "The balance filter: a simple solution for integrating accelerometer and gyroscope measurements for a balancing platform".
white paper, Massachusetts Institute of Technology, Cambridge, MA (cit. on p. 7).

Dallali, Houman et al. (2015). "On the use of positive feedback for improved torque control".
Control Theory and Technology 13.3, pp. 266–285 (cit. on p. 1).

Frosio, Iuri, Federsini. Pedersini, and N. Aalberto Borghese (2009).
"Autocalibration of MEMS Accelerometers". 58.6, pp. 2034–2041.
DOI: 10.1109/TIM.2008.2006137 (cit. on pp. 31, 32).

Glueck, Manuel et al. (2014). "Real-time autocalibration of MEMS accelerometers". *IEEE Transactions On Instrumentation And Measurement* 63.1, pp. 96–105 (cit. on p. 31).

Godler, Ivan et al. (1995). "A novel rotary acceleration sensor". *Control Systems, IEEE* 15.1, pp. 56–60 (cit. on pp. 6, 7).

Grammatikos, Antonios (1965). "Gimballess inertial systems for space navigation" (cit. on p. 9).

Hartikainen, Jouni, Arno Solin, and Simo Sarkka (2011). "Optimal filtering with Kalman filters and smoothers". *Department of Biomedica Engineering and Computational Sciences, Aalto University School of Science: Greater Helsinki, Finland* 16 (cit. on p. 29).

Honkakorpi, Janne (2014). "MEMS-based Motion State Estimation and Control of Hydraulic Manipulators". *Tampereen teknillinen yliopisto. Julkaisu-Tampere University of Technology. Publication; 1219* (cit. on pp. 8, 9).

Hutter, Marco (2013). "StarlETH & co-design and control of legged robots with compliant actuation". PhD thesis. Diss., Eidgenossische Technische Hochschule ETH Zurich, Nr. 21073, 2013 (cit. on p. 1).

Khosla, Pradeep (1987). "Estimation of robot dynamics parameters: Theory and application" (cit. on p. 2).

Kubus, Daniel, Corrado Guarino Lo Bianco, and Friedrich M Wahl (2012). "A sensor fusion approach to improve joint angle and angular rate signals in articulated robots". *Intelligent Robots and Systems (IROS), 2012 IEEE/RSJ International Conference on*. IEEE, pp. 2736–2741 (cit. on p. 8).

Kuzma, Oto and Vaclav Kalas (2001). "A Novel Integrated Angular Acceleration, Velocity and Position Sensor". *Journal of Electrical Engineering* 52.1-2, pp. 12–18 (cit. on pp. 6, 7).

Lin, Pei-Chun and Chi-Wei Ho (2009). "Design and implementation of a 9-axis inertial measurement unit". *Proc. IEEE Int. Conf. Robotics and Automation ICRA '09*, pp. 736–741. DOI: 10.1109/ROBOT.2009.5152546 (cit. on p. 9).

Lin, Pei-Chun, Haldun Komsuoglu, and Daniel E Koditschek (2006). "Sensor data fusion for body state estimation in a hexapod robot with dynamical gaits". *Robotics, IEEE Transactions on* 22.5, pp. 932–943 (cit. on pp. 10, 15).

LIS3DSH (2011). ST Micro Electronics (cit. on p. 27).

LSM6DS3 iNEMO Inertial Module (2016). ST Micro Electronics (cit. on p. 27).

Lu, Jau-Ching and Pei-Chun Lin (2011). "State derivation of a 12-axis gyroscope-free inertial measurement unit". *Sensors* 11.3, pp. 3145–3162 (cit. on pp. 10, 15, 25).

Madgwick, Sebastian OH et al. (2013). "Measuring motion with kinematically redundant accelerometer arrays: theory, simulation and implementation". *Mechatronics* 23.5, pp. 518–529 (cit. on pp. 9, 10, 15, 25, 32, 33, 43, 46, 52).

Naerum, Edvard, Hawkeye HI King, and Blake Hannaford (2009). "Robustness of the Unscented Kalman filter for state and parameter estimation in an elastic transmission." *Robotics: Science and Systems* (cit. on p. 2).

Nilsson, John-Olof, Isaac Skog, and Peter Handel (2014). "Aligning the forces-Eliminating the misalignments in IMU arrays". *IEEE Transactions on Instrumentation and Measurement* 63.10, pp. 2498–2500 (cit. on p. 34).

Padgaonkar, A. J., K. W. Krieger, and A. I. King (1975). "Measurement of angular acceleration of a rigid body using linear accelerometers". *Journal of Applied Mechanics* 42.3, pp. 552–556 (cit. on p. 9).

Panahandeh, G., I. Skog, and M. Jansson (2010). "Calibration of the accelerometer triad of an inertial measurement unit, maximum likelihood estimation and Cramer-Rao bound". *Indoor Positioning and Indoor Navigation (IPIN), 2010 International Conference on*, pp. 1–6. DOI: 10.1109/IPIN.2010.5646832 (cit. on p. 31).

Petrella, Roberto et al. (2007). "Speed measurement algorithms for low-resolution incremental encoder equipped drives: a comparative analysis".

Electrical Machines and Power Electronics, 2007. ACEMP'07. International Aegean Conference on. IEEE, pp. 780–787 (cit. on pp. 5, 6).

Quigley, Morgan et al. (2010). "Low-cost accelerometers for robotic manipulator perception". *Intelligent Robots and Systems (IROS), 2010 IEEE/RSJ International Conference on*. IEEE, pp. 6168–6174 (cit. on p. 7).

Radulescu, Andreea et al. (2012). "Exploiting variable physical damping in rapid movement tasks". *Advanced Intelligent Mechatronics (AIM), 2012 IEEE/ASME International Conference on*. IEEE, pp. 141–148 (cit. on p. 1).

Restivo, M. T., F. G. Almeida, and D. Freitas (2012). "Measuring relative acceleration: A relative angular acceleration prototype transducer". *Measurement Science and Technology* 24.2, p. 025101 (cit. on p. 7).

Rotella, Nicholas et al. (2016). "Inertial Sensor-Based Humanoid Joint State Estimation". *arXiv preprint arXiv:1602.05134* (cit. on pp. 1, 3, 8, 9, 49).

Schopp, Patrick et al. (2010). "Design, geometry evaluation, and calibration of a gyroscope-free inertial measurement unit". *Sensors and Actuators A: Physical* 162.2, pp. 379–387 (cit. on pp. 9, 10, 14, 15).

Shaowei, Wang and Wan Shanming (2012). "Velocity and acceleration computations by single-dimensional Kalman filter with adaptive noise variance". *Przeglad Elektrotechniczny* 88.2, pp. 283–287 (cit. on p. 6).

Su, Y. X. et al. (2005). "A simple nonlinear velocity estimator for high-performance motion control". *Industrial Electronics, IEEE Transactions on* 52.4, pp. 1161–1169 (cit. on p. 6).

Van Der Merwe, Rudolph and Eric A Wan (2004). "Sigma-point Kalman filters for integrated navigation". *Proceedings of the 60th Annual Meeting of the Institute of Navigation (ION)*, pp. 641–654 (cit. on pp. 18, 19).

Van Der Merwe, Rudolph, Eric A Wan, Simon Julier, et al. (2004). "Sigma-point Kalman filters for nonlinear estimation and sensor-fusion: Applications to integrated navigation". *Proceedings of the AIAA Guidance, Navigation & Control Conference*, pp. 16–19 (cit. on p. 2).

Wan, Eric, Ronell Van Der Merwe, et al. (2000). "The unscented Kalman filter for nonlinear estimation". *Adaptive Systems for Signal Processing, Communications, and Control Symposium 2000. AS-SPCC. The IEEE 2000*. IEEE, pp. 153–158 (cit. on p. 19).

Wang, John and Edwin Olson (2015). "High-performance inertial measurements using a redundant array of inexpensive gyroscopes (RAIG)". *Proc. IEEE Int. Conf. Multisensor Fusion and Integration for Intelligent Systems (MFI)*, pp. 71–76. DOI: 10.1109/MFI.2015.7295748 (cit. on p. 54).

Wang, Shiqian, Letian Wang, et al. (2015). "Design and Control of the MINDWALKER Exoskeleton". *Neural Systems and Rehabilitation Engineering, IEEE Transactions on* 23.2, pp. 277–286 (cit. on p. 55).

Webb, Dustin J, Kyle L Crandall, and Jur van den Berg (2014). "Online parameter estimation via real-time replanning of continuous Gaussian POMDPs". *2014 IEEE International Conference on Robotics and Automation (ICRA)*. IEEE, pp. 5998–6005 (cit. on p. 2).

Xinjilefu (2015). "State estimation for humanoid robots". PhD thesis. DTIC Document (cit. on pp. 1, 2, 9, 49).

Zappa, Bruno et al. (2001). "On the number and placement of accelerometers for angular velocity and acceleration determination". *Transactions-American Society of Mechanical Engineers Journal of Dynamic Systems Measurement and Control* 123.3, pp. 552–553 (cit. on p. 9).

Zhao, Hao and Hao Feng (2015). "A Novel Permanent Magnetic Angular Acceleration Sensor". *Sensors* 15.7, pp. 16136–16152 (cit. on p. 7).

Zhu, Wen-Hong and Tom Lamarche (2007). "Velocity estimation by using position and acceleration sensors". *Industrial Electronics, IEEE Transactions on* 54.5, pp. 2706–2715 (cit. on pp. 5, 8).

Appendix A

Link Ideal Rotations

These matrices serve to rotate the sensor outputs from as they are mounted to the test rig into the ideal sensor frame.
Link l_i ideal rotation matrices:

$$ {}^{l_i,1'}_{l_i,1}\tilde{\boldsymbol{R}} = \begin{bmatrix} 0 & -1 & 0 \\ 1 & 0 & 0 \\ 0 & 0 & 1 \end{bmatrix}, \tag{A.1} $$

$$ {}^{l_i,2'}_{l_i,2}\tilde{\boldsymbol{R}} = \begin{bmatrix} 0 & 1 & 0 \\ 1 & 0 & 0 \\ 0 & 0 & -1 \end{bmatrix}, \tag{A.2} $$

$$ {}^{l_i,3'}_{l_i,3}\tilde{\boldsymbol{R}} = \begin{bmatrix} 0 & -1 & 0 \\ 1 & 0 & 0 \\ 0 & 0 & 1 \end{bmatrix}, \tag{A.3} $$

$$ {}^{l_i,4'}_{l_i,4}\tilde{\boldsymbol{R}} = \begin{bmatrix} 0 & 1 & 0 \\ 1 & 0 & 0 \\ 0 & 0 & -1 \end{bmatrix}, \tag{A.4} $$

Link l_{i-1} ideal rotation matrices:

$$ {}^{l_{i-1},1'}_{l_{i-1},1}\tilde{\boldsymbol{R}} = \begin{bmatrix} 0 & -1 & 0 \\ 1 & 0 & 0 \\ 0 & 0 & 1 \end{bmatrix}, \tag{A.5} $$

$$ {}^{l_{i-1},2'}_{l_{i-1},2}\tilde{\boldsymbol{R}} = \begin{bmatrix} 0 & 1 & 0 \\ 1 & 0 & 0 \\ 0 & 0 & -1 \end{bmatrix}, \tag{A.6} $$

$$ {}^{l_{i-1},3'}_{l_{i-1},3}\tilde{\boldsymbol{R}} = \begin{bmatrix} 0 & -1 & 0 \\ 1 & 0 & 0 \\ 0 & 0 & 1 \end{bmatrix}, \tag{A.7} $$

$$ {}^{l_{i-1},4'}_{l_{i-1},4}\tilde{\boldsymbol{R}} = \begin{bmatrix} 0 & 1 & 0 \\ 1 & 0 & 0 \\ 0 & 0 & -1 \end{bmatrix}. \tag{A.8} $$

Appendix B

Additive (Zero Mean) Unscented Kalman Filter

The UKF is initialised with

$$\begin{aligned} \hat{\boldsymbol{x}}_0 &= \mathbb{E}\left[\boldsymbol{x}_0\right], \\ \boldsymbol{P}_0 &= \mathbb{E}\left[(\boldsymbol{x}_0 - \hat{\boldsymbol{x}}_0)(\boldsymbol{x}_0 - \hat{\boldsymbol{x}}_0)^{\mathsf{T}}\right]. \end{aligned} \tag{B.1}$$

For $k \in \{1, \ldots, \infty\}$ the sigma points are calculated as

$$\boldsymbol{\mathcal{X}}_{k-1} = \begin{bmatrix} \hat{\boldsymbol{x}}_{k-1} & \hat{\boldsymbol{x}}_{k-1} + \gamma\sqrt{\boldsymbol{P}_{k-1}} & \hat{\boldsymbol{x}}_{k-1} - \gamma\sqrt{\boldsymbol{P}_{k-1}} \end{bmatrix}. \tag{B.2}$$

The time update equations are

$$\begin{aligned} \boldsymbol{\mathcal{X}}^*_{k|k-1} &= \boldsymbol{f}(\boldsymbol{\mathcal{X}}_{k-1}, \boldsymbol{u}_{k-1}), \\ \hat{\boldsymbol{x}}_k^- &= \sum_{i=0}^{2L} W_i^{(c)} \boldsymbol{\mathcal{X}}^*_{i,k|k-1}, \\ \boldsymbol{P}_k^- &= \sum_{i=0}^{2L} W_i^{(m)} (\boldsymbol{\mathcal{X}}^*_{i,k|k-1} - \hat{\boldsymbol{x}}_{k-1})(\boldsymbol{\mathcal{X}}^*_{i,k|k-1} - \hat{\boldsymbol{x}}_{k-1})^{\mathsf{T}} + \boldsymbol{R}^v, \\ \boldsymbol{\mathcal{X}}_{k|k-1} &= \begin{bmatrix} \boldsymbol{\mathcal{X}}^*_{i,k|k-1} & \boldsymbol{\mathcal{X}}^*_{0,k|k-1} + \gamma\sqrt{\boldsymbol{R}^v} & \boldsymbol{\mathcal{X}}^*_{0,k|k-1} + \gamma\sqrt{\boldsymbol{R}^v} \end{bmatrix}, \\ \boldsymbol{\mathcal{Y}}_{k|k-1} &= \boldsymbol{h}(\boldsymbol{\mathcal{X}}_{k|k-1}), \\ \hat{\boldsymbol{y}}_k^- &= \sum_{i=0}^{2L} W_i^{(c)} \boldsymbol{\mathcal{Y}}_{i,k|k-1}. \end{aligned} \tag{B.3}$$

The measurement update equations are

$$\begin{aligned} \boldsymbol{P}_{\tilde{\boldsymbol{y}}_k \tilde{\boldsymbol{y}}_k} &= \sum_{i=0}^{2L} W_i^{(c)} (\boldsymbol{\mathcal{Y}}_{i,k|k-1} - \hat{\boldsymbol{y}}_k^-)(\boldsymbol{\mathcal{Y}}_{i,k|k-1} - \hat{\boldsymbol{y}}_k^-)^{\mathsf{T}} + \boldsymbol{R}^n, \\ \boldsymbol{P}_{\boldsymbol{x}_k \boldsymbol{y}_k} &= \sum_{i=0}^{2L} W_i^{(c)} (\boldsymbol{\mathcal{X}}_{i,k|k-1} - \hat{\boldsymbol{x}}_k^-)(\boldsymbol{\mathcal{Y}}_{i,k|k-1} - \hat{\boldsymbol{y}}_k^-)^{\mathsf{T}}, \\ \boldsymbol{\mathcal{K}}_k &= \boldsymbol{P}_{\boldsymbol{x}_k \boldsymbol{y}_k} \boldsymbol{P}_{\tilde{\boldsymbol{y}}_k \tilde{\boldsymbol{y}}_k}{}^{-1}, \\ \hat{\boldsymbol{x}}_k &= \hat{\boldsymbol{x}}_k^- + \boldsymbol{\mathcal{K}}_k (\boldsymbol{y}_k - \hat{\boldsymbol{y}}_k^-), \\ \boldsymbol{P}_k &= \boldsymbol{P}_k^- - \boldsymbol{\mathcal{K}}_k \boldsymbol{P}_{\tilde{\boldsymbol{y}}_k \tilde{\boldsymbol{y}}_k} \boldsymbol{\mathcal{K}}_k^{\mathsf{T}}. \end{aligned} \tag{B.4}$$

Where $\gamma = \sqrt{L + \lambda}$ and λ is a scaling parameter such that $\lambda = \alpha^2(L + \kappa) - L$. The constant α controls the spread of the sigma points around $\hat{\boldsymbol{x}}$ and κ is a secondary scaling parameter.

L is the dimension of the state vector, $\boldsymbol{R}^v$ is the process noise covariance and $\boldsymbol{R}^n$ is the measurement noise covariance. The weights W_i are given by

$$W_0^{(m)} = \frac{\lambda}{L+\lambda}, \tag{B.5}$$

$$W_0^{(c)} = \frac{\lambda}{L+\lambda} + 1 - \alpha^2 + \beta, \tag{B.6}$$

and

$$W_i^{(m)} = W_{(i)}^c = \frac{\lambda}{2(L+\lambda)}, \qquad i = 1, \ldots, 2L. \tag{B.7}$$

Where β is a parameter that incorporates prior knowledge of the distribution of $\boldsymbol{x}$.